

AD-A276 166

ATION PAGE

Form Approved
OMB No. 0704-0188

to average 1 hour per response, including the time for reviewing instructions, searching existing data sources, gathering the collection of information. Send comments regarding this burden estimate or any other aspect of this form to Washington Headquarters Services, Directorate for Information Operations and Reports, 1215 Jefferson Avenue, Washington, DC 20540.

1. AGENCY USE ONLY (Leave blank)		2. REPORT DATE 18 Oct 93		3. REPORT TYPE AND DATES COVERED Final 11 Dec 89 - 30 Jun 93	
4. TITLE AND SUBTITLE Solidification Structure Synthesis in Undercooled Liquids				5. FUNDING NUMBERS DAAL03-90-6-0042	
6. AUTHOR(S) J.H. Perepezko					
7. PERFORMING ORGANIZATION NAME(S) AND ADDRESS(ES) University of Wisconsin-Madison Dept. of Materials Science and Engineering 1509 University Avenue Madison, WI 53706				8. PERFORMING ORGANIZATION REPORT NUMBER	
9. SPONSORING / MONITORING AGENCY NAME(S) AND ADDRESS(ES) U.S. Army Research Office P.O. Box 12211 Research Triangle Park, NC 27709-2211				10. SPONSORING / MONITORING AGENCY REPORT NUMBER ARO 27472.6-m5	
11. SUPPLEMENTARY NOTES The views, opinions and/or findings contained in this report are those of the author(s) and should not be construed as an official Department of the Army position, policy, or decision, unless so designated by other documentation.					
12a. DISTRIBUTION / AVAILABILITY STATEMENT Approved for public release; distribution unlimited.				12b. DISTRIBUTION CODE	
13. ABSTRACT (Maximum 200 words) The undercooling of liquid metals is a fairly common observation, but the amount of undercooling is limited usually by the action of heterogeneous catalysts. When a liquid is subdivided into a fine droplet dispersion in order to isolate nucleation catalysis, substantial undercooling may be observed before the onset of solidification, as demonstrated by the increased undercooling limits established in the current work. At high undercooling, the solidification of alloys can result in the suppression of the usual crystallization reactions and in the formation of nonequilibrium phases with distinct and novel microstructures. A number of processing variables have been established to control undercooling including: droplet size, melt superheat, cooling rate and droplet surface chemistry. The application of thermal analysis together with x-ray diffraction and microstructural examination methods has allowed for an evaluation of the kinetic competition during phase selection, for the determination of the decomposition and melting temperatures of metastable phases and for the assessment of metastable phase diagrams. New advances have also been made in the understanding and control of heterogeneous nucleation and in probing the thermal history of rapidly solidifying samples by upquenching studies as well as in the development of new experimental capacity to study composites. The understanding developed from droplet undercooling studies has a direct application to Rapid Solidification Processing (RSP) and allows for an assessment of RSP treatment in terms of the influence of undercooling and metastable phase equilibria on phase selection and novel solidification microstructure development. The basic information that droplet studies yield also has a broad application to many aspects of solidification processing. The undercooling behavior of droplet samples has been determined by differential thermal analysis. An assessment of the stability and thermal history of the solidification products has been provided by calorimetric measurements, controlled upquenching and high temperature x-ray diffraction. Phase identification and microstructural characteristics in droplet samples are essential for the proper interpretation of undercooling and solidification behavior and have been studied by optical and electron metallography including TEM and Auger surface analysis on selected samples, quantitative image analysis and x-ray diffraction methods.					
14. SUBJECT TERMS				15. NUMBER OF PAGES 88	
				16. PRICE CODE	
17. SECURITY CLASSIFICATION OF REPORT UNCLASSIFIED		18. SECURITY CLASSIFICATION OF THIS PAGE UNCLASSIFIED		19. SECURITY CLASSIFICATION OF ABSTRACT UNCLASSIFIED	
				20. LIMITATION OF ABSTRACT UL	

94-06154

94 2 24 117

**Best
Available
Copy**

Solidification Structure Synthesis in Undercooled Liquids

Final Report

J.H. Perepezko

18 Oct 93

U.S. Army Research Office

Grant Number
DAAL-3-90-G-0042

University of Wisconsin-Madison

APPROVED FOR PUBLIC RELEASE;
DISTRIBUTION UNLIMITED

Table of Contents

LIST OF FIGURES	i
LIST OF TABLES	iv
ABSTRACT	1
INTRODUCTION	2
I. BACKGROUND	5
A. Droplet-emulsion Undercooling Technique	5
B. Thermal History Behavior	7
C. Dispersed Particle Catalysis	9
D. Design of High Temperature Al Alloys	11
II. RESEARCH ACCOMPLISHMENTS OF THE CURRENT PROGRAM	13
A. Undercooling Behavior of Pure Metals	15
B. Solidification of Al Alloy Powders	17
C. Heterogeneous Nucleation	21
1. Dispersed Particle Catalysis of Liquid Droplets	22
2. Heterogeneous Nucleation in Al-Ti-X systems	27
D. Metastable Phase Diagrams	32
1. Supersaturation in Sn-Sb Alloys	32
2. Microstructural Transitions in Fe-Ni alloys	33
E. Droplet Nucleation Kinetics	36
F. Controlled Alloy Phase Nucleation Catalysis	38
III. PUBLICATIONS OF THE CURRENT PROGRAM	40
IV. PARTICIPATING SCIENTIFIC PERSONNEL	41
V. REFERENCES	42
VI. FIGURES	47

DTC QUALITY INSPECTED 3

List of Figures

- Figure 1 Schematic representation of the recalescence for an isomorphous alloy of composition C_0 .
- Figure 2 Comparison of the measured values of T_0 with the Si-rich portion of the Sn-Bi phase diagram and the calculated T_0 curve (dashed line).
- Figure 3 The reported equilibrium binary phase diagram for the Al-Y system.
- Figure 4 A partial Al-Y binary phase diagram indicating the range of compositions studied and the phases formed by rapid solidification processing.
- Figure 5 X-ray diffraction traces of the Al-3at%Y sample in the as-solidified condition (trace A) and in the post thermal cycling condition (trace B) showing the presence of $L1_2$ reflections.
- Figure 6 X-ray diffraction traces of the Al-18.1at%Y sample in the as-solidified condition (trace A) and the post DSC condition (trace B).
- Figure 7 The observed lattice parameters of the supersaturated Al_2Y phase versus the composition determined by EDS analysis.
- Figure 8 The crystallography of the $\{110\}$ plane along with the geometric relationships of the atoms.
- Figure 9 The observed lattice parameters of supersaturated Al_2Y phase versus composition along with the calculated relationships using Goldschmidt radii and ideal radii.
- Figure 10 Schematic illustrating (a) nucleant isolation and particle incorporation during droplet emulsification and (b) potential nucleation sites in a particle incorporated droplet.
- Figure 11 Nucleant site identification in pure Sn and Y_2O_3 particle dispersed Sn droplets.
- Figure 12 Schematic illustrating the nucleation catalysis model for inoculant particles that are stable in liquid Sn.
- Figure 13 Schematic illustrating the production of Al master alloy droplet emulsions containing incorporated inoculant particles.
- Figure 14 DTA thermograms depicting the melting and nucleation behavior of (A) a bulk commercial Al-6 wt.% Ti master alloy sample, (B) a droplet sample of the commercial Al-6 wt.% Ti master alloy and (C) high purity Al-1 wt.% Ti.

Figure 15 Schematic depicting the stable Al-Al₃Ti and metastable Al-Al_xTi phase diagrams and accompanying thermogram showing the melting and nucleation behavior of Al in high purity Al-1 wt.% Ti droplets.

Figure 16 SEM photomicrograph (A) and corresponding X-ray map (B) of a master alloy droplet containing irregular faceted Si bearing inoculant particles that promoted Al nucleation prior to quenching from 671°C.

Figure 17 SEM photomicrograph (A) and corresponding X-ray map (B) of a master alloy droplet containing a blocky faceted Si free inoculant particle that has not promoted Al nucleation prior to quenching from 671°C.

Figure 18 Enlarged view of the Al-Ti-Si phase diagram with superimposed EPMA compositional data from inoculant particles found in the master alloy droplets.

Figure 19 DTA thermograms obtained for Al-6wt.% Ti commercial alloys containing different amounts of Boron. The corresponding reaction temperatures are indicated as well as sets of quenching temperatures T1, T2, and T3: a) 0.2 %wt.B b) 1 %wt.B

Figure 20 Mixed backscattered and secondary electron image of Al-6 wt.% Ti-0.2 wt.% B alloy droplets quenched at T1 (Figure 19 b), revealing an active (A) and inactive (I) intermetallics. The sample was etched using 4% NaOH solution followed by 4% HF solution.

Figure 21 Mixed backscattered and secondary electron image of Al-6 wt.% Ti-1 wt.% B alloy droplets quenched at T1 (Figure 19 b), revealing an active (A) and inactive (I) intermetallics. The sample was etched using 4% NaOH solution followed by 4% HF solution.

Figure 22 Mixed backscattered and secondary electron image photomicrograph of an unetched pure Al droplet containing a SiC particle emulsified at 800°C.

Figure 23 Differential Thermal Analysis traces generated by γ Al₂O₃-Al composite droplet samples containing 1 μ m γ Al₂O₃ particles at a heating rate of 5°C/min and cooling rates of: a) -30°C/min. b) -3°C/min.

Figure 24 Differential Thermal Analysis traces generated by a SiC-Al composite droplet sample containing 10-40 μ m SiC particles at heating and cooling rates of 5°C/min during: a) First cycle after emulsification. b) Second cycle after emulsification.

Figure 25 The Sn-Sb phase diagram of Predel and Schwermann. B. Predel and W. Schwermann, *J. Inst. Met.*, 99, 169 (1971).

Figure 26 DTA thermogram of the emulsified Sn-16 wt.% Sb alloy. The sample was prepared under argon and treated with organometallic acids.

Figure 27 Compilation of measurements of the β lattice constant a_0 as a function of Sb content. Circles: Lee and Raynor (Ref: J. A. Lee and G. V. Raynor, *Proc. Phys. Soc.*, B67, 737

(1954); squares: Varich and Yakunin (Ref: N. I. Varich and A. A. Yakunin, *Izv. Akad. Nauk USSR, Met.*, 2, 229 (1968); filled circle: Kaczorowski and Matyja (Ref: M. Kaczorowski and H. Matyja, *J. Mater. Sci.*, 14, 2887 (1979); and filled square: present investigation.

Figure 28 SEM micrographs of emulsified Sn-16 at.% Sb: argon cover with acid treatment. $\Delta T \cong 100^\circ\text{C}$, $T = 200^\circ\text{C s}^{-1}$. Micrograph A: as-solidified condition: powders consist of supersaturated β . Micrograph B: aged at room temperature: β contains a dispersion of SnSb precipitates.

Figure 29 Tin-rich portion of the Sn-Sb phase diagram showing metastable extensions of the β liquidus and solidus as well as $T_0^{\beta/L}$ (dot-dashed line). A metastable melting point maximum is indicated in the vicinity of 15 at.% Sb. Open circles: Predel and Schwermann B. Predel and W. Schwermann, *J. Inst. Met.*, 99, 169 (1971); open squares: Iwasé *et al* (Ref: K. Iwasé, N. Aoki and A. Osawa, *Sci. Rep. Tôhoku Univ.*, 20, 353 (1931); and filled circles: present investigation.

Figure 30 Schematic of the drop tube apparatus: (a) powder processing and (b) drop processing.

Figure 31 High-temperature Fe-Ni phase diagram with the undercooling levels of the large drops processed in He-2% H₂ labeled.

Figure 32 Comparative metastable bcc yields vs. average droplet diameter for Fe-15 wt.% Ni powder processed in He and He-2 % H₂ atmospheres.

Figure 33 Schematic of two possible solidification pathways and different solid-state reactions for drop tube-processed samples.

Figure 34 Schematic illustration of the microstructural evolution in large drops processed in the drop tube (S.C.B. = solidification cell boundary; G.B. = grain boundary; α' = martensite).

Figure 35 Schematic of solid-state powder processing pathways in Fe-15 wt.% Ni superimposed on a continuous cooling transition curve for bcc \rightarrow fcc: T_1 = cooling of solid powder ($d = 30$ to $44\ \mu\text{m}$) processed from the melt; T_2 = cooling of solid powder ($d = 75$ to $100\ \mu\text{m}$) processed from the melt; T_3 = heating of solid powder ($d = 30$ to $44\ \mu\text{m}$) during reprocessing in the solid state; and T_4 = cooling of solid powder ($d = 30$ to $44\ \mu\text{m}$) during reprocessing in the solid state.

Figure 36 Summary of the structural evolution in the drop tube processing of Fe-Ni alloy processed in a He-2% H₂ environment.

Figure 37 Heat capacity data measured for liquid and crystalline Au_{53.2}Pb_{27.5}Sb_{19.3} alloys.

Figure 38 Free-energy difference between undercooled liquid and eutectic solid per unit volume based on different approximations including the experimental data.

Figure 39 Calculated steady-state heterogeneous nucleation kinetics of glass-forming Au-Pb-Sb alloys including a correction for the temperature dependence of the viscosity of the prefactor terms for the different models for ΔG_V and the resulting ideal glass transition temperatures with the experimentally derived ideal glass transition temperature indicated as T_{g0} . The curves correspond to the extrapolation of experimental data (exp.), (b) to the approximation of ΔG_V and $T_{\Delta S=0}$ by Dubey and Ramachandrarao, *Acta Met.*, 32, 91, (1984), (c) by Thompson and Spaepen, *Acta Met.*, 27, 1855, (1979), and (d) by Hoffman, *J. Chem. Phys.*, 29, 1192, (1958), respectively.

Figure 40 Illustration of the approach used to measure the catalytic potency of a primary substrate for nucleation of secondary phase.

Figure 41 Geometry of heterogeneous nuclei with various substrate growth modes.

Figure 42 Exotherms observed during cooling phase of "het" cycles. The numbers along the right-hand side correspond to the cycle number. Note that the exotherm at 210°C disappears with increasing cycling, while the exotherm at 182°C increases.

List of Tables

Table 1. The effect of the various processing parameters on the undercooling response.

Table 2. The maximum undercooling limits for several pure metals measured using thermal analysis.

Table 3. The observed lattice parameters of the C15 Laves phase for each sample where the composition was determined by EDS analysis.

Table 4. A summary of nucleation catalysis results obtained from droplet emulsion studies.

Table 5. The influence of inoculant thermodynamic stability in the liquid as a function of undercooling behavior for oxide catalysis of Sn.

Accession For	
NTIS	<input checked="" type="checkbox"/>
CRA&I	<input type="checkbox"/>
DTIC	<input type="checkbox"/>
TAB	<input type="checkbox"/>
Unannounced	<input type="checkbox"/>
Justification _____	
By _____	
Distribution / _____	
Availability Codes	
Dist	Avail and/or Special
A-1	

ABSTRACT

The undercooling of liquid metals is a fairly common observation, but the amount of undercooling is limited usually by the action of heterogeneous catalysts. When a liquid is subdivided into a fine droplet dispersion in order to isolate nucleation catalysis, substantial undercooling may be observed before the onset of solidification, as demonstrated by the increased undercooling limits established in the current work. At high undercooling, the solidification of alloys can result in the suppression of the usual crystallization reactions and in the formation of nonequilibrium phases with distinct and novel microstructures. A number of processing variables have been established to control undercooling including: droplet size, melt superheat, cooling rate and droplet surface chemistry. The application of thermal analysis together with x-ray diffraction and microstructural examination methods has allowed for an evaluation of the kinetic competition during phase selection, for the determination of the decomposition and melting temperatures of metastable phases and for the assessment of metastable phase diagrams. New advances have also been made in the understanding and control of heterogeneous nucleation and in probing the thermal history of rapidly solidifying samples by upquenching studies as well as in the development of new experimental capacity to study composites. The understanding developed from droplet undercooling studies has a direct application to Rapid Solidification Processing (RSP) and allows for an assessment of RSP treatment in terms of the influence of undercooling and metastable phase equilibria on phase selection and novel solidification microstructure development. The basic information that droplet studies yield also has a broad application to many aspects of solidification processing.

The undercooling behavior of droplet samples has been determined by differential thermal analysis. An assessment of the stability and thermal history of the solidification products has been provided by calorimetric measurements, controlled upquenching and high temperature x-ray diffraction. Phase identification and microstructural characteristics in droplet samples are essential for the proper interpretation of undercooling and solidification behavior and have been studied by optical and electron metallography including TEM and Auger surface analysis on selected samples, quantitative image analysis and x-ray diffraction methods.

The results of this study have allowed for a quantitative assessment of the undercooling of liquid alloys, the stability of solidification structures, an improved comprehension of the reaction path followed during alloy solidification including the influence of competing metastable phase reactions and contribute to an improved understanding and modeling of microstructure evolution during RSP and other processing such as spray deposition, surface

melting and composite fabrication. It is clear that the full potential for the use of nucleation control in solidification processing has not yet been realized.

INTRODUCTION

The undercooling of liquid metals below their equilibrium melting point is a common occurrence in solidification. Throughout the analysis of solidification processing, the conditions of nucleation and liquid undercooling behavior have been recognized for the strong influence that they can exert on the initial stage of solidification structure formation. Moreover, undercooling phenomenon are recognized as being of central importance in the nucleation of equilibrium and non-equilibrium crystalline phases and in the formation of amorphous phases. At the same time, in theoretical and applied crystal growth work the amount of liquid undercooling is regarded as one of the critical parameters in determining the path of morphological evolution and the final solidification structure.

Although undercooling effects can be observed during the slow cooling of a liquid metal, most often, before an appreciable undercooling can develop, crystallization initiates at some heterogeneous catalytic site [1]. In practice, nucleation catalysts may be activated by any of a number of different types of sites in contact with the liquid including impurity aggregates, foreign inclusions and container walls. However, a number of experimental approaches have been developed which are effective in extending the range of observable undercooling and in permitting the examination of the rapid crystallization that develops following nucleation at high undercooling.

One of the highlights in the development of novel microstructures by advanced solidification processing methods is the common occurrence of various metastable structural states. Whether these structures represent ultrafine grain sizes, supersaturated compositions of equilibrium phases or non-equilibrium phase structures, their development has expanded significantly the range of microstructural options that are available for the synthesis of new materials and the attainment of new levels of performance.

Although a given novel microstructure may be synthesized through a variety of seemingly different processing routes, there is a common underlying thermodynamic criterion that is always applicable. Through the various stages of a processing operation the initial state of the reacting material must be energized to an elevated free energy configuration which represents a partially relaxed state. In the case of solidification processing operations, the energized state is achieved by cooling the liquid into the undercooled domain. While this viewpoint is widely

acknowledged and frequently used to account for metastable structure synthesis, the application is usually developed in a qualitative manner. For the most part this is due to the difficulty in accessing the undercooled state in a manner which allows for the measurement of the relevant thermodynamic properties. In fact, most of the thermodynamic measurements pertaining to metastable solidification reactions have been obtained from droplet samples which can exhibit a deep undercooling during slow cooling [2-5]. The commonly used rapid quench methods do not permit reliable thermodynamic measurements in general.

The establishment of melt undercooling as a key variable in microstructural development provides an important link between rapid quenching studies and undercooling research. Indeed, in many respects undercooling is a more fundamental parameter than cooling rate. In most work on RSP, cooling rate is used as a convenient process variable. However, in solidification studies on undercooled samples, it has been demonstrated that undercooling can be treated in a meaningful way as a process variable [2, 4, 6, 7]. Accordingly, examination of solidification in undercooled liquids can contribute to the basic understanding necessary for a successful microstructure control and alloy design in the optimization of processing treatments.

Solidification processing has been and continues to remain one of the dominant processing approaches for materials. One of the main reasons is the flexibility that solidification processing offers, for adaptation to new approaches to materials design and structure synthesis and the fabrication of components. These attributes allow for the production of premium quality material in a cost effective manner.

As a result of numerous studies on the rapid solidification of liquids it has become clear that the processing conditions play a major role in determining the selection of specific solidification phases and microstructural morphologies. Indeed, the rich variety of solidification microstructures that is accessible by RSP represents an important strength of the approach. At the same time, the flexibility in microstructure selection represents a key challenge to implementing a coherent guide to the control of processing that will permit an optimization of alloy design and processing in order to achieve a given structure. During the current work progress has been achieved in developing the desired alloy design and processing guide based upon advances in the fundamental understanding of some of the intrinsic sample characteristics and extrinsic factors involved in melt processing that control structure selection and development. Much of the current effort has focused upon melt undercooling as the key process variable, but new insight has also been developed on the role of external cooling rate and the interaction between cooling rate and undercooling in microstructure formation.

An effective experimental approach that may be applied successfully to yield large undercoolings before the initiation of solidification involves the slow cooling from the melt of a dispersion of stabilized fine droplets [2,9]. An important advantage of the droplet method is the capability to determine both the undercooling to the start of solidification and the nucleation kinetics. In addition, the high liquid undercooling that is possible in droplet samples has been found to result in conditions favorable for the formation of metastable solid structures during a slow cooling which are similar to those produced during rapid quenching treatments. Beyond these kinetic features, the use of droplet samples allows for the structural characterization of the solidification product phases and the microstructural morphology and for the measurement of the properties of the metastable undercooled liquid state [10]. With the advent of improved sample preparation and more extensive structural determinations, the droplet method has provided also a basis for the judgment of the phase selection nucleation kinetics that govern structure development during rapid solidification processing [4,11]. Moreover, this information represents a background that is needed in order to develop a new alloy design strategy to optimize the desirable microstructural features of RSP treatment.

As part of the investigation of melt processing, progress has been made in the analysis and interpretation of metastable phase formation. The application of metastable phase diagrams and T_0 constructions are now recognized as valuable aids in such an analysis. Further work on analytical treatments based upon physical models of heat flow and nucleation and growth kinetics has also been advanced to allow for the development of an understanding of the competitive solidification kinetics that controls the formation and evolution of metastable phases and novel microstructures. New capabilities for experiment and analysis have also been established in the examination of controlled nucleation catalysis, thermal stability of metastable structures, the influence of composite reinforcement particles to modify the solidification pathway and the development of solidification microstructural maps.

While progress has been made, there are still important challenges to understanding that remain to be addressed in the solidification of highly undercooled liquids. For example, the reliable prediction of nucleation control of structure selection is an open issue, but there are developments in experiment and analysis that offer promise for new predictive capability. Although the experience in rapid solidification has increased, it is certainly not a mature area. New advances continue to be made. Some developments represent totally new observations and others represent a better understanding of reported behavior. Beyond the potential for innovative applications, rapid solidification has provided an experimental vehicle and a stimulus that has pushed the limits of the basic understanding of structure development. These developments have

a wide impact on a range of processing applications including spray deposition, surface melting, soldering and composite fabrication.

I. BACKGROUND

I.A Droplet-emulsion Undercooling Technique

A large continuous sample of liquid metal contains a variety of catalytic nucleation centers which acts to preclude the attainment of high levels of undercooling prior to solidification. Since crystallization will be catalyzed by the most potent nucleation site present, a means of circumventing the effect of catalytic sites such as oxides or container walls is necessary in order to observe extensive undercooling. Following from this basis, an effective approach to obtain large undercoolings is to disperse the bulk liquid into a collection of fine droplets which effectively isolates potent nucleation sites into a small fraction of the droplet population. The effect of these catalytic sites will then be restricted to the few drops in which they are located. The high purity liquid sample is dispersed within a suitable carrier fluid, and droplet independence is maintained by the formation of thin, inert surface coatings which are not catalytic to crystallization. When a sample of liquid metal in the form of a stabilized droplet emulsion is cooled, those droplets containing potent nucleants will freeze at low undercoolings, but the majority will not freeze until reaching the maximum nucleation undercooling level which can range from 0.3 to 0.4 T_m [11].

In considering the droplet approach to undercooling, a distinction should be made between the several modifications of this technique which have been employed by a number of investigators in the past. For example, in the droplet substrate method [9], a small sample of liquid metal is placed on an inert glass substrate in a chamber with an inert reducing atmosphere. With this approach, the onset of solidification is determined by visual observation of the change in surface reflectivity of a metal droplet which is about 50-100 μm in diameter. In the entrained droplet technique [12], a bulk alloy sample is equilibrated in a liquid-solid two-phase field with the temperature and alloy composition selected so that only a small fraction of the volume will be liquid. Since the liquid phase is in contact with the primary solid solution, which is a potential heterogeneous nucleant, the undercooling achieved with this sample configuration would be expected to be smaller than that attained using techniques in which the liquid is not in contact with an active catalyst. In addition, several other procedures have been developed for generating liquid metal droplet dispersions which exhibit a propensity for substantial undercooling. These droplet forming techniques include exploding wires [13], shotting [14] and

the containerless solidification in drop tubes [15]. While the majority of droplet undercooling schemes have a provision for some method of temperature measurement, the undercooling tendency of liquid metal droplets in most atomization methods is usually judged from microstructural observations.

Another approach for bulk samples uses the removal of active nucleation sites from the melt to achieve high levels of undercooling. The removal of catalysts is usually accomplished by physical separation of the sites from the liquid or by chemical treatment which acts to incorporate or deactivate possible catalytic sites in the presence of a chemical containment layer. These approaches include the containment of a liquid sample in an inorganic glass [8,16] as well as the levitation of a bulk melt using induction [17] and have demonstrated that in some cases, large levels of undercooling (of the order of $0.2 T_m$) may be achieved. The layer of glass encasing the melt is believed to promote undercooling not only by isolating the liquid from catalytic sites present on the crucible walls, but also by a possible scavenging action of nucleation centers that may be distributed within the volume of the melt.

Besides these specific undercooling techniques, it is clear that atomization of liquids is a commercial RSP method which incorporates an effective nucleant isolation operation as well as rapid quenching.

In principle, the droplet emulsion method of sample preparation appears to offer a relatively simple means of isolating internal catalysts which tend to promote nucleation of the solid at low levels of undercooling below T_m . In fact, samples of liquid metal in the form of droplet emulsions have yielded undercooling results which exceed the values reported by any other undercooling method (such as the droplet substrate or encased melt techniques) by a large margin [11]. In practice, the effectiveness of the dispersion operation appears to be limited by the nature of the surface film and the droplet supporting medium. It appears clear that the liquid metal-substrate (i.e. coating) interaction is important in determining the level of undercooling observed prior to nucleation [2,4,18]. Similarly, a variety of possible surface films consisting of different metal oxides, sulfides, and salts may be formed on liquid droplets, but the selection of a suitable film that is inert in catalyzing nucleation is quite difficult as is the selection of a suitable inert, stable carrier fluid. In general it is desirable that the liquid wet the coating more effectively than the solid so that amorphous coatings appear to be preferable. At the same time the coating/carrier fluid surface energy must be low to allow for a high degree of dispersion that is necessary for effective emulsification. However, there is at present, no set of well established guidelines to follow in selecting a satisfactory inert coating film for a particular metal or alloy. Nevertheless, the acquired experience in applying the droplet emulsion technique has indicated

that film coatings can be generated on a variety of different metal surfaces which permit the attainment of the largest reported maximum undercooling limits [4,11].

Furthermore, the experience gained from earlier work on relatively low melting point metals ($T_m < 500^\circ\text{C}$) using organic carrier fluids has permitted the extension of the droplet emulsion technique to high melting point metals [6,19]. With the current experience it is now possible to prepare droplet emulsion samples in molten salt fluids from alloys with melting points up to 1100°C (including Cu-based alloys) which exhibit large undercooling values. A further extension of the droplet technique now allows for direct measurement of the effect of cooling rate on the undercooling potential of the liquid. Nucleation temperatures can now be measured for cooling rates approaching $10^3^\circ\text{C}/\text{sec}$. In addition during the current program advances in droplet sample preparation have established the capability to examine composite droplet samples containing solid particles-liquid metal mixtures. Such samples are produced by either in-situ particle formation in emulsified droplets or by dispersing a bulk melt containing incorporated particles. This development represents a major advance in the application of droplet samples to study melt-particle interactions that govern the kinetics during solidification processing of metal matrix composites and is a good example of the versatility of droplet samples in studying solidification processing. On the basis of the experience of continued development of the droplet emulsion technique both in terms of achieving increasing undercooling limit values and in terms of extending the upper working temperature and the range of alloys that can be examined, it is expected that further developments and improvements in undercooling capability and in the variety of alloys and composites that can be studied will be made during the proposed program.

I.B Thermal History Behavior

Understanding microstructural evolution during rapid solidification of an undercooled melt requires a consideration of the effects of recalescence which results from the rapid release of the latent heat of fusion. For an undercooled liquid droplet (which can be assumed to represent an adiabatic system [20]) the maximum temperature reached during recalescence, T_R^{max} , is governed by thermodynamic considerations: the latent heat of fusion, the specific heat of the sample, and the degree of undercooling prior to the onset of crystallization. For a binary alloy, if the undercooling is large enough so that T_R^{max} is less than the T_0 temperature, the liquid is said to be hypercooled, and the entire droplet may solidify in a partitionless manner. However, since the hypercooling condition is not frequently achieved (even for the high liquid undercooling levels attained with the DET), the solidification of undercooled melts will usually involve a stage which occurs once T_R exceeds T_S during which the growth rate of the solid is much slower.

That portion of the droplet which freezes during this stage of solidification can exhibit a segregated solidification pattern as opposed to the compositionally homogeneous solid which forms prior to recalescence above T_S .

A schematic representation of recalescence behavior is shown in Figure 1 for an alloy of composition C_0 . This representation assumes solidification by slow cooling in an adiabatic system. The liquid of composition C_0 is slow cooled along path 1, and upon reaching point 2 at a temperature $T_N > T_N^{\text{hyp}}$ the undercooled liquid begins to solidify forming solid of composition C_0 . As solidification is occurring heat is released sufficient to reheat the sample (along path 3) until a maximum temperature T_R^{max} is reached, at which point cooling of the sample continues since the sample is in a surrounding environment at a temperature of T_N (due to adiabatic assumption, environment is not allowed to change temperature as a result of recalescence). Cooling of the sample from T_R^{max} results in the solidification of the remaining liquid fraction of the droplet according to the usual alloy solidification pathway [21]. The result will be solute partitioning in that portion of the droplet solidified after T_R^{max} , with compositions of liquid and solid in equilibrium at the interface varying, respectively, along the liquidus and solidus curves from T_R^{max} to $T_S(C_0)$ (path 4). Thus the post-solidification droplet would be expected to consist of an initial fraction solid of uniform composition and the remainder of the droplet with a segregated structure (possibly dendritic) resulting from solute partitioning along paths 3 and 4 in Figure 1. As the droplet recalesces above T_S , the C_0 solid which formed during the initial stage of solidification becomes metastable with respect to formation of a two-phase mixture of solid + liquid with compositions given by the equilibrium phase boundaries. Therefore, once T_R exceeds T_S , an important factor controlling T_R^{max} is the kinetic stability of the C_0 solid with respect to melting. For this reason, the melting behavior of an initially homogeneous solid solution alloy during continuous heating was examined as a function of upquenching rate. The metastable melting behavior has been demonstrated for Sn-Bi alloys which were carefully prepared as homogeneous tin-rich solid solutions prior to continuous heating at different rates [13]. As the applied heating rate increased an additional thermal signal between the solidus and liquidus temperature was detected which remained invariant with further increases in heating rate. The plot of these metastable melting events as a function of composition is shown in Figure 2 superimposed on the portion of the phase diagram. The calculated T_0 curve based upon a dilute solution approximation is also shown for comparison and indicates good agreement between the measured invariant metastable melting event and the T_0 curve.

I.C Dispersed particle catalysis

In almost all solidification processes, the crystallization of a bulk liquid volume occurs through favorable interaction between the melt and internal or residual catalysts which act as heterogeneous nuclei. The heterogeneous sites can be melt impurities or other external catalysts inherent to most casting processes. To a large extent the heterogeneous sites ultimately control the initial solidification structure type, size scale, and spatial distribution of product phases.

Effects induced from heterogeneous nucleation catalysis also exert a strong influence on the resultant grain size, phase morphology and compositional homogeneity as well. In order to modify and refine the as-cast solidification microstructure, it is common practice to intentionally inoculate a melt with particle catalysts that surpass the catalytic activity of other less potent heterogeneous nuclei in contact with the bulk liquid. By using this inoculation procedure, the added catalysts can promote the nucleation of a refined primary phase, alternative product phase morphologies, or the formation of fine equiaxed as-cast grain structures with enhanced mechanical properties.

There is a wide commercial application of cast alloy treatments that modify the initial solidification characteristics to provide a means for effective control of grain size and morphology. Examples include the addition of ferrosilicon to cast iron in order to promote the nucleation of graphite; Zr or C can be added to refine Mg alloys; P is introduced to Al-Si alloys to refine the primary Si phase size; As or Te can be added to Pb alloys; and Ti is added to Zn based systems. Other additives, such as Na in Al-Si alloys, are used to modify the growth morphology. In addition there is also a wide body of experience on the grain refinement of Al based alloys by Al-Ti and Al-Ti-B melt additions [22-34].

While the success of inoculation procedures is clearly established, the actual performance of inoculant additions in practice exhibits a fair amount of variability. For example, Al-Ti and Al-Ti-B master alloy additions that refine Al alloys are relatively complex and minor changes in the manufacturing process used to prepare them can result in significant differences in their effectiveness [30, 35, 36]. Moreover, even though there is a broad data base of literature concerning grain refinement processing, an understanding of the actual mechanism(s) by which grain refining agents operate in a melt still remains uncertain.

The basic requirements for an effective nucleating agent can be assessed from consideration of nucleation theory [37-39]. In order to promote the formation of crystals on an intended nucleant, the interface between the nucleant and the liquid should be of higher energy

than that between the nucleant and the solid. This condition is maximized by providing nucleant-solid crystallographic relationships that result in low disregistry orientations between the respective lattices. In fact, the potency of a given catalyst is believed to be increased for decreasing values of relative lattice disregistry with the crystalline phase, and results in solidification at lower levels of undercooling. However, under conditions of poor crystallographic fit, a reduction in interfacial energy may occur through chemical interaction [37], electronic interaction [40], or the formation of interfacial compounds and adsorbed reaction layers that are experimentally associated with much larger levels of undercooling [12, 38, 41]. In addition to the basic requirement of lattice stability, to insure effective catalysis of solid, the melt should tend to wet the surface of the nucleant. Improved mutual wetting characteristics are generally associated with a decrease in substrate-liquid interfacial tension and can be affected by parameters such as substrate surface roughness [42-44], substrate porosity [45], temperature [46-47], and adsorption phenomena induced by increased chemical affinity at the interface [48] or impurity effects in the liquid and surrounding atmosphere [49-51].

As an additional prerequisite for inoculant particles used as grain refining agents, the onset of solidification should not be followed by a rapid crystal growth, to allow the full effect of the potential nucleants to be realized. In alloys the growth restriction may be achieved as a consequence of solute redistribution during freezing which allows for nucleants dispersed throughout the melt to become effective and favors an equiaxed grain structure [24, 52, 53].

Within these general requirements, a number of compounds appear to act as effective catalysts for the nucleation of Al with disregistry values below 10% and nucleation undercoolings of less than $\sim 5^{\circ}\text{C}$ [26, 29, 31, 54]. However, the exact identities of the active nucleants have not been established by direct observation, but rather the operative nucleants have been inferred from thermal and structural results obtained from standard bulk refinement tests.

The issue of specific nucleant identity is crucial when it is considered that in commercial melts, a broad spectrum of catalysts exists that may operate singly or together to yield crystallization events. The presence of uncontrolled nucleation sites can yield irreproducible catalysis results that are related to the sample environment and the population of internal particles which may be comprised of several different structural types with variable sizes, size distributions, and surface conditions. For example, in Al castings containing refining agents which approach ideal effectiveness, the number of grains in a casting should approach the total number of inoculant particles added to a melt. However, from actual ingot grain density measurements in Al alloy castings containing inoculant additives, a grain density corresponding to only 1-2% inoculant particle effectiveness is usually observed [30]. Also, it appears that small

amounts of V, Cr, and Zr can act to poison catalytic particle surfaces [25, 30, 55].

Since the nucleation and growth characteristics of grain refinement indicate a sharp selection of particles in terms of refinement effectiveness, it is important to investigate and identify the parameters that influence the catalysis of grains and the specific physical mechanisms that govern heterogeneous nucleation processes. With bulk melts and uncontrolled sample environments, it is not clear that such a study can be accomplished in a reliable manner.

However, by using the DET to produce droplet emulsions containing incorporated particle catalysts, residual catalytic interaction between intended nucleation sites and residual sites present in bulk samples and their environments are eliminated. In addition, the ability to produce changes in droplet coating chemistries allows for the assessment of secondary interaction between the particle catalysts and the applied droplet surface coatings. Analysis of secondary interaction allows for the assessment of the true catalytic potencies of intended inoculants by using differential thermal analysis (DTA) [56]. Moreover, because inoculant particles are isolated into individual droplets within an emulsion sample, the DET has been used to produce powders of commercial Al master alloy grain refiners. DET processing of master alloys results in the incorporation of effective and ineffective catalyst particles within discrete droplets [57]. This technique used in conjunction with analytical x-ray and microbeam studies has allowed for the subsequent identification of chemical and morphological differences between the catalytically potent and ineffective particle species for the first time in commercial grain refiners [58].

I.D Design of high temperature Al alloys

As a result of an extended effort in a number of laboratories a new generation of advanced high temperature-high strength Al alloys has evolved through the direct application of RSP. Among these developments several alloys classes have been shown to be suitable for temperatures up to about 325°C including Al-Fe-Ce[60], Al-Fe-Mo[61], Al-Fe-V-Si[62] and Al-V-Zr[63]. In all cases alloying additions yield intermetallic phase dispersoids (both stable and metastable) that display very low solubility in Al. The strengthening dispersoid phases are present in fairly large volume fraction (i.e. 20-30%) as a direct result of RSP to form a supersaturated solid solution or to use the liquid phase to solutionize the solute and allow dispersoid formation to initiate on a fine scale during solidification. From this base of experience, it is now recognized that in order to maintain a high volume fraction of fine scale particles in an Al matrix at relatively high temperature, it is essential to apply an alloy design that minimizes the effects of coarsening on the particle size distribution.

The essential features of the design strategy may be illustrated by examining the LSW[64, 65] model for volume diffusion controlled coarsening where the average particle size \bar{d} varies with time, t , as

$$\bar{d}^3 - \bar{d}_0^3 = \frac{K \gamma_{\alpha/\beta} D_B C_B \bar{V}_\beta^2 t}{kT}$$

where \bar{d}_0 is the initial size, K is a constant, $\gamma_{\alpha/\beta}$ is the particle matrix interfacial energy, C_B is the solubility in the matrix, \bar{V}_β is the partial molar volume in β and kT has the usual meaning. Therefore, for a volume diffusion controlled process the effect of coarsening is minimized by reducing the $(\gamma_{\alpha/\beta} D_B C_B)$ product to as low a value as possible. For the most promising high temperature Al alloys, C_B is at very low levels and the D_B values for transition metal [66] and rare earth [67] solutes are also small so that much attention has been focused on $\gamma_{\alpha/\beta}$. Indeed in several detailed studies of the relative coarsening behavior a clear and consistent trend has emerged [68]. The lowest coarsening rates are associated with intermetallic particle dispersions which may be expected to have the lowest values of $\gamma_{\alpha/\beta}$ based upon a low lattice misfit between the particle and Al.

Based upon the current experience it appears that the lowest coarsening rate is achieved with particles that have an $L1_2$ structure and low misfit with Al. In addition a comparable coarsening behavior or somewhat slower coarsening is reported in Al-Fe-V-Si alloys where the dispersoids are based on $Al_{13}(Fe,V)_3Si$ and $Al_{12}(Fe,V)_3Si_2$ complex silicides which also may have a low interfacial energy with Al. It is interesting in retrospect to note that the finding of an $L1_2$ dispersoid phase in Al as a favorable alloy design is analogous to the combination of $Ni_3Al(L1_2)$ in Ni which is the foundation of Ni-base superalloys. In Al-Zr, Al-Ti, and Al-Zr-V where the attributes of $L1_2$ particles were established initially processing limitations restricted the maximum volume fractions to under 5%. While the processing limitations were not quantified it seems clear that these systems exhibit peritectic reactions with steeply rising liquidus temperatures to increase the level of supersaturation to achieve high volume fractions of dispersoid phase requires an increasing liquid undercooling. Moreover, due to recalescence effects attempts to increase the supersaturation level may yield non-uniform solidification microstructures. In order to address the solidification processing limitations it is useful to consider another class of solute addition based on rare earth metals that develops an $L1_2$ structure, but also exhibits a eutectic reaction with Al. In this case, of course, liquidus

temperatures exhibit a shallow decline until hypoeutectic compositions are reached so that high levels of supersaturation are facilitated. At the same time it is important to define the extent of the coupled zone, where cooperative eutectic growth develops, especially for hypereutectic compositions to which the coupled zone may be displaced [69]. In addition, for hypereutectic compositions other intriguing possibilities exist for novel control of the solidification microstructure that warrant investigation. For example, for an $L1_2$ Al_3RE ($RE \equiv$ Rare Earth) phase with low misfit with Al, the particles may be expected to promote efficient grain refinement. This has been demonstrated with Al_3Sc , but unfortunately Sc is quite expensive. In this case, at high undercooling a high density of fine Al_3RE particles can develop as a primary phase with each particle promoting the nucleation of Al during further cooling and effectively modifying the development of a cellular/dendritic structure that is usually observed in systems where the intermetallic particle lattice is not closely matched to Al.

II. RESEARCH ACCOMPLISHMENTS OF THE CURRENT PROGRAM

During the current program, research has been focused upon metastable phase formation and the controlling phase selection reactions, the evolution of solidification microstructure under the combined influence of undercooling, heterogeneous nucleation sites, recalescence and external cooling and several other aspects of undercooled alloy solidification and product structure stability. The experimental approach that has been applied to carry out these studies is based on the droplet emulsion technique. With this method, samples may be produced which exhibit large undercoolings prior to solidification during slow cooling ($10-30^\circ C/min$) and which may be maintained in the metastable undercooled state for extended time periods without the intervention of crystallization.

At deep undercoolings equilibrium crystallization reactions may be bypassed and metastable solid phases can be produced during freezing. With thermal analysis and x-ray diffraction measurements it has been possible to examine the undercooling conditions for metastable phase formation and to elucidate the kinetic competition during crystallization. Often, the microstructural morphology and the structure of product phases that solidify from the melt have features which are distinct to high undercooling solidification. Several examples of fine-scale eutectics, multizone structures, and ultrafine dispersoids as well as uniform, supersaturated solid solution morphologies have been identified in droplet samples.

For selected reactions it has been possible to identify the solidification path for crystallization from the undercooled liquid state. With samples containing known nucleation catalysts, thermal analysis and x-ray diffraction study has been used to identify a path for the

generation of supersaturated solid solutions and metastable intermediate phases. Based on these findings it has been possible to develop a framework for describing the reaction paths followed during high undercooling solidification in terms of metastable phase diagram constructions [70]. In one case for the Sn-Sb system a fairly detailed and complete experimental measurement and thermodynamic modeling evaluation of the stable and metastable equilibria has been performed [87, 88]. Which has exposed new behavior during peritectic solidification and the development of supersaturated solid solutions in peritectic systems at high undercooling. In another study on solidification in undercooled Al-Y eutectic alloys, two new structural options have been identified which offer intriguing opportunities for microstructural design. For Al-rich alloys a metastable ordered phase with an $L1_2$ structure has been synthesized and has been shown by TEM observations to retain coherency with the Al matrix after elevated temperature exposure. For intermediate alloy compositions it has been demonstrated that the stoichiometric Al_2Y line compound can be extended to a significant single phase region with composition range of about 20at%Y. The synthesis of supersaturated line compounds represents a new option as a precursor to the development of fine-scale multiphase microstructures.

In a complementary examination, the use of droplet samples with controlled undercooling levels and known nucleation catalysts has permitted the documentation of new features governing heterogeneous nucleation [56]. For example, it is often considered that the lattice registry in a hetroepitaxial relationship between a catalyst surface and the nucleus is the key to controlling heterogeneous nucleation undercooling, at least at low undercooling. However, at high undercooling there is now clear evidence that a chemical interaction at the catalyst surface is important in establishing catalytic potency. Some of the implications of chemically controlled catalysis for wetting behavior during soldering and solidification processing of composites have also been explored in an initial study.

Several new applications and analysis methods involving droplet samples have also been advanced during the current research. A new perspective on rate effects has been established to allow for the measurement of nucleation undercooling temperatures at cooling rates approaching $10^3^\circ\text{C}/\text{sec}$. These results have been coupled with a nucleation kinetics model and measured thermodynamic properties to provide a quantitative assessment of the measurement requirements for reliable analysis of nucleation rates [71]. Moreover, new observations on heterogeneous nucleation during continuous cooling indicate that the usual model analysis assumption of a static catalyst/melt interface is not valid in all situations. The influence of catalyst/melt interface dynamics (i.e. step structure) on nucleation behavior can be monitored by the measured kinetic responses in droplet samples. An important advance in the development of solidification

microstructure maps for rapid solidification has been achieved in the Fe-Ni system where an analysis has provided a unified interpretation of microstructure evolution in samples spanning seven orders of magnitude in volume.

Several advances in experimental capability have been established during the current work. An important development in the controlled upquenching of droplet samples has provided a direct measurement of metastable phase boundaries and the first reports of T_0 measurements [72]. A new level of detection sensitivity in thermal analysis has been established to allow for the measurement of thermal signals from only 50 droplets and may be increased further with optical fiber methods. Besides dynamic experiments, new capability has been added for *in-situ* analysis of phase selection and the thermal stability of product structures with an x-ray diffraction system that is equipped with a position sensitive detector for rapid data acquisition at elevated temperature.

In addition, the droplet technique has also been modified to allow for analysis of the catalytic potency of various compounds for nucleation of a metallic phase through the incorporation of inoculant particles into the droplets during emulsification [56]. This technique is currently being used to evaluate the effectiveness of Al grain refining master alloys [57] and has been extended to permit the examination of reinforcement particle/melt interactions that influence the solidification processing of metal matrix composites.

In the following sections, a description is given of the results of the current areas of study. When these findings are viewed together, several new features of the solidification of highly undercooled alloys can be identified from the droplet studies. The significance and implications of these observations are discussed in terms of the factors determining the rate of solidification, the phase selection process for the solidification products, and the microstructural evolution. A consideration of the results is of value not only in demonstrating the unique potential of the droplet technique, but also in providing the necessary background for the further development of the application of the droplet method to study the solidification of undercooled liquid alloys.

II.A Undercooling Behavior of Pure Metals

The droplet emulsion technique has proved to be a very effective means of attaining high levels of liquid undercooling. Present experience with the droplet method has identified a number of processing parameters that are likely to govern the optimization of undercooling in powder samples [73]. These processing variables include droplet size refinement, sample purity, droplet surface coating, uniformity of coating, cooling rate and melt superheat as well as alloy

composition and applied pressure. Although the influence of these processing variables has been demonstrated with droplet experiments, the results are general and are expected to apply to other processing methods where direct measurement and control of solidification is more difficult.

The effect of the various processing parameters on the undercooling response is summarized in Table 1. Even when these processing conditions are satisfied to produce maximum undercooling, experience suggests that solidification is still initiated by a heterogeneous nucleation site associated with the sample surface [74].

Table 1

Parameter	Undercooling Response	Remarks
Droplet Size	Increased ΔT with size refinement at constant T	Nucleant isolation follows Poisson statistics
Droplet Coating	Function of coating structure and chemistry; major effect in limiting ΔT	Most effective coating is catalytically inert
Cooling Rate	ΔT generally increases with increasing T	Changing T can alter the nucleation kinetics
Melt Superheat	System specific	Appears to be related to coating catalysis
Composition	T_n follows trend of T_L	Melt purity not usually critical
Pressure	T_n parallels melting curve trend	Change in response can signal alternate phase formation

Therefore, it appears that close attention to the nature of the powder surface coating is of prime importance in achieving reproducible, large undercooling values in fine powders. The maximum undercooling limits for several pure metals measured using thermal analysis are listed in Table 2.

Table 2

Element	Previous Studies		Reference	Current Studies	
	ΔT ($^{\circ}\text{C}$)	$\Delta T/T_m$		ΔT ($^{\circ}\text{C}$)	$\Delta T/T_m$
Al	130	0.14	Turnbull and Cech (1950)	175	0.19
Sb	135	0.15	Turnbull and Cech (1950)	210	0.23
Bi	90	0.16	Turnbull and Cech (1950)	227	0.41
Cd	-	-		110	0.19
Ga	150	0.50	Bosio et al. (1966)	174	0.58
In	-	-		110	0.26
Pb	80	0.13	Turnbull and Cech (1950)	153	0.26
Hg	80	0.34	Turnbuil (1952)	88	0.38
Te	-	-		236	0.32
Sn	117	0.23	Pound and LaMer (1952)	191	0.38

Based upon the comparison presented in Table 2, current studies have demonstrated clearly that the previous maximum undercooling values actually correspond to heterogeneous nucleation conditions. Indeed, the present findings emphasize that further nucleation kinetics studies are necessary before a complete characterization of the revised undercooling limits in terms of heterogeneous or homogeneous kinetics is possible.

II.B Solidification of Al Alloy Powders

A similar influence of powder processing parameters has also been found to prevail in the treatment of Al-rich alloys as well. The solidification microstructure that develops in Al alloys has been documented to be related closely to the initial level of undercooling at the onset of solidification [75,76]. Of course, with alloy solidification the available pathways for freezing from an undercooled state involve a variety of options. In this case, the microstructural and thermal history capabilities that can be applied in the controlled solidification of powder samples produced from the DET are of particular assistance in identifying the operative pathway under a given set of processing conditions. A number of the RSP pathway options can be analyzed by examining the solidification of droplet samples in several Al alloy systems, some of which offer useful potential for dispersoid formation.

Through the control of melt undercooling in Al alloy droplet emulsions, highly dispersed phase mixtures have been produced in several alloys through various phase separation reactions.

fine scale eutectic growth, precipitation of phases from supersaturated solid solutions, and from the decomposition of metastable phases [77]. In addition, the microstructural morphologies that develop during the solidification of the undercooled Al alloy droplets under slow cooling conditions are also comparable to the structures that evolve during the rapid quenching of atomized powders. Therefore, the information obtained from the alternative solidification pathways and the current experience with Al alloy droplets has allowed for favorable microstructures to be developed and can be used as a basis for effective RSP alloy design. In addition the Al-Y and Al-Be alloys have produced results that have increased our understanding of using the DET with alloys containing highly reactive elements. The DET under unfavorable conditions can "purge" the reactive elements from the powder. The purging effect can be uniform throughout the sample volumes as in the Al-Be system or can be random as in the Al-Y system. Initial work has demonstrated that this purging effect can be changed by certain processing parameters such as salt, cover gas and composition.

As part of a continuing study of Al alloy systems that offer the potential for the development of large volume fractions of fine dispersoid phases with high temperature stability the current focus has been directed towards Al-rich Al-Y alloys. As shown in Figure 3 the Al-Y system exhibits a eutectic between Al and Al_3Y at about 3.1at%Y and Al has a maximum equilibrium solubility of less than 0.03at%Y [78]. The alloying effects of Y are of interest in several respects. First, Y_2O_3 is more stable than Al_2O_3 so that Y additions may be expected to modify surface coatings which in turn will influence the undercooling and solidification behavior. Secondly, several metastable phase effects have been reported including significant supersaturation of Y in Al solid solution [79], a substantial increase in the solubility range of Al_2Y (C15) [80] and the development of a metastable L_{12} structure phase [81]. Along with the DET process other RSP techniques as two-piston anvil splat quenching and single roller melt-spinning have been used to access metastable phase formation in Al-Y alloys and to explore a range of solidification processing conditions.

A partial Al-Y binary phase diagram indicating the range of compositions studied and the phases that were formed is given in Figure 4. In the region of the Al rich eutectic x-ray diffraction analysis, and TEM analysis indicate the development of a metastable L_{12} phase. The lattice parameter of the L_{12} phase, presumably Al_3Y in stoichiometry, was determined to be 0.4234 nm. The observed lattice parameter of the L_{12} phase in the Al-Y system is similar to those observed for the Al_3Ho and Al_3Dy compounds exhibiting the L_{12} crystal structure at elevated pressure where L_{12} lattice parameters are 0.4230 nm and 0.4236 nm respectively [82]. In other work the lattice parameter of Al_3Y in the L_{12} crystal structure was calculated to be

0.423 nm[83]. Initial TEM results indicate that the $L1_2$ particles are coherent with the matrix and are potent dispersion strengtheners [84]. Thermal cycling of the Al-3at%Y sample showed an exothermic signal on first heating at around 240°C corresponding to the decomposition of the metastable structure. However, some of the $L1_2$ crystal structure was still detectable by XRD following heating of the sample to 550°C in the DSC. This is illustrated in Figure 5, which consists of an XRD trace of the Al-3at%Y sample in the as-solidified condition and in the post thermal cycling condition. It should be noticed that the relative intensity of the $L1_2$ {111} reflection decreases after thermal cycling and reflections of the β -Al₃Y phase become evident. The continued detection of the $L1_2$ phase with XRD after heating to 550°C in the DSC, suggests that many of the particles retain coherency with the matrix, moreover the potential for a large volume percent of second phase particles indicates that the alloy system is worth investigating further for its possible elevated temperature capabilities.

An important issue to resolve in the continuing studies is related to the solidification pathway for formation of the metastable $L1_2$ phase in undercooled Al-Y samples. There have been two possible pathways that can be identified based upon the current work. The first consisting of supersaturation of the aluminum primary phase with subsequent solid state precipitation and growth of $L1_2$ particles. Supersaturation of the aluminum phase would require extensive undercooling for the hypereutectic alloys due to the rising liquidus of the Al₃Y phase. The second mechanism consists of nucleation of the $L1_2$ phase perhaps at a non-stoichiometric composition from the liquid and subsequent growth of the $L1_2$ with the last liquid to freeze being slightly supersaturated primary aluminum. An examination of the possible metastable phase boundaries suggests that this pathway may only require a modest undercooling; especially if the initial $L1_2$ phase formation develops above the eutectic (Figure 3). Further study is required in order to determine positively the actual solidification pathway so that strategies can be developed to optimize the yield of the metastable phase.

In the region of the reaction $L + Al_2Y \rightarrow Al_3Y$ the formation of a highly supersaturated Al_2Y phase with the C15 Laves structure was observed. X-ray diffraction traces obtained in the transmission mode of the Al-18.1at%Y sample in the as-solidified condition (trace A) and the post DSC condition (trace B) are shown in Figure 6. From trace A it is apparent that Al_2Y is the major phase present with a small volume fraction of Y_2O_3 and peaks that correspond to the reported $Al_4Y/Al_{11}Y_3$ structure [120]. The $Al_4Y/Al_{11}Y_3$ structure is not reported to be an equilibrium phase in the Al-Y system [78]. Moreover, the metastable $Al_4Y/Al_{11}Y_3$ structure does not exist in the x-ray diffraction trace of the post DSC sample.

From the x-ray diffraction trace B in Figure 6 it is apparent that β -Al₃Y is the major

phase present along with a small amount of Y_2O_3 and primary Al. It should be noted that all of the samples decomposed to $\beta-Al_3Y$ instead of the low temperature polymorph $\alpha-Al_3Y$ even with repeated heating cycles to $600^\circ C$. In contrast, the current versions of the Al-Y phase diagram would predict the decomposition product to $\alpha-Al_3Y$.

The observed lattice parameters of the C15 Laves phase for each sample where the composition was determined by EDS analysis are shown in table 3 and are plotted in Figure 7 along with the reported lattice parameter of stoichiometric Al_2Y (0.7855 nm) [85].

Table 3

Sample Composition (at%Y)	Lattice Parameter of Al_2Y (nm)
Al-18.1Y	0.7780 ± 0.0002
Al-23.4Y	0.7818 ± 0.0008
Al-24.3Y	0.7821 ± 0.0001
Al-31.8Y	0.7844 ± 0.0003
Al-43.8Y	0.7867 ± 0.0007

From Figure 7 it is apparent that the observed lattice parameter of the C15 Laves phase decreases in a linear manner with increasing Al content in the sample. While, the observed lattice parameter of the C15 Laves phase increases with an increase in Y content from stoichiometry. The observed lattice parameter of Al_2Y in the Al-31.8at%Y sample in the post DSC condition involving decomposition above $400^\circ C$ and the reported lattice parameter of stoichiometric Al_2Y are 0.7852 ± 0.0004 nm and 0.7855 nm respectively [85]. In agreement with the reported phase diagram it appears that at equilibrium Al_2Y has little departure from stoichiometry [78]. The change in lattice parameter also indicates that the Al_2Y phase is in a supersaturated condition in the as-solidified sample. From the current work, a substantial amount of supersaturation can be confidently shown to exist and the extent of supersaturation observed can be reasonably determined as indicated.

The linear relationship of lattice parameter versus composition seen in Figure 7 compares favorably to what is seen for Vegard's simple solute substitution model. This would seem to indicate that the supersaturation of Al in the C15 lattice is substitutional. The amount of supersaturation observed on the Al rich side of stoichiometry is greater than the amount of supersaturation on the Y rich side of stoichiometry. This can be explained by the difference in the size of the atoms. From a geometrical standpoint it would be easier to place an aluminum

atom on a yttrium site than it would be to place a yttrium atom on an aluminum site, because the aluminum atom is smaller.

Two simple relationships can be established to model what the change in lattice parameter versus composition could follow using the packing factor of the C15 crystal structure, the Goldschmidt radii and the ideal atomic radii determined from the crystallography of the {110} plane shown in Figure 8. Using the reported lattice parameter 0.7855 nm and the geometric configuration for Al and Y respectively shown in Figure 8 the ideal atomic radii are calculated to be 0.1389 nm and 0.1701 nm for Al and Y respectively. The Goldschmidt radii are given to be 0.143 nm and 0.181 nm for Al and Y respectively [86]. The observed lattice parameters of the samples is plotted along with the calculated relationships in Figure 9. The slope of both relationships are greater than the slope observed for measured lattice parameters, but the trend is the same. The model using the calculated ideal atomic radii is taken to be the best model of the two since it produces a value closer to the reported lattice parameter of the stoichiometric composition. The linear manner of the data and the similarities of the calculated relationships appears to indicate that near partitionless solidification occurred in the samples and the supersaturated Al_2Y formed is at or near the respective alloy compositions.

The development and extent of supersaturation for the Al_2Y phase which is essentially a line compound at equilibrium raises a number of questions and also exposes some intriguing opportunities for controlled solidification processing microstructures. First the usual experience with line compounds is to expect the T_0 curve to be steeply falling with decreasing temperature with a position close to the stoichiometric composition. However, when the compound has the capability to accommodate non-stoichiometric compositions by means of a defect structure in the ordered lattice, the T_0 curve may exhibit a more shallow drop with decreasing temperature. This appears to be the case for Al_2Y . Beyond the issue of the possible defect lattice structure, the rate of ordered phase crystal growth to allow for solute trapping is also uncertain, but is central in analyzing the kinetic competition between Al_2Y , Al_3Y and the metastable L_{12} phase. In this regard any information on the T_0 curve for Al_2Y obtained by upquenching experiments or other assessments would provide valuable insight. At the same time, the relatively high thermal stability of Al_2Y and the manipulation of the decomposition reaction for supersaturated Al_2Y offer unique opportunities for fine scale microstructures that can be considered for high temperature applications.

II. C Heterogeneous nucleation

The nucleation of a solid on an energetically favorable surface present within a liquid can

ultimately control the solidification microstructures and interrelated physical and mechanical properties of many materials. By examining the solidification responses generated from liquids containing a variety of identifiable catalytic sites such as primary phases, or secondary dispersed particle additions, it is possible to modify and control the solidification microstructure by altering the heterogeneous nucleation response. In order to promote a given solidification pathway via nucleation on an intended catalyst in addition to conducting a meaningful assessment concerning the actual catalytic potency of the specified agent, it is essential that all background nucleation sites more potent than the intended agent be removed or isolated from the sample. Based upon past and current experience, the DET is well suited for this purpose and can be used effectively to study heterogeneous nucleation responses generated through primary phase catalysis [87, 88]. In fact the progress in primary phase catalysis has advanced so that it is now possible to conduct detailed kinetic studies (as described in section II. E) relating to the catalysis of specific primary phase nucleation sites.

In further research concerning heterogeneous nucleation catalysis this background is being used as a basis for the examination of systems in which heterogeneous nucleation of a solid is produced through particle agents that are introduced into a melt, as a complement to catalysis reactions in which nucleation of solid is facilitated internally within the melt through the existence of a primary phase.

The addition of dispersed particle catalysts has wide commercial application as grain refining agents and as strengthening agents in composite materials as well. In order to examine factors which influence effective nucleation in systems which rely upon the use of dispersed particle additions, two investigations were performed by modifying the DET to accommodate for the production of droplets containing dispersed particles. The procedures used in conjunction with the DET have allowed for discrete identification of the active nucleation agent present within a given sample and thus provide a means to assess the potency of the active site and identify influential parameters which control the heterogeneous nucleation response. These studies include the undercooling behavior and catalytic trends associated with the nucleation of droplets of Sn and Al containing a variety of chemically different dispersed particles [56], and a specific examination of inoculant particles contained in commercial Al-Ti grain refining master alloys [57, 58].

II.C.1 Dispersed Particle Catalysis of Liquid Droplets

In order to promote nucleation from intended catalysis and obtain meaningful assessments of actual catalytic potencies of the specified agents, elimination of background

nucleation sites more potent than the intended agents is essential. The principal features of the heterogeneous nucleation sites that may be active are illustrated in Figure 10. In the schematic, site 1 is a residual or isolated impurity, site 2 is the applied droplet coating, and site 3 is a junction site involving the influence of site 4, the incorporated particle and the droplet coating (site 2) on the resolved catalytic activity. Based upon this description the nucleation undercooling will change in response to a change in surface coating when either site 2 or 3 is active. However, if the activity of the intended inoculant particle exceeds that of the applied droplet surface coating or a possible junction site between the surface coating and the intended inoculant particle (sites 2 and 3), then the nucleation undercooling associated with the particle (site 4) will be unchanged by modifications of the droplet surface coating (site 2). Therefore, by changing the droplet surface coating and monitoring the undercooling responses of droplet emulsions containing pure droplets and particle incorporated droplets, the actual catalytic potency of particle inoculants is established in terms of the operative surface interactions.

The application of this approach is illustrated in Figure 11. In Figure 11 (a), pure Sn droplets nucleate at an undercooling of 176°C . In Figure 11 (b) an emulsion with incorporated Y_2O_3 particles produced with an identical droplet coating shows the pure Sn undercooling and an exotherm associated with catalysis by the Y_2O_3 particles at $\sim 136^{\circ}\text{C}$ of undercooling, thus establishing the presence of both Y_2O_3 incorporated and Y_2O_3 free droplets within the emulsion. By using the coating check procedure it is possible to establish the identity of the catalytic sites inducing nucleation in the two sub-populations of Sn droplets. In Figure 11(c) a Y_2O_3 dispersed particle emulsion produced with a different droplet coating shows a shift in the pure Sn undercooling from 176°C to 153°C while the undercooling for droplets containing Y_2O_3 particles remains constant at 136°C . Therefore junction site activity between the applied droplet surface coating and the incorporated particles is absent and the most catalytic sites present within the emulsions are the interfaces formed between the liquid Sn and the Y_2O_3 inoculant particles surfaces. It should be noted that because a shift in undercooling with a change in coating treatments occurs in droplet free of Y_2O_3 particles, the most potent nucleation sites present in the inoculant free Sn droplet are associated with the applied surface coating.

To emphasize the importance of extrinsic site isolation in relation to obtaining reliable undercooling measurements that are representative of the actual catalytic potencies of intended agents, a Sn- Y_2O_3 incorporated droplet emulsion was prepared without the use of an applied coating to promote the formation of a uniform, thick ($> 1\ \mu\text{m}$) oxide surface film. Figure 11(d) shows a Y_2O_3 incorporated, oxide coated droplet representative of this sample and the corresponding masking effect of the true catalytic responses.

An identical experimental sequence was also used to study the catalytic effect of several other compound inoculant particles incorporated within Sn droplets as well. The nucleation catalysis results obtained from these studies are summarized in Table 4 which shows the resultant undercoolings to nucleation attained in the droplet samples that nucleated via incorporated particle catalysis. From the catalysis results shown in Table 4, it is apparent that a trend emerges in which similar chemical species of inoculant particles are shown to promote nucleation within a common nucleation temperature regime. For example, the catalyst particles Al_2O_3 , TiO_2 , Fe_2O_3 , ZrO_2 , and ZnO all promoted nucleation of Sn droplets at essentially the same level of

Table 4

Crystallographic disregistry δ and nucleation undercooling ΔT in Sn droplets containing inoculant particles			
Inoculant (I)	Orientation (β-Sn)/(I)	δ (%)	ΔT ($^{\circ}\text{C}$)
Al_2O_3	100//0001	33.2	144
TiO_2	001//101	13.8	142
Y_2O_3	101//100	31.6	136
ZrO_2	100//100	13.1	142
Fe_3O_4	110//100	13.9	142
ZnO	100//1010	7.1	139
SnO	110//001	4.6	142
SnO_2	100//110	7.6	142
CdO	101//110	9.8	97
PbO	001//101	1.2	97
MoS_2	110//0001	20.8	78
WS_2	110//0001	20.8	78
CdTe	101//100	6.8	69
Cr_2Te_3	001//0001	26.3	69
PbTe	101//100	6.7	69
SnTe	101//100	6.6	69
ZnTe	101//100	6.4	69
AlP	001//100	7.0	64
InSb	101//100	6.8	97
CaF_2	001//100	6.3	157

undercooling observed for Y_2O_3 incorporated droplets ($\Delta T = \sim 140 \pm 4^\circ\text{C}$). Moreover, the incorporation of the native oxides, SnO and SnO_2 , also produced identical nucleation behavior ($\Delta T = 142^\circ\text{C}$). Although the CdO and PbO inoculant particles were found to be more catalytically potent than the other oxides examined, nucleation catalysis also occurred at a common undercooling level which was identical in temperature to the undercooling level produced in air-oxidized Sn droplets samples as shown in Figure 11(d), ($\Delta T = 97^\circ\text{C}$, $T_n = 135^\circ\text{C}$). Similarly, the nucleation behavior of Sn droplets containing several species of telluride particles also catalyzed Sn nucleation at a common nucleation undercooling level of 69°C ($T_n = 163^\circ\text{C}$), while Sn catalysis by the sulfides WS_2 and MoS_2 also resulted in a common undercooling to nucleation at $\Delta T = 68^\circ\text{C}$, ($T_n = 154^\circ\text{C}$).

In general, effective solidification catalysis is prompted through a lowering of interfacial energy between the catalytic substrate, the liquid, and solid (nucleus) phases. Two factors that predominantly influence a lowering of this interfacial energy are a structural contribution that involves the degree of crystallographic mismatch (disregistry, δ) between preferred planar orientations of the nucleus and substrate and a chemical interaction contribution [37]. For disregistry control to dominate the nucleation process and provide for common undercooling in Sn droplets containing various inoculant particles, similar crystallographic mismatch between Sn and the various substrates promoting the common nucleation behavior is required. However, disregistry calculations used to estimate the minimum amount of crystallographic misfit between various low index planes of $\beta\text{-Sn}$ and the compound inoculant particles that are summarized in Table 4 show extensive variability and do not support a disregistry controlled nucleation process [89].

Although it is difficult to judge the exact nature of the atomic interaction at the catalyst/nucleus interface, the lack of evidence to support a structurally dominated nucleation process indicates that the observed undercooling trends are primarily dominated by chemical interaction. Moreover, the occurrence of a chemically dominated nucleation behavior resulting in common nucleation undercooling levels for Sn droplets containing chemically similar inoculant particles, is consistent with the formation of adsorbed layers or intermediate compounds of similar origin at the nucleus/catalyst interfaces as required to satisfy interfacial equilibrium. A schematic model to illustrate the operation of this catalysis mechanism is presented in Figure 12.

The body of evidence obtained from the nucleation of Sn droplets suggests that the selection of the chemically dominated nucleation mechanism is influenced by the ultimate

thermodynamic stability and crystal chemical properties of the catalytic substrate surfaces in contact with the liquid. To illustrate this behavior, the influence of inoculant thermodynamic stability in the liquid as a function of undercooling behavior is highlighted in Table 5 for oxide catalysis of Sn.

Table 5

Thermodynamic stability of oxide particles in Sn

Oxide (X_mO_n)	ΔGr_{xn1} (kJ)	ΔGr_{xn2} (kJ)	ΔT (°C)
Al ₂ O ₃	+1605	+810	144
TiO ₂	+367	+372	142
Y ₂ O ₃	+2119	+1067	136
ZrO ₂	+537	+542	142
Fe ₃ O ₄	+35	+45	142
ZnO	+141	+73	139
CdO	-87	-41	97
PbO	-139	-67	97

droplets as determined for 1) SnO₂ and 2) SnO formation at 1000K [89].

For substrates which are unstable in contact with the liquid, the formation of intermediate chemical reaction layers is favored. In addition, the experimental catalysis data also shows that these reaction layer surfaces are more catalytically potent as nucleation agents than are thermodynamically stable substrate surfaces which promote a surface interaction that is akin to chemical adsorption processes. The most effective wetting of substrate materials usually occurs through liquid/substrate interaction that results from intermetallic layer formation. It is apparent that an analogous condition has been shown to occur in particle dispersed droplets via nucleation catalysis on substrate surfaces that are subject to reduction in contact with the liquid phase.

In summary, the results of the current work point clearly to a chemically controlled nucleation catalysis when nucleation occurs under the influence of dispersed particles at significant undercooling a geometric control of nucleation catalysis involving a minimization of lattice misfit registry may dominate. However, the issue of the transition undercooling level that may separate geometric from chemical control of catalysis needs to be resolved in order to establish guidelines for the selection of the most appropriate nucleation catalysts for a given undercooling response. By extending this analysis to other particle/melt combinations the

application of the DET can allow for an identification of the controlling reaction behaviors.

II.C.2 Heterogeneous Nucleation in Al-Ti-X systems

Inoculation treatments are a commercially successful approach for the refinement of Al ingot castings. However the actual mechanisms that control the physical processes of grain refinement are not well understood. In actual practice a significant degree of refinement variability exists in the performance of inoculation agents [29-30, 35-36]. Moreover, the commercial data base suggests the grain refiner efficacy is further complicated by several phenomena such as inoculant dissolution, fading effect, settling or agglomeration of inoculant particles, impurity poisoning, etc.[30, 25, 52, 55].

In fact, many commercial Al-Ti and Al-Ti-B type grain refinement additions do not promote efficient grain refinement: bulk grain density measurements from inoculated Al castings indicate that only 1-2% of the potentially refining particles present in the master alloy actively promote and result in Al grain formation [29]. Under special conditions inoculant activity may reach 8-10% of the added refining particles, but this is still a rather poor efficiency. The usual techniques implemented to assess grain refining efficacy of a substance consist mainly on the observation of a bulk inoculated sample where quantitative metallography is applied to measure the average grain size of a casting due to different treatments. This data is then correlated with the relative grain refiner effectiveness. However, the issue of specific nucleant identity within a bulk sample cannot be addressed in a reliable way [89, 58, 90, 91] because the original solidification morphologies associated with the nucleation and growth of Al on effective particle catalysts are consumed during matrix coarsening and final solidification.

The DET method allows for the measurement of reproducible nucleation catalysis by isolating background catalytic factors in metallic droplets containing inoculant particles. This procedure, which was successfully applied to pure Sn containing Y_2O_3 particles [56], has been extended to the production and the subsequent evaluation of commercial grain refining alloys based on the Al-Ti system [89, 58, 90, 91]. To accomplish the master alloy powder production a bulk sample is placed in molten eutectic salt mixture at 800°C which acts as a carrier fluid for the liquid alloy. Emulsification is carried out at 800°C to assure that phases such as Al_3Ti , i. e. the potential nucleants, are in contact with the Al-rich liquid phase. A high speed rotating agitator generates a fine dispersion of alloy droplets dispersed within the carrier fluid. Immediately, the emulsion is quenched on a Cu or Al chill plate. Finally, the solidified salt mixture is dissolved in distilled water and the emulsified powder is separated by filtration and sorted by size. An illustration depicting this procedure is shown in Figure 13.

In Figures 14 A, B, C DTA thermograms corresponding to a commercial Al-6wt%Ti alloy in bulk and emulsified droplet samples and a high purity Al-1wt%Ti emulsified alloy sample are shown. In the commercial alloy traces three reactions are observed (Figures 14 A, B). At 672°C, i.e., above the equilibrium peritectic temperature, the initial nucleation onset indicates the presence of inoculant particles that possess an enhanced potency to promote Al nucleation. The equilibrium peritectic reaction at 665°C is promoted by the less potent catalytic particles. The low temperature reaction is most likely associated with a multicomponent eutectic growth since this reaction does not appear in the highly pure binary alloy (Figure 14 C). In the binary alloy sample, the reaction at 672°C corresponds to the Al formation on an intermediate metastable Al_xTi phase via a non-equilibrium peritectic reaction [92, 93]. The correspondence between that latter DTA trace with the Al-Ti phase diagram is shown in Figure 15. In commercial alloys the similarities of the thermal signal at 672°C again suggest the operation of a metastable peritectic reaction involving the Al_xTi phase.

An interrupted nucleation quenching treatment can be used to correlate effective nucleation catalysis of Al to specific inoculant particles incorporated within the master alloy droplets. The quenching temperatures are selected in the Al solidification temperature range accordingly with the reaction signals detected with a highly sensitive DTA during cooling cycles. Upon quenching the evolving solidification morphology is retained at any desired temperature and the preserved microstructure after appropriate etching is examined by optical and electron microscopy. Consequently, an individual DTA signal can be correlated with the transformation of phases at a particular stage of their evolution, by studying the alloy microstructure. Particularly, this method has been used to discriminate the most potent catalyst for the Al nucleation. Once the nature of the reactions taking place upon cooling has been established, a quenching experiment is performed at a temperature just below the first Al solid phase formation from the liquid. With this approach, the incipient phase with its characteristic initial solidification morphology developing on the surface of the most potent nucleant will be retained upon quenching. On the other hand, all other less potent substrates will exhibit a mostly featureless (i.e. very fine scale) surrounding Al phase formed during the quenching treatment from the parent undercooled liquid. Therefore, during SEM examinations, by pinpointing and quantifying the most effective substrate phases, classified as **active**, the general performance of the master alloy is assessed in terms of the percentage of active nucleants relative to all the present inoculant phases.

Figures 16 and 17 show the resultant quenched microstructure from 671°C of two different droplets of the same Al-6wt%Ti alloy sample. A droplet containing an active catalytic

aluminide particle with rounded Al dendrites radiating from it is shown in Figure 16 A; the evolving microstructure has been retained by quenching the powder at 671°C. Another droplet from the same sample, but containing a less effective aluminide bears a cellular microstructure produced from a still liquid alloy upon quenching (Figure 17 A). The accompanying Figures 16 B and 17 B consist of Wavelength Dispersive Spectroscopy WDS X-ray maps generated from the two types of droplets.

Two significant differences are evident between droplets containing active and inactive inoculant particles. First, a faceted morphology is associated with ineffective aluminides while an active inoculant has a more irregular shape. Secondly, quantitative microanalysis indicates that the active nucleants contain Si concentrations which range from ~4 to ~10 at.%. Meanwhile the inactive aluminides are found to be essentially Si free. X-ray diffraction examinations have demonstrated that Si atoms enter into solubility in the Al_3Ti , modifying the lattice constant so as to minimize the interfacial energy between the aluminide and the Al nuclei. The extension of the $(\text{Al},\text{Si})_3\text{Ti}$ phase field is shown in the Al-Ti-Si phase diagram in Figure 18. Chemical analysis indicates the presence of small amounts of some Si-rich phases shown in Figure 18, attributed to a non-equilibrium phase formation promoted by the manufacturing process. These results suggest in a straight-forward manner that for commercial Al-6 wt.% Ti grain refining master alloys, Si plays a key role in determining catalytic activity.

Additionally, a further inspection of the WDS X-ray maps of Figures 16 B and 17 B indicates that for the active aluminides Si is also present in the interdendritic regions and is likely involved in the solute redistribution required for growth of Al phase during quenching. In other words, a restrained growth velocity of the catalyzed Al-solid solution also collaborates with the final grain refining performance of the master alloy. Thus, the actual Si role is presumably a combination of an enhanced Si-containing substrate and restriction of growth due to solute redistribution.

On the other hand, commercial Al-Ti-B type master alloys have also been investigated to elucidate the actual effect of B in the grain refining mechanism. After emulsification, two commercial alloys containing 5 wt.% Ti-0.2 wt.% B and 5 wt.% Ti-1 wt.% B underwent DTA cycles that resulted in the thermograms depicted in Figures 19 a, b. From the traces, it is clear that both alloys, despite the significant difference in B content, produce similar reaction signals, either in absolute values of temperature or temperature ranges. The number of reactions upon heating and cooling is the same as well.

A set of quenching experiments at different temperatures (indicated in Figures 19 a, b)

was implemented in order to retain the evolving microstructure and to discriminate the actual origin of each reaction signal upon cooling. From these experiments and additional Energy Dispersive Spectroscopy (EDS) analyses, a striking similarity emerges between the thermal behavior of the B containing alloys and the commercial Al-Ti alloys containing Si. For example, in Figures 19 a, the reaction at 655°C is due to the formation of Al in the most potent substrate; the second reaction, at 648°C, is most likely the result of a peritectic transformation that produces small amounts of Al_3Ti particles and Al on the less catalytic surfaces. The low temperature reaction, at 646°C, is attributed to the solidification of a multicomponent eutectic containing small amounts of Fe, Si, etc.

The T1 quenched powders were employed to reveal the active particles that promoted the early formation of α -Al phase at the highest temperature on the most active nucleant. Figures 20 and 21 show the morphological characteristics of the retained microstructures where active and inactive nucleants are present in the droplets. Based upon the same criterion that was used in the Al-Ti-(Si) study, the classification of the aluminides phases in active and inactive indicates that only a fraction (~8% for the 0.2 wt.% B alloy and ~10% for the 1 wt.% B alloy) of the total amount of intermetallics present catalyses the Al nucleation. For the sake of comparison, the presence of Si was analyzed using EDS on all the available samples. It was found that no segregation of Si developed to active droplets, as observed for the Al-6 wt.% Ti samples, but rather the Si was uniformly scattered throughout the droplets. This result implies that Si does not appear to play a preferential role in Al catalysis when B is present. Additionally no morphological contrast (i.e. faceted or irregular shapes) between active and inactive intermetallics was observable. The difficulties to detect small amounts of B with standard EDS detectors limited the ability to reveal any B content difference between potent and less catalytic nucleants as identified by the initial Al phase microstructure. Complementary qualitative analysis using highly contrasted Backscattered Electron Image suggests the possible presence of Boron in the interdendritic regions adjacent to the catalyzed Al-phase. This result suggests a constitutional effect of Boron in the remaining liquid alloy so as to reduce the α -Al growth velocity in a similar fashion as Si does in Al-Ti commercial alloys.

In order to supplement the EDS measurements and to provide information on the possible solubility of B in the Al_3Ti phase, two-phase Al + Al_3Ti alloys were prepared with increasing amounts of B. The measured lattice parameters at the limit of the Al + Al_3Ti two phase field were essentially identical to those of pure Al and Al_3Ti without B. As a result it is clear that the beneficial effect of B on grain refinement is not due to an influence on the lattice misfit between Al and Al_3Ti [94].

As a summary, while the main effect of Boron still remains unclear, several alternatives have been studied and crucial data has been obtained to help understand the grain refining mechanisms involved during Al inoculation. While the apparent substrate is still the Al_3Ti phase, B additions appear to impede any solubility of Si into the intermetallic lattice. On the other hand, B itself is not soluble in that phase either. Both active and inactive aluminides present the same morphological aspect.

The successful application of the DET to study the influence of incorporated particles on nucleation catalysis and solidification microstructure development that has been demonstrated in the present work, has been extended to establish a new capability to examine a variety of dispersed particle types in Al base matrices such of those of interest in metal matrix composites.

By means of a modification of the emulsification technique, the incorporation of several types of ceramic particles into pure Al droplets was performed accordingly with the procedure discussed in Section IV. C. 1. SEM observations of these emulsified composites indicate adequate wettability between the metallic droplet and the ceramics. An excellent example of this achievement is shown in Figure 22, where a SiC reinforcing particle is embedded well within a pure Al droplet. The photomicrograph was taken by using a mixed backscattered and secondary electron image and reveals a sharp contrast between the particle and the matrix. Similar results have been obtained for the incorporation of Al_2O_3 particles in Al. The successful incorporation of different dispersed particles in pure Al has also been monitored by thermal analysis to quantify the influence of particles on undercooling behavior. As noted in Figure 23 a, irregularly shaped $\gamma\text{-Al}_2\text{O}_3$ (1 μm) in Al yields a large ΔT ($\sim 110^\circ\text{C}$), but less than that for pure Al. The nucleation exotherm is relatively broad with evidence of a high temperature shoulder indicating the operation of several nucleation sites. In addition, the exotherm peak temperature is sensitive to cooling (Figure 23 a, b) with a shift from $\sim 647^\circ\text{C}$ to 592°C in the cooling rates from $-3^\circ\text{C}/\text{min}$ to $-30^\circ\text{C}/\text{min}$. While the Al_2O_3 -Al composite is not chemically reactive, SiC-Al composite have been reported to react to form an Al_4C_3 product on SiC [59, 95, 96]. The initial thermal analysis results shown in Figures 24 a, b indicate that for the reactive Al-SiC composite droplets the onset of freezing during cooling occurs above the onset of melting during heating as would be expected for reaction product formation. With continued melting and solidification thermal cycles, additional thermal signals due to a likely eutectic reaction develop as would be expected to occur with the formation of an Al_4C_3 reaction product.

Therefore, the application of thermal analysis to composite Al droplets provides additional capability to monitor reactive particle/liquid systems.

The initial effort on composite Al droplets is continuing, but the current capability provides the essential experimental background to pursue a systematic investigation of particle/melt interaction and solidification microstructure evolution in Al alloy metal matrix composite systems.

II. D Metastable phase diagrams

With droplet samples it has been demonstrated in a variety of alloys displaying the full range of phase reaction types that an accurate measurement of metastable phase equilibria is possible. This data has proven to be extremely useful in several ways such as in the proper interpretation of solidification pathways [9] and in the complete modeling of both the stable and metastable phase equilibria [97, 98]. Instead of repeating developments which are well documented in the published literature, some new examples will be used to illustrate the unique value of this approach in analysis of solidification structure evolution.

1. Supersaturation in Sn-Sb alloys

As an initial illustration it is of value to examine the development of supersaturated Sn-rich solid solutions in Sn-Sb alloys during solidification at maximum undercooling. As shown in the phase diagram of Figure 25 the Sn-Sb system displays a peritectic reaction (actually two peritectics) for Sn-rich alloys. In droplet samples, large undercooling, $\Delta T = T_L - T_n$, in excess of 100°C is observed (Figure 26) and yields a metastable solidification product which decomposes upon heating at T_d before the onset of the peritectic melting. A detailed and careful X-ray diffraction study of droplet samples quenched from T_n and examined at subambient temperatures to minimize decomposition effects has confirmed that the initial solidification structure formed at a high undercooling was a supersaturated Sn solid solution for alloys up to 22 at.% Sb. This is indicated by the lattice parameter trend in Figure 27 and the droplet microstructures from interior sections that are given in Figures 28 A, B.

Upon a first inspection the observed behavior for Sn-Sb alloys is similar to that observed in many other alloys where a metastable extension of primary phase solid solubility develops following rapid solidification at high undercooling. In all of these cases the modification of powder microstructure and the operative solidification pathway at high undercooling can be analyzed from a consideration of the stable and/or metastable phase boundaries. For supersaturated β -Sn solid solutions, the relevant phase boundaries are the metastable liquidus and solidus as well as the β /Liquid T_0 curve, which represents the maximum temperature for which partitionless solidification of β is possible.

An extension of the liquidus, solidus and the T_0 curve for $\beta + L$ equilibria obtained from thermodynamic solution model calculations is plotted on the phase diagram in Figure 29. It is significant that the metastable phase boundaries converge to a congruent point at about 15 at.% Sb. In order to obtain high levels of supersaturation it is necessary to attain nucleation temperatures below $T_0^{\beta/L}$. However, for Sb contents in excess of that corresponding to the

congruent point, $\frac{dT_L}{dX_{Sb}} > 0 > \frac{dT_0^{\beta/L}}{dX_{Sb}}$ so that the undercooling required to initiate partitionless solidification increases dramatically. Indeed, the observation that β solubility can not be extended beyond about 22 at.% Sb is consistent with the interpretation of the metastable phase equilibria and explains the results of other studies. Moreover, as a result of the detailed analysis of the Sr-Sb data an important constraint on the extension of solubility due to a metastable congruent point has been identified and may be a general feature in a number of peritectic systems.

2. Microstructural Transitions in Fe-Ni alloys

As a further test of the application of droplet samples together with an analysis based on metastable phase diagrams and competitive kinetics, the microstructural development has been examined after solidification in undercooled Fe-Ni alloys. Even though the Fe-Ni system has been studied previously the solidification behavior has been reported in different studies to follow various pathways, with apparent dissimilarities existing as a function of sample size and processing conditions. In order to identify the possible hierarchy of microstructural pathways and transitions, a systematic evaluation of the microstructural evolution in undercooled Fe-Ni alloys was performed on uniformly processed samples covering seven orders of magnitude in volume. At appropriate undercooling levels, alternate solidification pathways become thermodynamically possible and metastable product structures can result from the operation of competitive solidification kinetics. For thermal history evaluation, a heat flow analysis was applied and tested with large Fe-Ni alloy particles (1 to 3 μm), to assess undercooling potential. Alloy powders (10 to 150 μm), with large liquid undercoolings, were studied under the same composition and processing conditions to evaluate the solidification kinetics and microstructural evolution, including face-centered cubic (fcc)/body-centered cubic (bcc) phase selection and the thermal stability of a retained metastable bcc phase.

For the high melting temperature Fe-Ni alloys it was advantageous to employ a drop tube facility sketched in Figure 30 to promote undercooling by containerless processing and also to

provide a means to enhance the cooling of droplet samples following solidification. For the large drops (1 to 3 mm) and assuming Newtonian heat transfer conditions i. e. Biot number is less than 10^{-2} [99], and applying the Ranz-Marshall relation for a flow past a submerged sphere [100], a numerical analysis of the heat flow yielded undercoolings of $\sim 160^{\circ}\text{C}$ below the liquidus temperature of the fcc phase. The numerical analysis results for the alloy compositions processed in a He-2% H_2 atmosphere are plotted in the upper portion of the Fe-Ni phase diagram of Figure 31. From this model it is apparent that metastable bcc phase formation from the melt is thermodynamically feasible and may compete with fcc phase development.

The X-ray diffraction evidence suggests that the crystal structure of the Fe-Ni alloys was fcc at some point during processing and subsequently transformed to martensite during processing. In the case of the powders (10 to 150 μm), the X-ray diffraction results suggest that martensite exists in a percentage of the large powders (75 to 100 μm) while a non-martensitic bcc phase prevails in the fine powders (30 to 44 μm). The SEM and optical microscopy observations show the presence of a mainly bcc cellular/dendritic morphology in the fine powders and evidence of a martensitic transformation in the large droplets. A quantitative measurement of the volume fraction of the metastable bcc phase as a function of the droplet diameter for Fe-15 wt.% Ni powder processed in He and He-2% H_2 atmospheres is shown in Figure 32. A further kinetics analysis of the data in Figure 32 reveals a similar reaction mechanism (i.e. surface nucleation) but a difference in catalytic site density that may be due to the reducing effect of the He-2% H_2 atmosphere. This supports the important role that processing environment can have on product phase selection.

Based upon the detailed microstructural observations there are two possible solidification pathways. As schematically shown in Figure 33 either bcc or fcc phases could develop upon freezing, depending on the nucleation and growth competition. Moreover, if bcc solidification occurred, the bcc phase could decompose into the fcc phase and then to martensite upon cooling. During the period of recalescence and heat extraction there is sufficient time available for solid-state transformations as demonstrated by solid-state upquenching treatments. For fast cooling rates and/or sluggish decomposition kinetics the high temperature bcc phase could be retained to room temperature. It is well-known that the transition M_s temperature is relatively independent of the cooling rate [101] and that martensitic phase always develops from the fcc phase. Therefore only the bcc δ and martensite phases are possible provided that M_s is above room temperature. On the other hand the presence of an equiaxed grain structure can be explained as the result of a metastable bcc dendritic structure formed from the melt which then transformed into the stable fcc with an equiaxed grain structure before forming martensite. This process is

illustrated in Figure 34.

In fact, the latter pathway has been confirmed by the results of upquenching treatments that are summarized in Figure 35. Essentially, the fine powders cool fast enough in the solid state to retain the metastable bcc phase solidification structure, but the large drops which cool slowly undergo a solid state reaction from the as-solidified bcc phase to an fcc phase which then transforms to martensite. Based upon this analysis a consistent, clear trend is apparent for the first time in the solidification microstructure development for Fe-Ni alloys. When the liquid undercooling falls below the metastable bcc liquidus, the bcc phase develops from the melt.

A summary of the results and analysis of solidification microstructure development in Fe-Ni alloys is presented in Figure 36. The log of droplet diameter vs nickel content is used as a guide to delineate regimes of microstructural development. With decreasing droplet size, larger cooling rates and undercooling apply and, combined with nucleant isolation in the solid state, can account for the change in phase retention below a certain size. The transition size was taken as the approximate droplet diameter where an equal abundance of the two different morphologies (cellular/dendritic vs martensitic) was found so that the trend in Figure 36 may approximate isokinetic-type behavior. Above this transition, the bcc phase formed from the melt, decomposed to the stable fcc phase, and then transformed to martensite (α'). Indeed, the transition size provides a useful means of defining and distinguishing between bulk and powder processing behavior in the Fe-Ni system. In effect, the summary plot given in Figure 36 represents a map which provides in outline form the domains of microstructure development in terms of processing (i.e. sample size) and sample variables (i.e. alloy composition) that can be controlled in a regulated manner. A more complete analysis requires a detailed consideration of the competitive reaction kinetics under the influence of a changing thermodynamic driving free energy. However, if the boundary separating bcc phase retention and decomposition in Figure 36, is regarded as isokinetic in nature and rate-limited by the solid-state heterogeneous nucleation of an fcc phase from the bcc solidification product, then for a given sample composition during continuous cooling at a constant rate T ,

$$-\frac{a}{T} \int_{T_0}^{T_N} J_a(T) dT = 1 \quad [A1]$$

where a is the heterogeneous nucleation site (i.e. sample surface) area, $J_a(T)$ is the steady-state heterogeneous nucleation rate, and T_N is the nucleation temperature. Since $J_a(T)$ is a relatively steep function of T with most of the value occurring near T_N , Eq. [A1] may be approximately expressed by

$$J_a a \frac{\Delta T}{T} \cong 1 \quad [A2]$$

where $\Delta T = T_0^{\delta L} - T_N^{\gamma}$. If it is considered also that along the retention/decomposition boundary J_a is constant, then for powders where $a \propto d^2$ and $T \propto d^{-2}$ [99],

$$d^4 \Delta T \cong \text{constant} \quad [A3]$$

Since ΔT for the solid-state bcc \rightarrow fcc reaction can be expected to scale with alloy composition (over a narrow composition range) the trend in the experimental data of Figure 36 is plausible and in fact agrees with the power-law dependence given by equation [A3].

II. E Droplet Nucleation Kinetics

As a liquid is cooled further into the deeply undercooled regime an increasing variety of structural options develop with either crystallization or vitrification. While there have been a number of kinetics calculations [102] presented to account for the observed structures developed in a given system or for the estimated critical cooling rate for glass formation, such calculations have not been as successful in providing detailed predictions of kinetic behavior that can be tested by experiment. This difficulty appears to be due in part to the sensitivities of such calculations to system specific input data which is usually not available for most systems but has been estimated by various approximation models. These points may be demonstrated clearly by examining the competition between glass formation and crystallization in a near eutectic Au-Pb-Sb alloy.

Based on classical theory the heterogeneous nucleation rate J_a can be represented as [105]

$$J_a = \frac{\Omega_a}{\eta} \exp(-\Delta G^* / kT) \quad (1)$$

Appropriate values for the prefactor Ω_a and nucleation barrier ΔG^* can be derived for different conditions. The liquid viscosity η is given by $\eta(T) = 10^{-3.3} \exp[3.34 T_E / (T - T_{go})]$ with T_E as the eutectic temperature and T_{go} the ideal glass temperature. The activation barrier ΔG^* is given in general by $\Delta G^* = b \sigma_{XL} f(\theta) / \Delta G_v^2$ where σ_{XL} is the crystal/liquid interfacial energy, $f(\theta)$ is a function of the contact angle θ involved in heterogeneous nucleation, ΔG_v is the driving free energy for nucleation per unit volume of product phase and b , is a geometrical factor. During continuous cooling at low rate, the onset of nucleation within a time t and for a droplet with

catalytic surface area a and heterogeneous nucleation rate J_a pure unit area is given to a good approximation as [75]

$$\ln t = -\ln[a\Omega_a / [K(T_N)\eta]] + b\sigma_{cl}^3 f(\theta) / (\Delta G_v^* kT) \quad (2)$$

where K represents a constant at the nucleation temperature. From measurements of ΔT at different cooling rates, T to give t as $\Delta T/T$, the prefactor term $A = a\Omega_a / [K(T_N)\eta]$ and the interfacial energy related term $B = b\sigma_{cl}^3 f(\theta)/k$ may be derived from experimental results if separate values for the driving free energy are available. The kinetics can be accurately determined by differential scanning calorimetry if there is a well defined crystallization onset at large supercooling as is the case in the Au-Pb-Sb system.

With droplet samples that exhibited a maximum undercooling level of $0.3 T_L$ before the onset of heterogeneous nucleation, a wide range of liquid specific heat measurement was accessible as illustrated in Figure 37 where separate values determined for the crystalline state are also displayed [71]. Based on the measured data and standard thermodynamic analysis, the entropy and enthalpy of liquid and crystal could be assessed and used to evaluate the ideal glass temperature (where $\Delta S = S_L - S_x = 0$) as 313K and the free energy difference between liquid and crystal. From the continuous cooling kinetic studies, the measured parameters for the prefactor $A=1.8 \times 10^{16} \text{ s}^{-1}$ and the interfacial energy related slope $B=1.02 \times 10^8 \text{ KJ}^2 \text{ cm}^{-6}$ which yields a value for ΔG^* of about 41 kT.

The specific heat measurements of undercooled liquid in glass forming Au-Pb-Sb alloys cover much wider temperature range and previously reported for several pure metals and alloys [103]. In fact, at the deepest undercooling the liquid heat capacity is almost twice that of the solid. This has an important effect on the actual value of the driving free energy available for crystallization. As noted previously, there have been various approximations to quantities such as the driving free energy ranging from a simple linear treatment with undercooling to a more complex fitting relations [10, 104, 105]. At low undercooling the differences between the various models and the actual experimental measurements are too small to discriminate between the different models as presented in Figure 38, but at high undercooling it is clear that none of the models accurately follows the experimental measurements for Au-Pb-Sb alloys [103].

When the measured crystallization kinetics are compared with the calculated values based upon the measured kinetic parameters and driving free energy and corrected for the temperature dependence of the viscosity, the resulting kinetic curves can be compared as in Figure 39. In this case it is clear that the apparently small differences in predicted values for ΔG_v at the largest

undercooling yield much more significant differences in predicted kinetic behavior [71]. Indeed, none of the free energy approximation models produces a satisfactory fit to the observed crystallization behavior which in turn is confirmed with the fact that the critical cooling rate determined for glass formation is of the order of 10^3°C/s . When transient effects [106] which may be expected to become important as the glass transition is approached are included, there is a minor adjustment of the kinetic curves in Fig. 39, but the critical cooling rate is not affected significantly.

Based on this example it is clear that a reasonable assessment of the competition between glass formation and crystallization over a wide range of undercooling and cooling rate is possible if experimental kinetic and thermodynamic data for the undercooled state are available. This reveals the importance of using measured values of thermophysical properties as a basis for extrapolations into the glass forming regime, in contrast to model approximations that are often inconsistent and only valid at very low undercooling.

II.F. Controlled Alloy Phase Nucleation Catalysis

As the previous discussion on kinetic competition in Au-Pb-Sb alloys has illustrated, the main nucleation process responsible for the onset of crystallization even at the deepest undercoolings that are accessible experimentally is usually catalyzed at a heterogeneous nucleation site. With this in mind, a key issue in developing a more quantitative analysis of the kinetic competition that controls phase and microstructure selection is the identification of the active nucleation site. Once again, due to the flexibility of the droplet technique, it has been possible to introduce known heterogeneous sites to permit a controlled nucleation catalysis evaluation.

The approach for the evaluation of alloy phase catalysis is summarized in Figure 40. The first cycle in Figure 40 indicates that the sample exhibits an undercooling ΔT_{max} when it is cooled from a temperature above the liquidus. By annealing droplet samples between the peritectic temperature, T_p , and the liquidus, a two phase mixture is generated consisting of solid β phase and liquid within each droplet. When the sample is cooled from the annealing temperature as in the second cycle in Figure 40, a level of undercooling of ΔT_{het} below T_p is observed which can be used as a measure of the catalytic potency of β for nucleation of α from the remaining liquid. With this experimental design, the liquid and β coexist in a metastable equilibrium during the slow cooling to T_{het} . However, since the volume fraction of β phase is increasing with decreasing temperature, the heterogeneous catalysis reaction observed is likely to depend upon the atomistic configuration of the β -liquid interface and the interface movement.

In fact, most often the interaction at liquid-solid interfaces during wetting or nucleation reactions is considered in terms of a static interface, but this viewpoint can be misleading as a generalization as shown by the illustration in Figure 41. In addition for the case of solid particles dispersed within a liquid that is typical for composite processing the viewpoint of a dynamic interface character may be most appropriate. During either continuous cooling or isothermal holding the operation of diffusion in the interface region can alter the morphology of particles yielding motion of a particle-liquid interface on an atomic scale which of course is the important size scale for nucleation processes.

When the above approach is applied to a real system, some interesting details of the catalysis behavior are revealed as illustrated in the thermal analysis traces in Figure 42. The results shown were obtained on a Sn-16 at.% Sb alloy droplet sample where the solid catalyst was a Sn_3Sb_2 phase with a cubic rock salt structure. During cycle 1, a broad freezing exotherm was detected ranging from about 210°C to 185°C. Based upon experience, this broad exotherm represents the summation of signals from several nucleation sites of slightly different potency. With continued thermal cycling to 10 repetitions, the initially broad exotherm becomes more sharply defined with a peak temperature that decreases. In addition, as the initial onset at about 210°C is removed at cycle 5, a new exotherm at about 182°C develops and grows in magnitude with continued cycling. Supplementary microstructural studies have also established that with cycling the Sn_3Sb_2 phase changes morphology from irregular crystals in cycle 1 to well developed faceted crystals in cycle 10.

From these observations and other extensive studies including detailed nucleation kinetics measurements, a model has been developed to describe the general atomistic features of the catalysis reactions. The model is based on the realization that in order for a site at a liquid-solid interface to be active in crystal nucleation, the topographic feature must be of a size comparable to a radius of a spherical cap nucleus, i.e. several nm. From this basis a geometric model of the heterogeneous nucleation sites has been proposed as shown in Figure 41. Three principal features are illustrated in order of decreasing catalytic potency: static steps (A), growth steps (B) and facet planes (C). Initially the catalytic solid surface contains many large (almost macroscopic) static steps which permit edge nucleation as illustrated for the shaded wedge shaped nucleus A in Figure 41. With thermal cycling and interface movement to yield the required changes in phase fractions, the large static steps are removed as the surface equilibrates towards a faceted configuration. However, growth steps of atomic dimensions are present during the removal of static steps and allow for a fine scale adjustment of interface configurations. The nucleation potency of a growth step is a function of the step velocity as documented by kinetic

analysis. Along with the progressive removal of static steps, large areas of facet planes which are atomically smooth and remote from any moving growth step develop and provide for a low potency for catalysis. From this geometric model and other supporting evidence it is possible that the exotherms at 210°C, 190°C and 182°C represent catalysis by static steps, growth steps and facet planes respectively.

The results of this study have allowed for a quantitative assessment of the undercooling of liquid alloys, the stability of solidification structures, an improved comprehension of the reaction path followed during alloy solidification including the influence of competing metastable phase reactions and contribute to an improved understanding and modeling of microstructure evolution during RSP and other processing such as spray deposition, surface melting and composite fabrication. It is clear that the full potential for the use of nucleation control in solidification processing has not yet been realized.

III. Publications of the current program

During a research program, substantial time intervals often elapse between the completion of a research study, submission of a manuscript, and the final appearance of a paper in print. As a result, the following list gives publications in preparation as well as those in print or in press.

1. "Constitution of the Tin-Antimony System", W.P. Allen and J.H. Perepezko, *Scripta Met.* **24**, 2215, (1990).
2. "Evaluation of Al-Ti-Si Alloys as Grain Refining Agents", M.K. Hoffmeyer and J.H. Perepezko in "Light Metals 91", ed. E.L. Rooy, (TMS, Warrendale, PA) 1105, (1991).
3. "Thermodynamic Properties and Crystallization Kinetics of Undercooled Liquid Au-Pb-Sb Alloys", H.J. Fecht, J.H. Perepezko, M.C. Lee and W.L. Johnson, *Jnl. Appl. Physics*, **68**, 4494, (1990).
4. "Solidification of Undercooled Sn-Sb Peritectic Alloys I: Microstructural Evolution", W.P. Allen and J.H. Perepezko, *Met. Trans.*, **22A**, 753, (1991).
5. "Solidification of Undercooled Sn-Sb Peritectic Alloys II: Heterogeneous Nucleation", W.P. Allen and J.H. Perepezko, *Met. Trans.*, **22A**, 765, (1991).
6. "Solidification Structure Development and Substrate Interactions in Solder Alloys", M.K. Hoffmeyer and J.H. Perepezko in "The Metal Science of Joining" eds. M.J. Cieslak, J.H. Perepezko, S. Kang and M.E. Glicksman (TMS, Warrendale, PA) 73 (1992).
7. "Microstructural Observation of Active Nucleants in Al-Ti-B Master Alloys", O.M. Suarez

- and J.H. Perepezko in "Light Metals 1992" ed. E.R. Cutshall (TMS, Warrendale, PA) 851 (1992).
8. "Microstructural Tansitions During Containerless Processing of Undercooled Fe-Ni Alloys", D.J. Thoma and J.H. Perepezko, *Met. Trans.*, 23A, 1347 (1992).
 9. "Microstructural Development in Undercooled Al-Be Powders", B.A. Mueller, L.E. Tanner and J.H. Perepezko, *Mat. Sci. & Eng.* A150, 123 (1992).
 10. "Thermal Analysis of Solidification Kinetics", J.H. Perepezko in "Thermal Analysis in Metallurgy", eds. R.D. Shull and A. Joshi (TMS, Warrendale PA) 121 (1992).
 11. "Solidification Kinetics and Metastable Structures in Undercooled Melts", J.H. Perepezko in "Metastable Microstructures", eds. D. Banerjee and L.A. Jacobson, Oxford & IBH Pub., Bombay, 3 (1993).
 12. "Fundamentals of Solidification at High Rates", W.J. Boettinger and J.H. Perepezko in "Rapidly Solidifying Alloys", ed. H. Liebermann (Marcel Dekker, NY), 17 (1993).
 13. "Nucleation Kinetics in Undercooled Liquid Metals and Alloys", J.S. Paik and J.H. Perepezko in "Nucleation and Crystallization in Liquids and Glasses", ed. M.C. Weinberg, Amer. Cer. Soc., Westerville, OH, 13 (1993).
 14. J.H. Perepezko *J. Non-Cryst. Solids*, 156-158, 463 (1993)
 15. Interface Reactions and Microstructure Control in Composite Processing", J.H. Perepezko (Composite Interfaces, in press).
 16. "Solidification of a Supersaturated Al_2Y Laves Phase", J.C. Foley, D.J. Thoma and J.H. Perepezko (*Met. Trans.*, in press).
 17. "Formation of Metastable $L_{12} Al_3Y$ Through Rapid Solidification Processing", J.C. Foley, J.H. Perepezko and D. Skinner, (*Mat. Sci. and Eng.*, in press).
 18. "Nucleation Controlled Microstructures in Al-Si Alloys", M. Gremaud and J.H. Perepezko (in preparation).

Patents

"Method of Evaluation and Identification for the design of Effective Inoculation Agents", J.H. Perepezko and M.K. Hoffmeyer, U.S. Patent No. 5,066,324.

IV. Participating Scientific Personnel

1. Professor J.H. Perepezko, Principal Investigator.
2. W.P. Allen, Graduate Student, PhD in Metallurgical Engineering, December 1990.

3. M.K. Hoffmeyer, Graduate Student, PhD in Metallurgical Engineering, December 1990.
4. J.C. Foley, Graduate Student, M.S. in Metallurgical Engineering, May 1991, currently working on PhD.
5. O.M. Suarez, Graduate Student, M.S. in Materials Science and Engineering, May 1993.

V. References

1. B. Chalmers, "Principles of Solidification", Wiley, NY (1964).
2. J.H. Perepezko, "Rapid Solidification Processing: Principles and Technologies II", eds. R. Mehrabian, B.H. Kear, and M. Cohen, p. 56., Claitors Publishing Division, Baton Rouge, LA, (1980).
3. J.H. Perepezko, D.H. Rasmussen, I.E. Anderson and C.R. Loper Jr, "Sheffield Int. Conf. on Solidification and Casting of Metals", p. 169., Metals Soc., London (1979).
4. J.H. Perepezko and J.S. Paik, "Rapidly Solidified Amorphous and Crystalline Alloys", eds., B. Kear, B.C. Giessen, and M. Cohen, p. 49., North Holland, NY, (1982).
5. J.H. Perepezko and I.E. Anderson, "Synthesis and Properties of Metastable Phase", eds. T.J. Rowland and E.S. Machlin, p. 31., The Metallurgical Society of the American Institute of Mining, Metallurgical, and Petroleum Engineers, Warrendale, PA, (1980).
6. J.J. Richmond, J.H. Perepezko, S.E. LeBeau and K.P. Cooper, In Rapid Solidification Processing: Principles and Technologies III, Ed. R. Mehrabian, p. 90 NBS, Washington, DC (1983).
7. K.P. Cooper, I.E. Anderson and J.H. Perepezko, "Proc. 4th Int. Conf. on Rapidly Quenched Metals", Eds. T Masumoto and K. Suzuki, p. 107, Japan Inst. Metals, Sendai (1982).
8. T.Z. Kattamis and M.C. Flemings, Trans. AIME, 236, 1523 (1966).
9. D. Turnbull, *J. Appl Phys.*, 21, 804, 1022 (1950).
10. J.H. Perepezko and J.S. Paik, *J. Non-Cryst. Solids*, 61, 113 (1984).
11. J.H. Perepezko, *Mat. Sci. Eng.*, 65, 125 (1984).
12. C.C. Wang and C.S. Smith, *Trans. AIME*, 188, 136 (1950).
13. E. Meyer and L. Rinderer, *J. Crystal Growth*, 28, 199 (1975).
14. R.E. Cech and D. Turnbull, *Trans. AIME*, 206, 124 (1956).
15. L.L. Lacy, M.B. Robinson and T.J. Rathz, *J. Crystal Growth*, 51, 47 (1980).
16. T.Z. Kattamis and M.C. Flemmings, *Trans. AFS*, 75, 191 (1967).
17. S.Y. Shirashi and R.G. Ward, *Canadian Met. Quarterly*, 3, 117 (1964).
18. J. Paull, J. Ryall and G.W. Delamore, *Scripta Met.*, 10, 845 (1976).
19. J.H. Perepezko, S.E. LeBeau, B.A. Mueller and G.J. Hildeman, "Rapidly Solidified Powde

- Al Alloys", Eds. E.A. Starke and M.E. Fine. Eds., ASTM-STP 890, Philadelphia, PA. 118 (1985).
20. C.G. Levi and R. Mehrabian, *Metall. Trans. A*, 13A, 221 (1982).
 21. H.D. Brody and M.C. Flemings, *Trans. AIME*, 236, 615 (1966).
 22. A. Cibula, *J. Inst. Met.*, 76, 321 (1950), 80, 11 (1951-1952).
 23. F.A. Crossley and L.F. Mondolfo, *Trans. AIME*, 141, 1143 (1951).
 24. I.G. Davies, J.M. Dennis, and A. Hellawell, *Met. Trans.*, 1, 275 (1970).
 25. G.P. Jones and J. Pearson, *Met. Trans.*, 7B, 223 (1976).
 26. J.A. Marcantonio and L.F. Mondolfo, *J. Inst. Met.*, 98, 23 (1970).
 27. I. Maxwell and A. Hellawell, *Acta Met.*, 23, 895 (1975).
 28. J.H. Perepezko, and S.E. LeBeau, "Aluminum Transformation Technology and Its Applications", C.A. Pampillow, H. Biloni, and L.F. Mondolfo, Eds., ASM, Metals Park, OH, 309 (1982).
 29. L. Arnberg, L. Backerud, and H. Klang, *Met. Tech.*, 9, 1 (1982), 9, 7 (1982).
 30. M.M. Guzowski, G.K. Sigworth, and D.A. Sentner, *Met. Trans.*, 18A, 603 (1987).
 31. J. Cisse, G.F. Bolling, and H.W. Kerr, *J. Cryst. Growth*, B-14, 777 (1972).
 32. L.F. Mondolfo, "Grain Refinement in Castings and Welds", G.J. Abbaschian and S.A. David, Eds., TMS, 3 (1983).
 33. D.A. Granger, "Practical Aspects of Grain Refining Aluminum Alloy Melt", Laboratory Report 11-1985-01, Alumin Company of America, (1985).
 34. J.L. Kirby, "Aluminum Alloys-Physical and Mechanical Properties", E.A. Starke and T.H. Sanders, Eds., 1, EMAS, West Midlands, U.K., 61 (1986).
 35. A.J. Cornish, *Met. Sci.*, 9, 477 (1975).
 36. T.W. Cyne and M.H. Robert, *Met. Tech.*, 177 (1980).
 37. D. Turnbull and B. Vonnegut, *Ind. Eng. Chem.*, 44, 1292 (1952).
 38. P.B. Crosley, A.W. Douglas, and L.F. Mondolfo, "The Solidification of Metals", Iron and Steel Inst., 10 (1968).
 39. A. Hellawell, "Solidification and Casting of Metals", The Metals Society, 161 (1979).
 40. W.A. Tiller and T. Takahashi, *Acta Met.*, 17, 483 (1969).
 41. M.K. Hoffmeyer, M.S. Thesis, University of Wisconsin-Madison (1985).
 42. B.E. Sundquist and L.F. Mondolfo, *Trans. AIME*, 221, 607 (1961).
 43. K.A. Jackson and C.E. Miller, *J. Cryst. Growth*, 40, 169 (1977).
 44. D.P. Woodruff, "The Solid-Liquid Interface", Cambridge Univ. Press, London, 25 (1973).
 45. G.V. Samsonov, A.D. Pansasyuk, and G.K. Kozina, *Sov. Powder Met. and Met. Ceram.*, 11, 874 (1968).
 46. S.K. Rhee, *J. Amer. Ceram. Soc.*, 53, [7], 386 (1970).

47. G.A. Yasinskaya, *Poroshkovaya Met.*, 7, [43], 53 (1966).
48. M. Humenik Jr. and W.D. Kingery, *J. Amer. Ceram Soc.*, 37, [1], 18 (1954).
49. Y.U. Naidich and G.A. Koleschenko, *Poroshkovaya Met.*, 2, 76 (1968).
50. Y.U. Naidich and Y.N. Chuvashov, *J. Mat. Sci.*, 18, 2071 (1983).
51. V.K. Nagesh, A.P. Tomisia, and J.A. Pask, *J. Mat. Sci.*, 18, 2173 (1983).
52. J.A. Marcantonio and L.F. Mondolfo, *Met. Trans.*, 2, 465 (1975).
53. A. Cibula, *Foundry Trade Jnl.*, 93, 695 (1952).
54. K.F. Kobayashi, S. Hashimoto, and P. Shingu, *Z. Metallkde.*, 74, 751 (1983).
55. G.P. Jones, "New Ideas on the Mechanism of Heterogeneous Nucleation in Liquid Aluminum", NPL Report DMA(A) 19, Oct. (1980).
56. M.K. Hoffmeyer and J.H. Perepezko, *Scripta Met.*, 22, 1143 (1988).
57. M.K. Hoffmeyer and J.H. Perepezko, *Scripta Met.*, 23, 315 (1989).
58. M.K. Hoffmeyer and J.H. Perepezko, "Light Metals 1989", P.G. Campbell, Ed., TMS, 913 (1988).
59. V. Laurent, D. Chatain and N. Eustathopoulos, *J. Mater. Sci.*, 22, 244 (1987).
60. R.E. Sanders, Jr., G.J. Hildeman, Air Force Wright Aeronautical Laboratories Technical Report, AFWAL-TR-81-4076 (1981).
61. S.L. Langenbeck, R.A. Rainen, et al., Air Force Wright Aeronautical Laboratories Technical Report, AFWAL-TR-86-4027 (May 1986).
62. D.J. Skinner, R.L. Rye, D. Raybould, and A.M. Brown, *Scripta Metal.*, 20, 867, (1986).
63. M.S. Zedalis and M.E. Fine, *Met. Trans. A.*, 17A, 2187, (1986).
64. I.M. Lifshitz and V.V. Slyozov, *J. Phys. Chem. Solids*, 19, 35, (1961).
65. C. Wagner, *Z. Elektrochem*, 65, 581, (1961).
66. L.F. Mondolfo, "Aluminum Alloys: Structure and Properties", The Butterworth Group, Butterworth publishers, Boston Mass. (1976).
67. L.M. Angers, D.G. Konitzer, J.L. Murray and W.G. Truckner, "Dispersion Strengthened Aluminum Alloys", eds. Y-W Kim and W.M. Griffith, TMS-AIME, Warrendale, PA, 355, (1988).
68. L. Angers, Y. Chen, M.E. Fine, J.R. Weertman and M.S. Zedalis, "Proc. of Aluminum Alloys Their Physical and Mechanical Properties", eds. E.A. Starke, Jr. and T.H. Sanders, Jr., Chameleon Press LTD, London, UK, 1, 321, (1986).
69. M.H. Burden and J.D. Hunt, *J. of Crystal Growth*, 22, 328, (1974).
70. J.H. Perepezko and W.J. Boettinger, *Proc. Mat. Res. Soc. Symp.*, 19, 223, (1983).
71. J.H. Perepezko, B.A. Mueller, and K.O. Ohsaka, "Undercooled Alloy Phases", eds. E.W. Collings and C.C. Koch, TMS-AIME, Warrendale, PA, 289 (1987).
72. W.P. Allen and J.H. Perepezko, *Scripta Met.*, 24, 2215, (1990).

73. J. H. Perepezko and W. P. Allen, in "Proc. of the Third International Colloquium on Drops and Bubbles", T. Wang, Ed., Amer. Inst. of Phys., (1989).
74. J.H. Perepezko, J.A. Graves, and B.A. Mueller, in "Processing of Structural Metals by Rapid Solidification", F. H. Froes and S. J. Savage, Eds., ASM, Metals Park, OH, 13 (1987).
75. W.J. Boettinger and J.H. Perepezko, in "Rapidly Solidified Crystalline Alloys", S. K. Das, B. H. Kear, and C. M. Adams, Eds., TMS-AIME, Warrendale, PA, 21 (1985).
76. J. H. Perepezko and W. J. Boettinger, "Surface Alloying by Ion, Electron, and Laser Beams", L.E. Rehn, S.T. Picraux, and H. Wiedersich, Eds., ASM, Metals Park, OH, (1986).
77. J. H. Perepezko and D. U. Furrer, in "Dispersion Strengthened Aluminum Alloys", Y-W. Kim and W.M. Griggith, Eds., TMS, Warrendale, PA, 77 (1988).
78. K. A. Gschneider Jr., F. W. Calerwood, *Bulletin of Alloy Phase Diagrams*, 10, 44, (1989).
79. Akihisa Inoue, Katsumasa Ohtera and Tsuyoshi Masumoto, *Japanese J. of Appl. Phys.*, 27, No. 5, L736, (1988).
80. M.X. Quan, P. Haldar, J. Werth and B.C. Giessen, *Mat. Res. Soc. Symp. Proc.*, 58, 299, (1986).
81. J.C. Foley, J.H. Perepezko, and D.J. Skinner, (in preparation).
82. J. F. Cannon, and H. T. Hall, *Journal of Less-Common Metals*, 40, 313, (1975).
83. Jian-Hua Xu, and A.J. Freeman, *J. Mater. Res.*, 6, 1188, (1991).
84. Private Communication D.J. Skinner Allied Corporation, Morristown NJ.
85. P. I. Kripyakevich, *Soviet Physics of Crystallography*, 5, 440, (1960).
86. F. Laves, "Theory of Alloy Phases", ASM Cleveland, OH, 124, (1956).
87. W.P. Allen and J.H. Perepezko, *Met. Trans.*, 22A, 753, (1991).
88. W.P. Allen and J.H. Perepezko, *Met. Trans.*, 22A, 765, (1991).
89. M. K. Hoffmeyer, Ph.D. Thesis, University of Wisconsin-Madison, (1991).
90. M. K. Hoffmeyer and J. H. Perepezko, in "Light Metals 1991", E. L. Rooy, Ed., TMS, 1105, (1991).
91. O. M. Suárez and J. H. Perepezko, in "Light Metals 1992", E. R. Cutshall, Ed., TMS, 851, (1992).
92. H. W. Kerr, J. Cisse and G. F. Bolling, *Acta Met.*, 22, 677 (1974).
93. H. J. Schurhoff, W. Gruhl and W. G. Burchard, *Z. Metallkde.*, 74, 132 (1983).
94. O. M. Suárez, M. S. Thesis, University of Wisconsin-Madison (to be published).
95. D. J. Lloyd and E. Dewing, in "Advanced Structural Materials", D. S. Wilkinson, Ed., 9, Pergamon Press, NY, 71 (1988).
96. R. Warren and C-H. Anderson, *Composites*, 15 (2), 101 (1984).
97. H.J. Fecht and J.H. Perepezko, *Met. Trans.*, 20A, 785, (1989).

98. H.J. Fecht, M.X. Zang, Y.A. Chang and J.H. Perepezko, *Met. Trans.*, 20A, 795, (1989).
99. C. G. Levi and A. R. Mehrabian, *Metall. Trans. B*, 11B, 21, (1980).
100. R. B. Bird, W. E. Stewart and E. N. Lightfoot, "Transport Phenomena", John Wiley & Sons, New York, NY, (1960).
101. J. D. Verhoeven, "Fundamentals of Physical Metallurgy", John Wiley & Sons, NY, (1975).
102. H. Jones, "Rapid Solidification of Metals and Alloys", Inst. of Metallurgists, London, 1982.
103. H. J. Fecht, J. H. Perepezko, M. C. Lee and W. L. Johnson, *J. Appl. Phys.*, 68, 4494 (1990).
104. K. S. Dubey and P. Ramachandrarao, *Acta Metall.*, 32, 91 (1984).
105. C. V. Thompson and F. Spaepen, *Acta Metall.*, 27, 1855 (1979).
106. J. D. Hoffman, *J. Chem. Phys.*, 29, 1192 (1958).
107. J.P. Nic S. Zhang and D.E. Mikkola, *Scripta Metall. and Mater.*, 24, 1099 (1990).
108. M. Kogachi, S. Minamigawa and K. Nakahigashi, *Scripta Metall. and Mater.*, 27, 407 (1992).
109. K.F. Kelton and A.L. Greer, *J. Non-Cryst. Solids* 79 295 (1986).
110. B. Kujur, A. K. Ray, C. B. Raju and M. Patel, *J. Mater. Sci.*, 22, 962 (1987).
111. N. Blake and M.A. Hopkins, *J. Mat. Sci.*, 20, 2861, (1985).
112. R.R. Sawtell and J.W. Morris, Jr., "Exploratory Alloy Development in the System Al-Sc-X", *Dispersion Strengthened Aluminum Alloys*, Eds. Y-W. Kim and W.M. Griffith (1988) 409-420.
113. D. Eliezer, S.J. Savage, Y.R. Mahajan, and F.H. Froes, *Mat. Res. Soc. Symp. Proc.*, 58, 293, (1986).
114. Akihisa Inoue, Katsumasa Ohtera, An-Pang Tsai and Tsuyoshi Masumoto, *Japenese J. of Appl. Phys.*, 27, L479, (1988).
115. Yeong-Hwan Kim, Akihisa Inoue and Tsuyoshi Masumoto, *Materials Trans. JIM*, 31, 747 (1990).
116. Yeong-Hwan Kim, Akihisa Inoue and Tsuyoshi Masumoto, *Materials Trans. JIM*, 32, 331 (1991).
117. M.F. Ashby, *Acta Met.*, 20, 887, (1972).
118. M.F. Ashby and K.E. Easterling, *Acta Met.*, 30, 1969, (1982).
119. A.S. Helle, K.E. Easterling and M.F. Ashby, *Acta Met.*, 33, 2136, (1985).
120. B. Dill, Y. Li, M. Al-Khafaji, W.M. Rainforth, R.A. Buckley, and H. Jones, to be published in *Materials Science & Engineering*

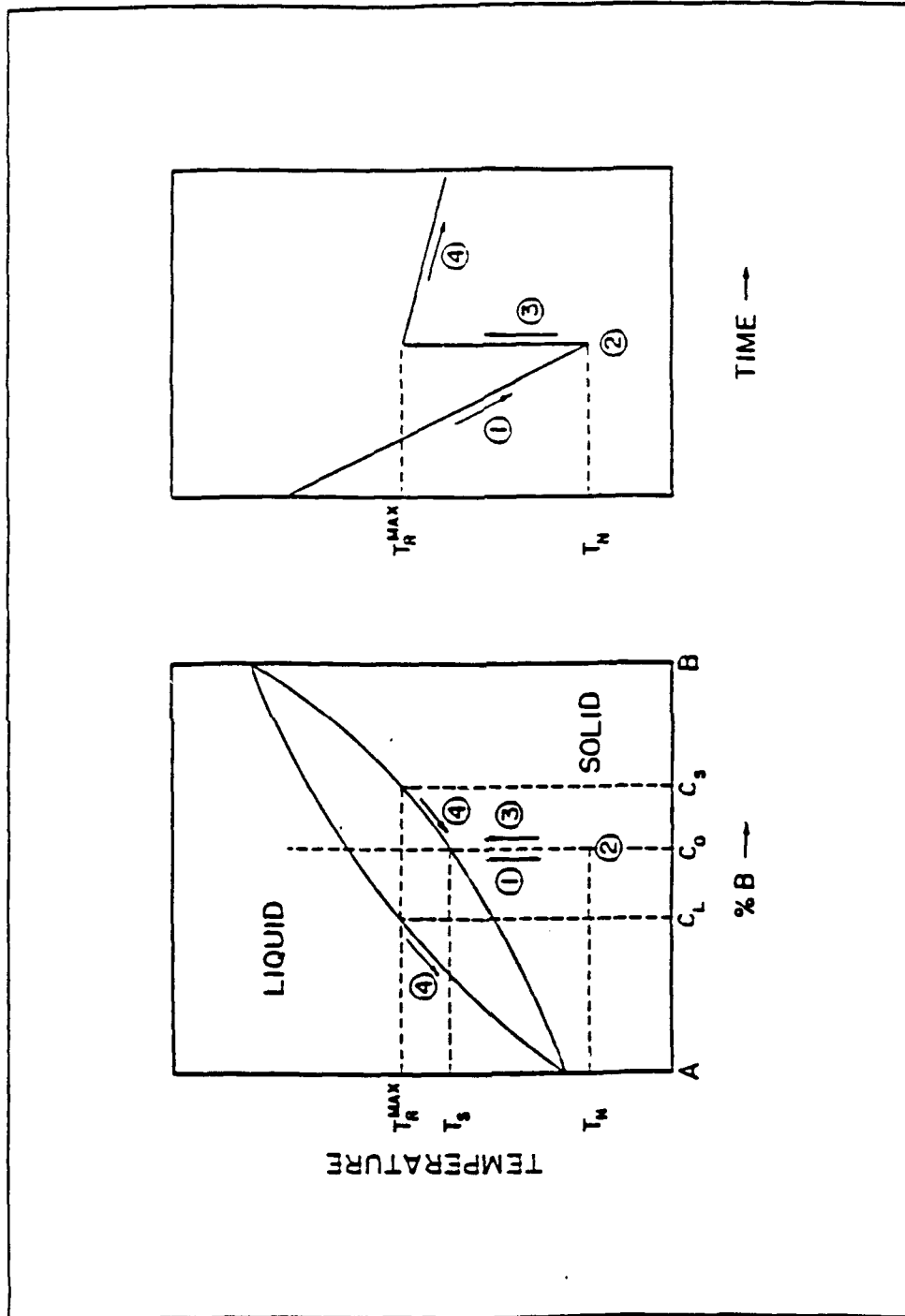


Figure 1

Schematic representation of the recalescence for an isomorphous alloy of composition C_0 .

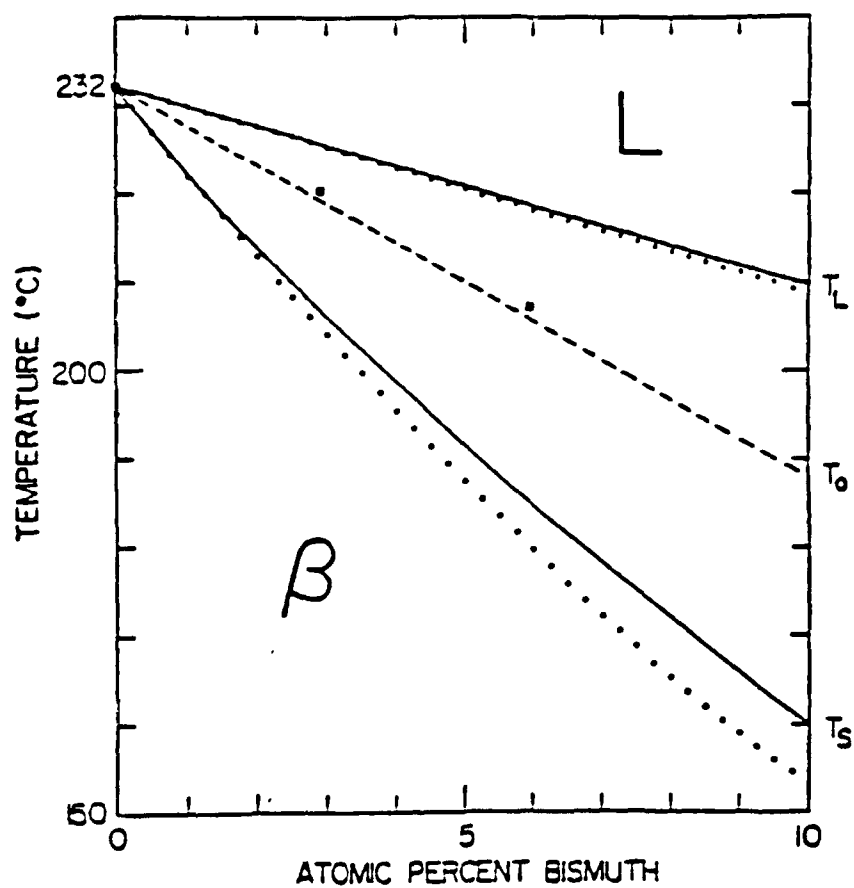


Figure 2

Comparison of the measured values of T_0 with the Si-rich portion of the Sn-Bi phase diagram and the calculated T_0 curve (dashed line).

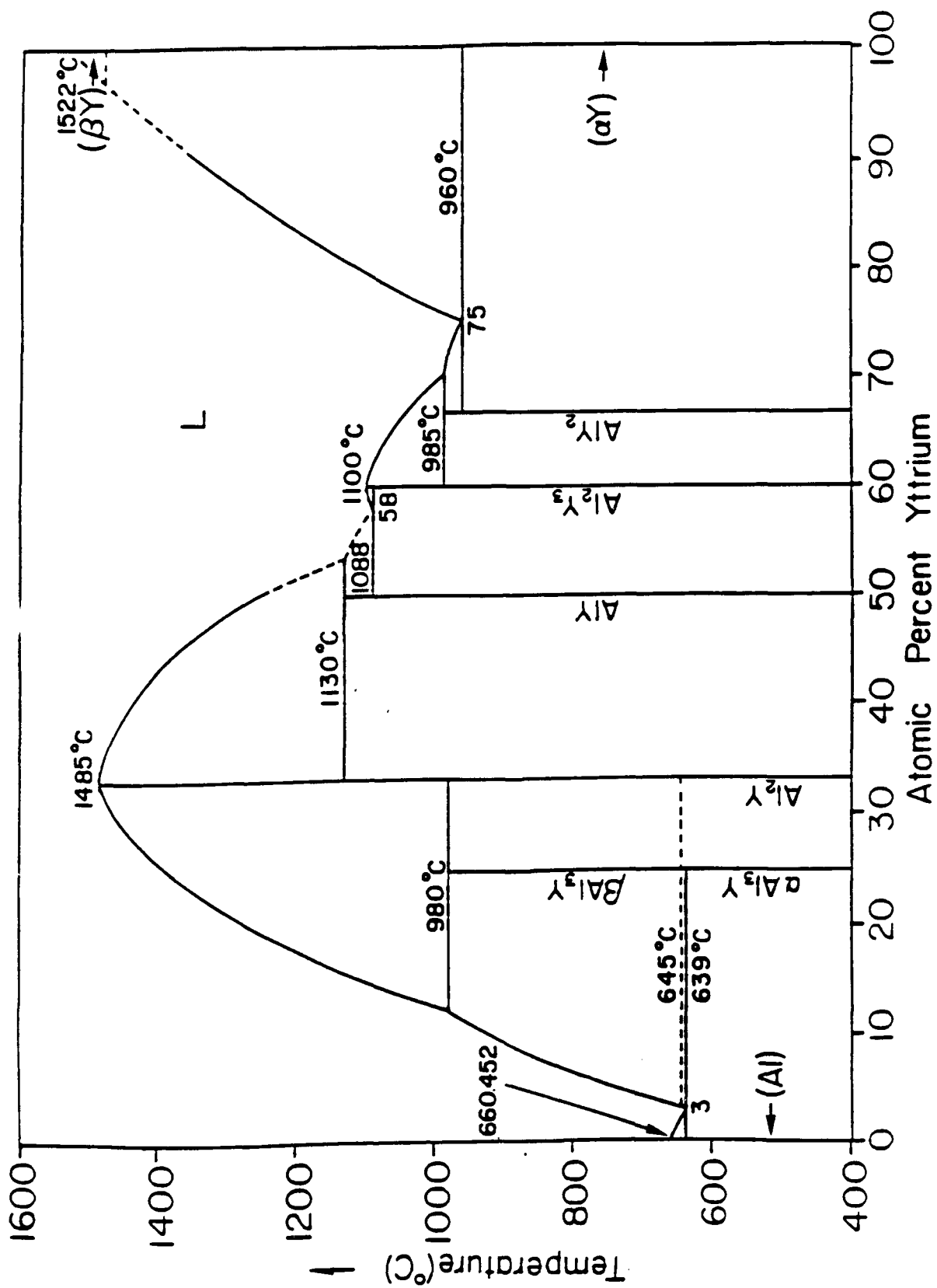


Figure 3

The reported equilibrium binary phase diagram for the Al-Y system.

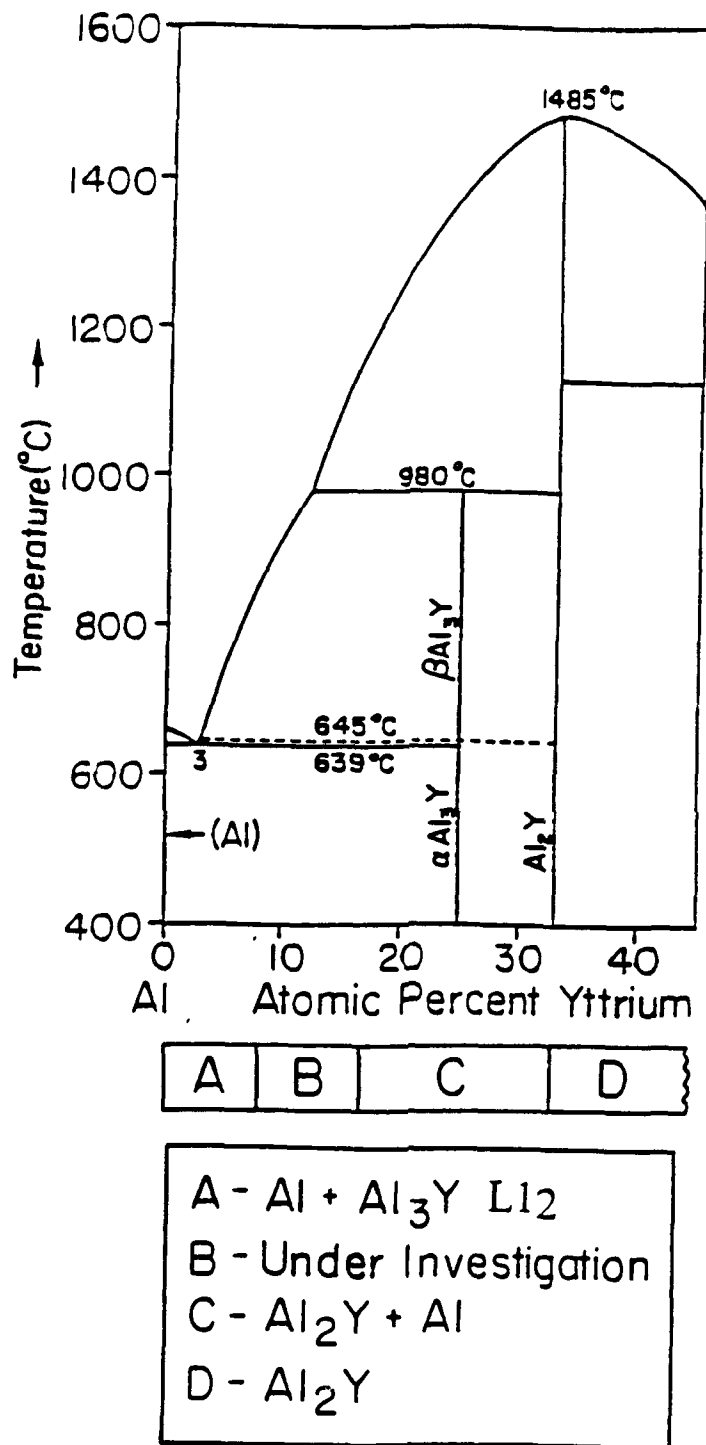


Figure 4

A partial Al-Y binary phase diagram indicating the range of compositions studied and the phases formed by rapid solidification processing.

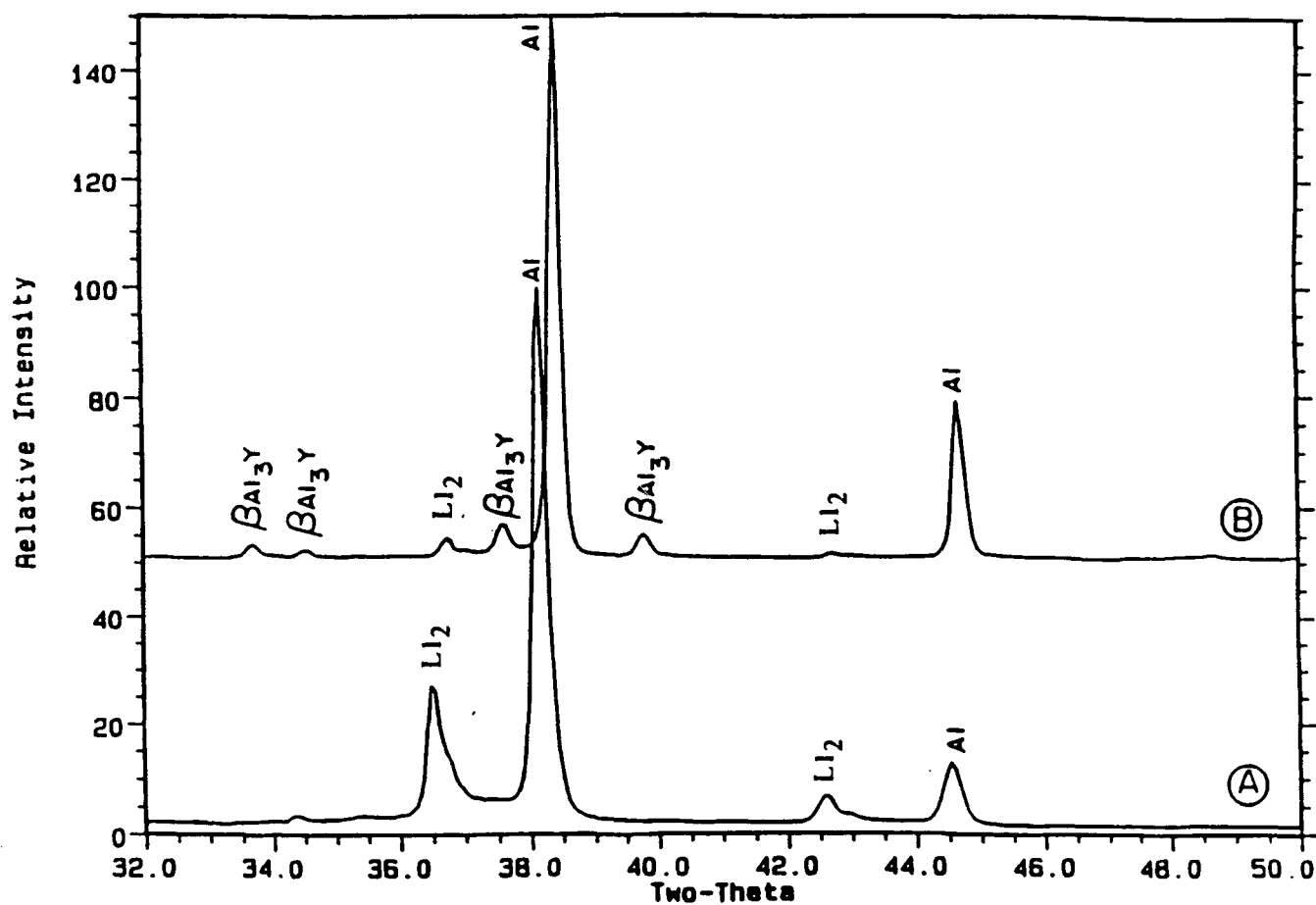


Figure 5

X-ray diffraction traces of the Al-3at%Y sample in the as-solidified condition (trace A) and in the post thermal cycling condition (trace B) showing the presence of L_{12} reflections.

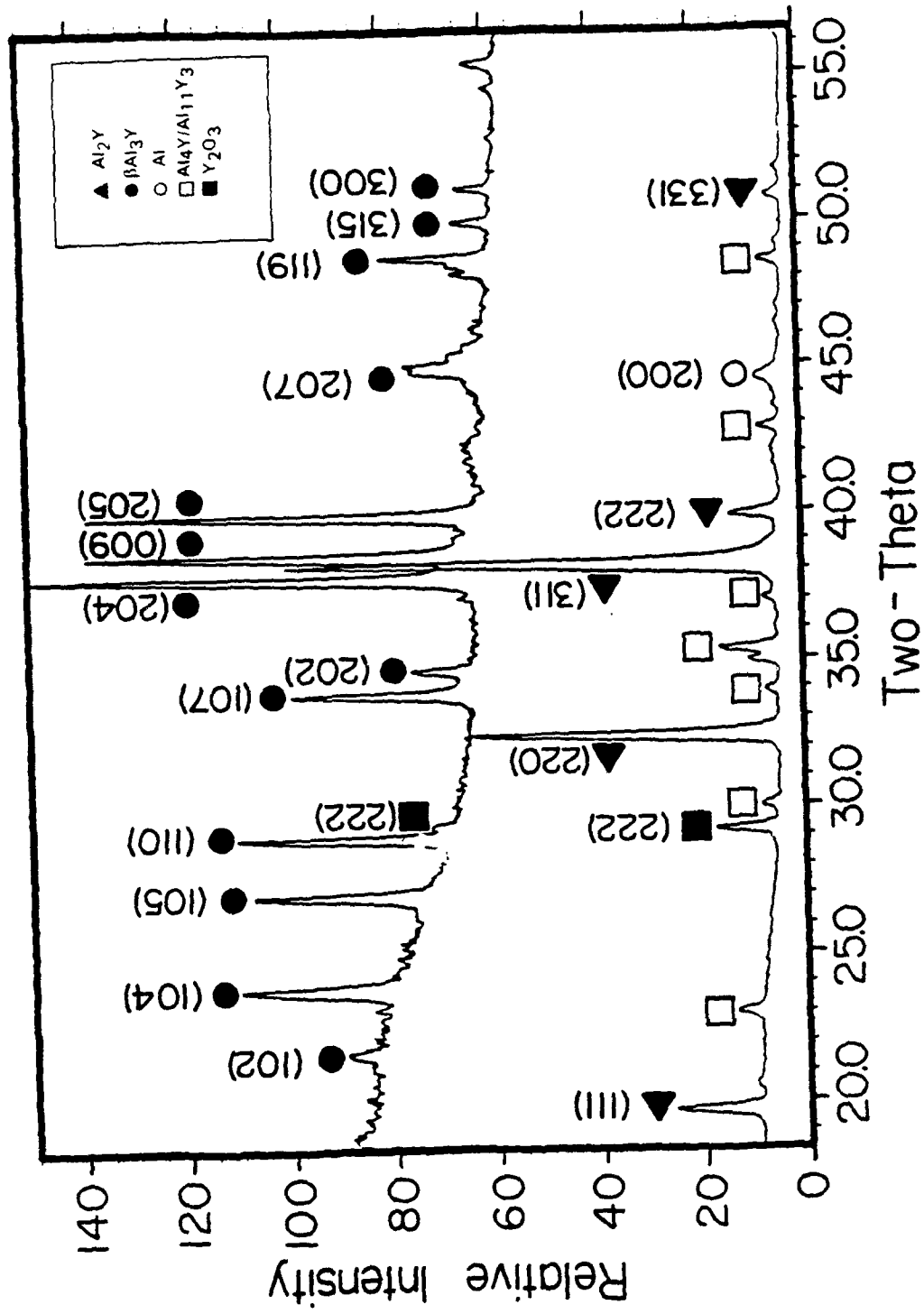


Figure 6

X-ray diffraction traces of the Al-18.1at%Y sample in the as-solidified condition (trace A) and the post DSC condition (trace B)

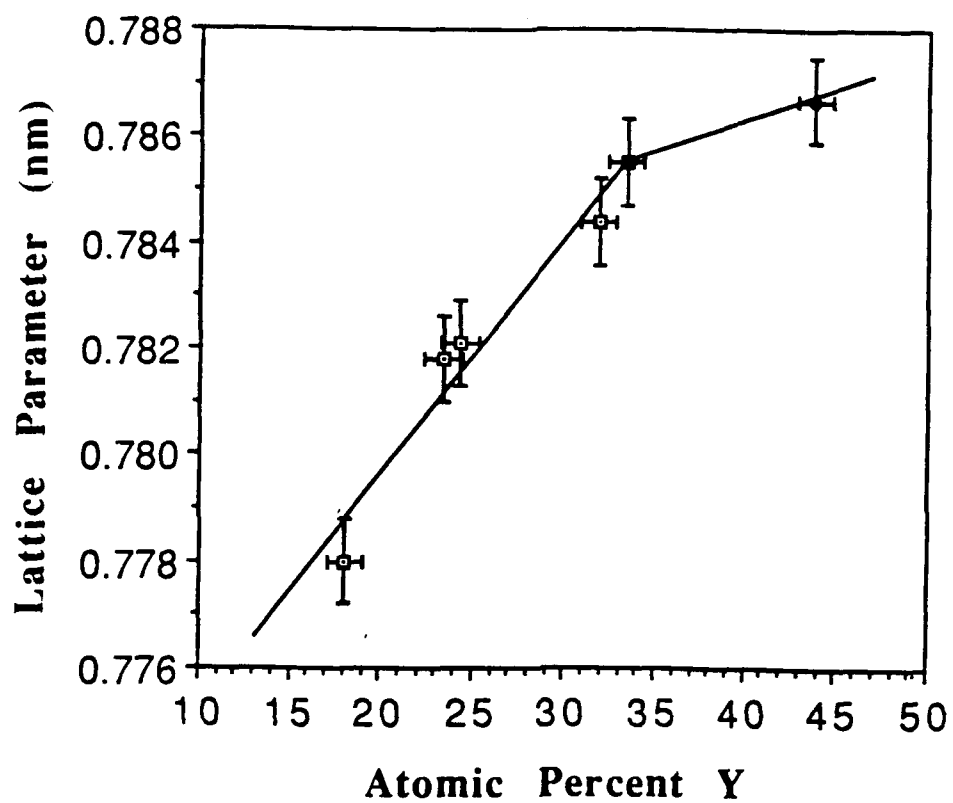


Figure 7

The observed lattice parameters of the supersaturated Al_2Y phase versus the composition determined by EDS analysis.

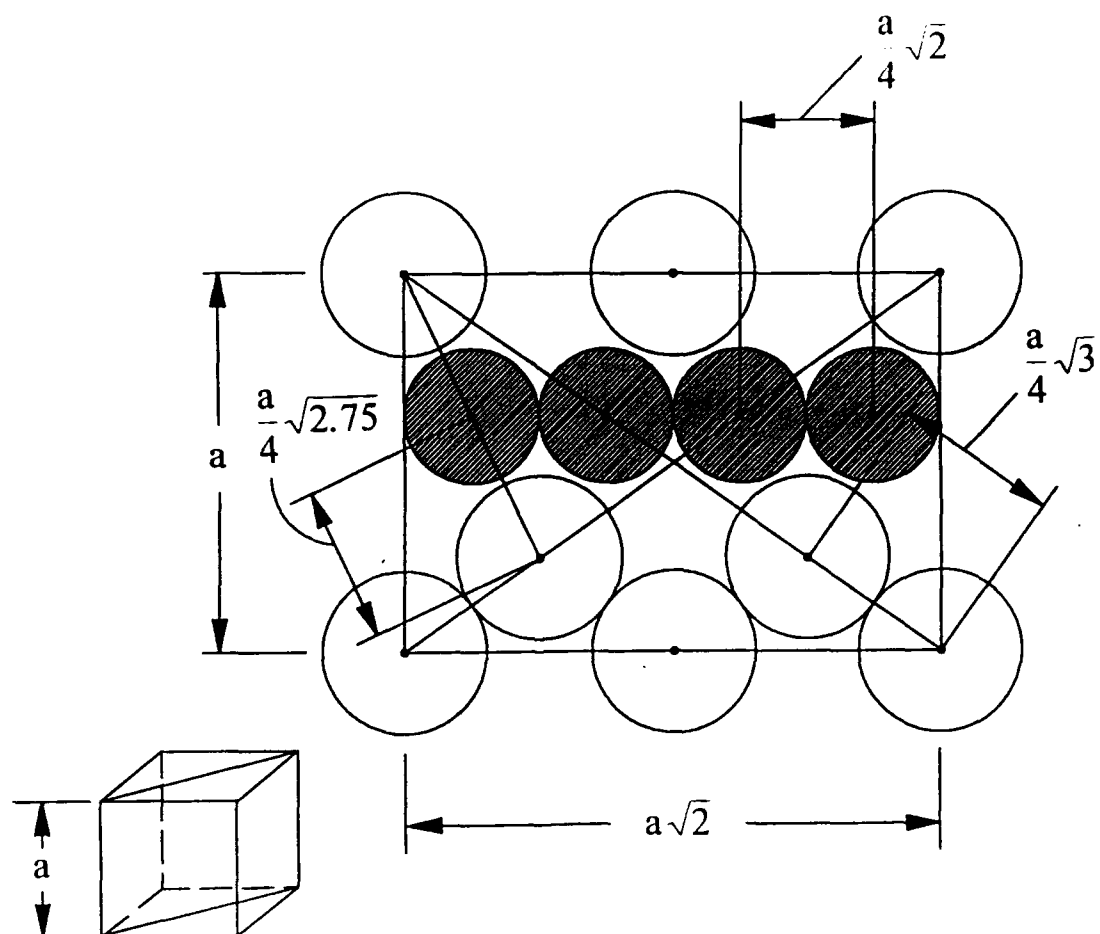


Figure 8

The crystallography of the $\{110\}$ plane along with the geometric relationships of the atoms.

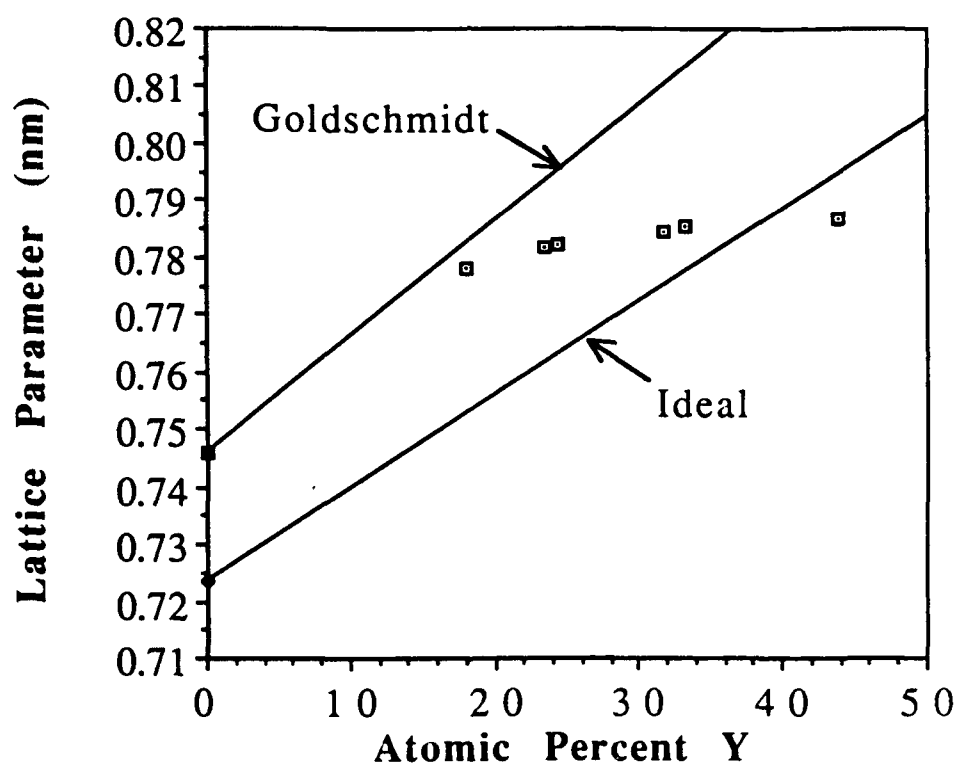


Figure 9

The observed lattice parameters of supersaturated Al₂Y phase versus composition along with the calculated relationships using Goldschmidt radii and ideal radii.

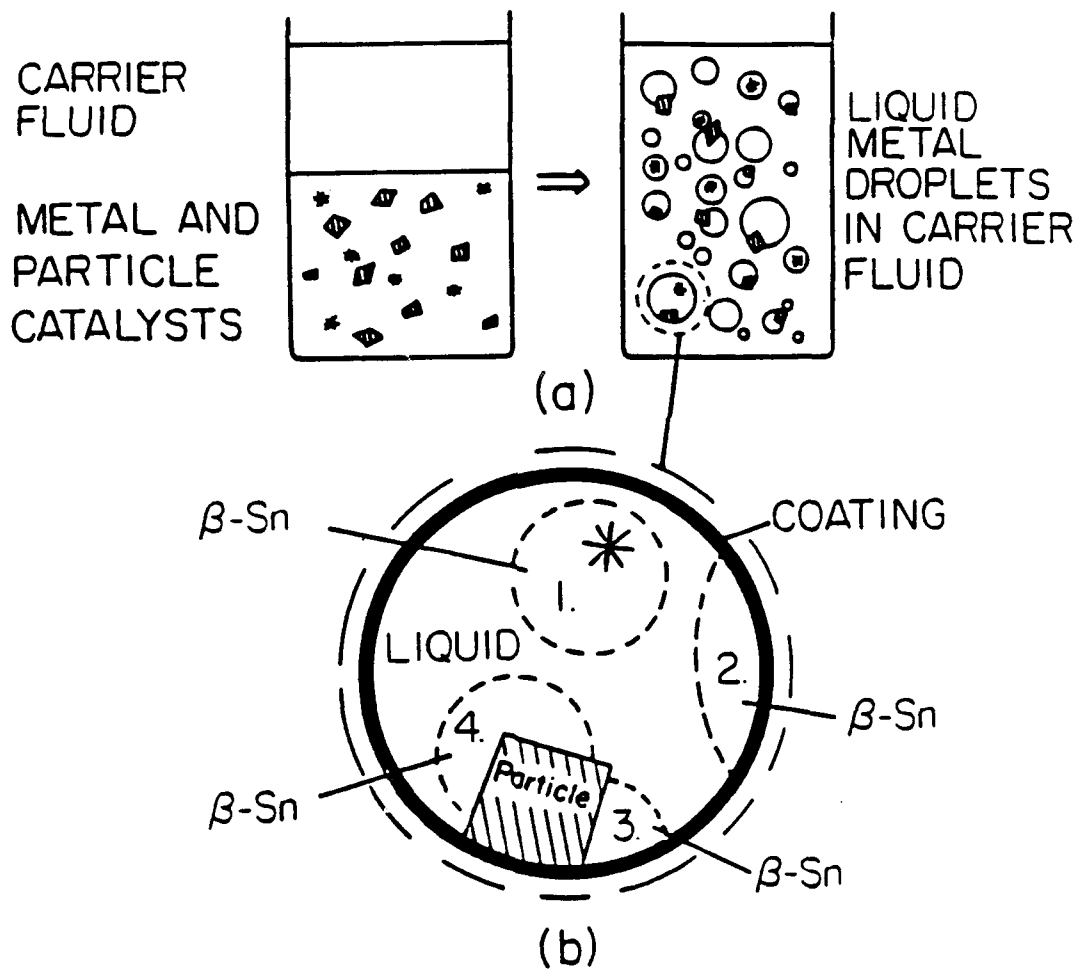


Figure 10

Schematic illustrating (a) nucleant isolation and particle incorporation during droplet emulsification and (b) potential nucleation sites in a particle incorporated droplet.

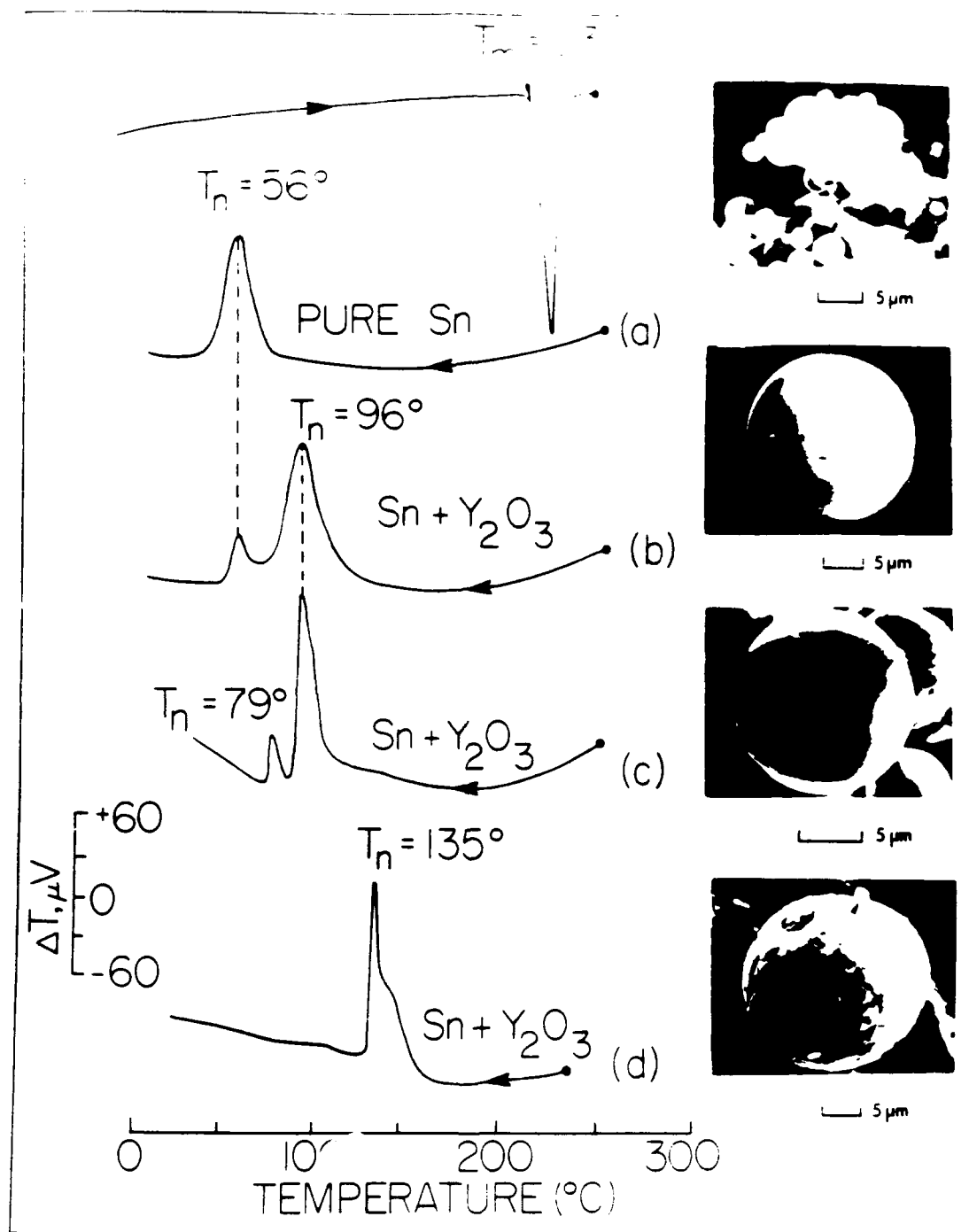


Figure 11

Nucleant site identification in pure Sn and Y_2O_3 particle dispersed Sn droplets.

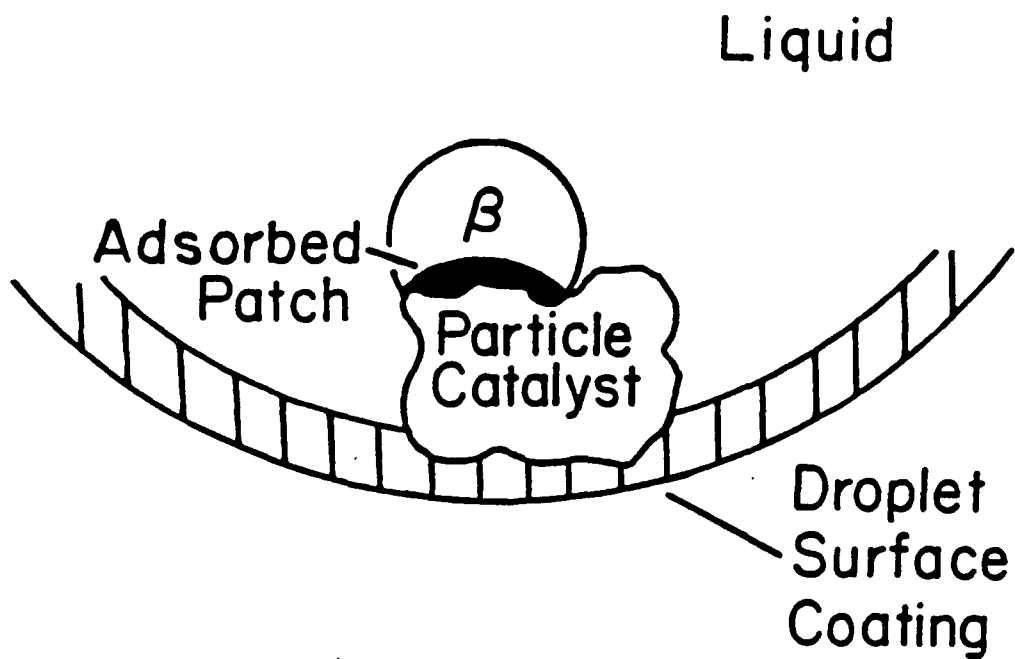


Figure 12

Schematic illustrating the nucleation catalysis model for inoculant particles that are stable in liquid Sn.

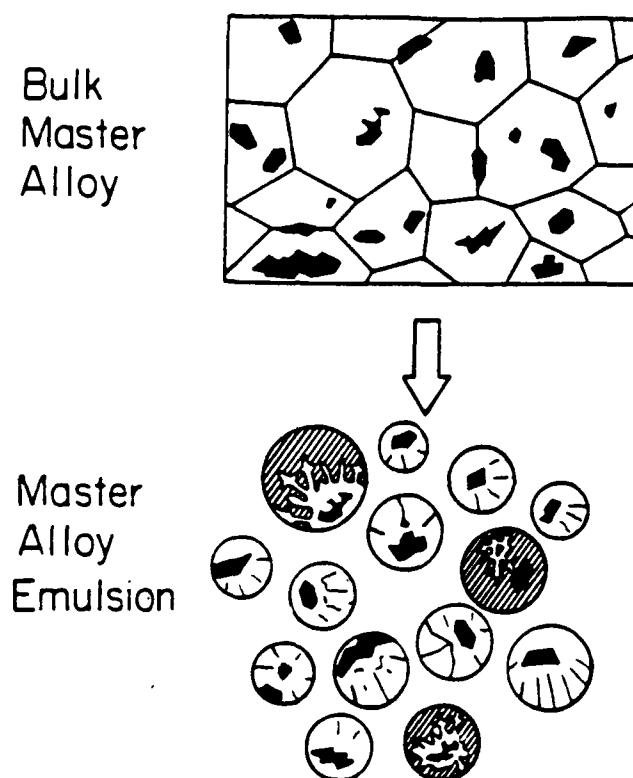


Figure 13

Schematic illustrating the production of Al master alloy droplet emulsions containing incorporated inoculant particles.

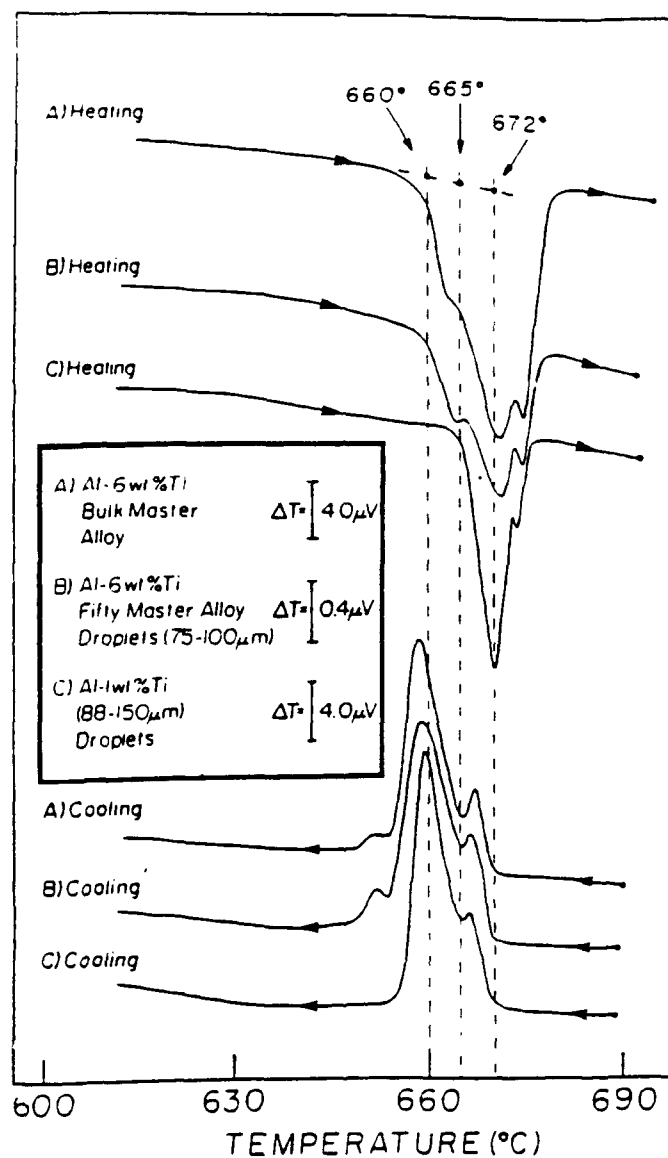


Figure 14

DTA thermograms depicting the melting and nucleation behavior of (A) a bulk commercial Al-6 wt.% Ti master alloy sample, (B) a droplet sample of the commercial Al-6 wt.% Ti master alloy and (C) high purity Al-1 wt.% Ti.

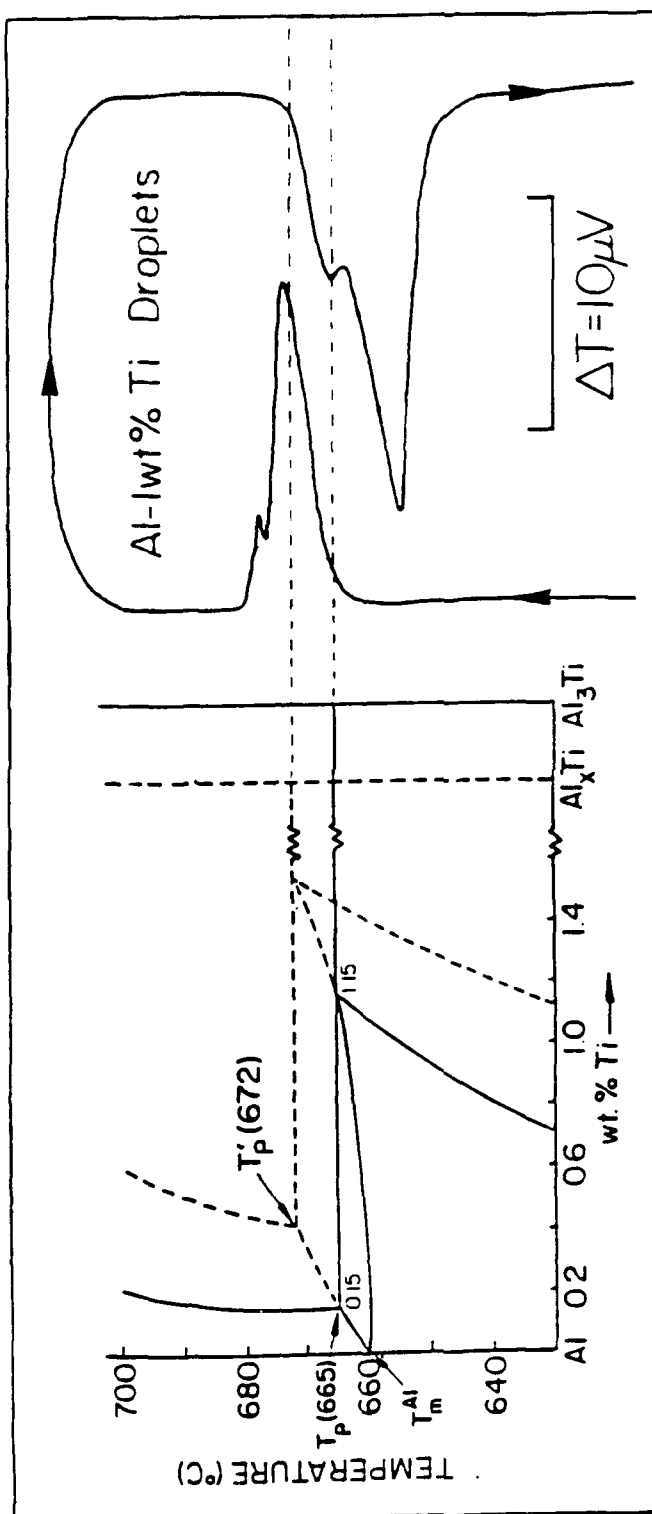


Figure 1.5

Schematic depicting the stable Al-Al₃Ti and metastable Al-Al_xTi phase diagrams and accompanying thermogram showing the melting and nucleation behavior of Al in high purity Al-1 wt.% Ti droplets.

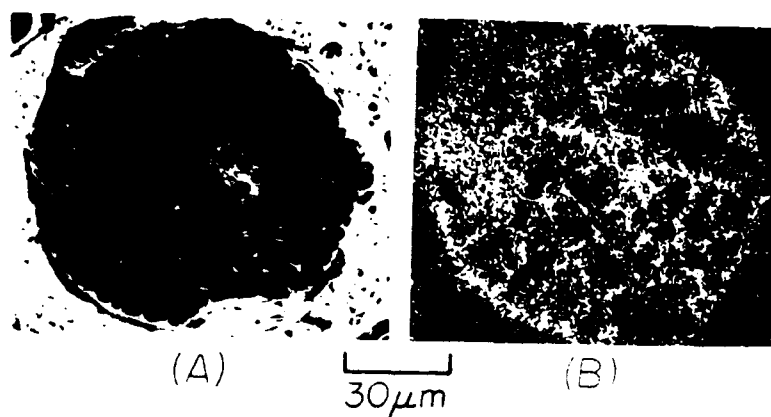


Figure 16

SEM photomicrograph (A) and corresponding X-ray map (B) of a master alloy droplet containing irregular faceted Si bearing inoculant particles that promoted Al nucleation prior to quenching from 671°C.

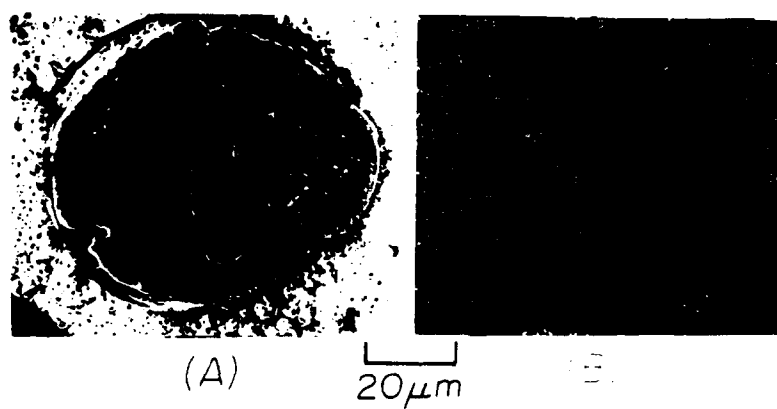


Figure 17

SEM photomicrograph (A) and corresponding X-ray map (B) of a master alloy droplet containing a blocky faceted Si free inoculant particle that has not promoted Al nucleation prior to quenching from 671°C.

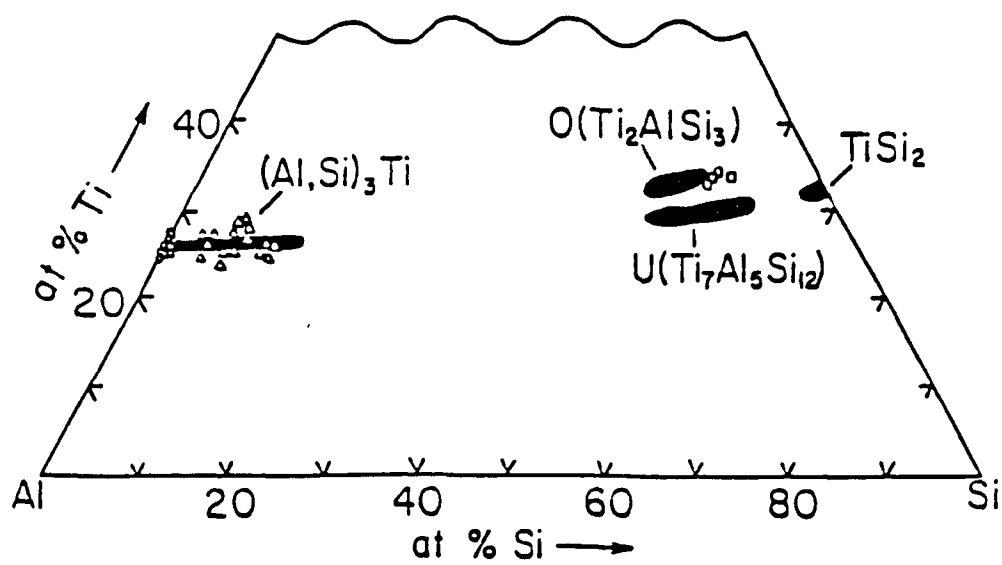


Figure 18

Enlarged view of the Al-Ti-Si phase diagram with superimposed EPMA compositional data from inoculant particles found in the master alloy droplets.

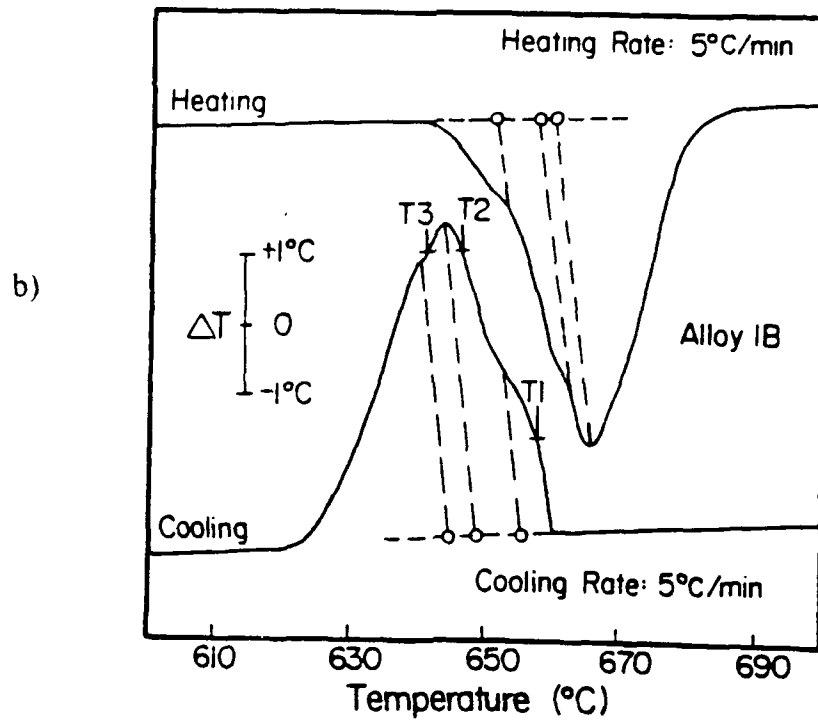
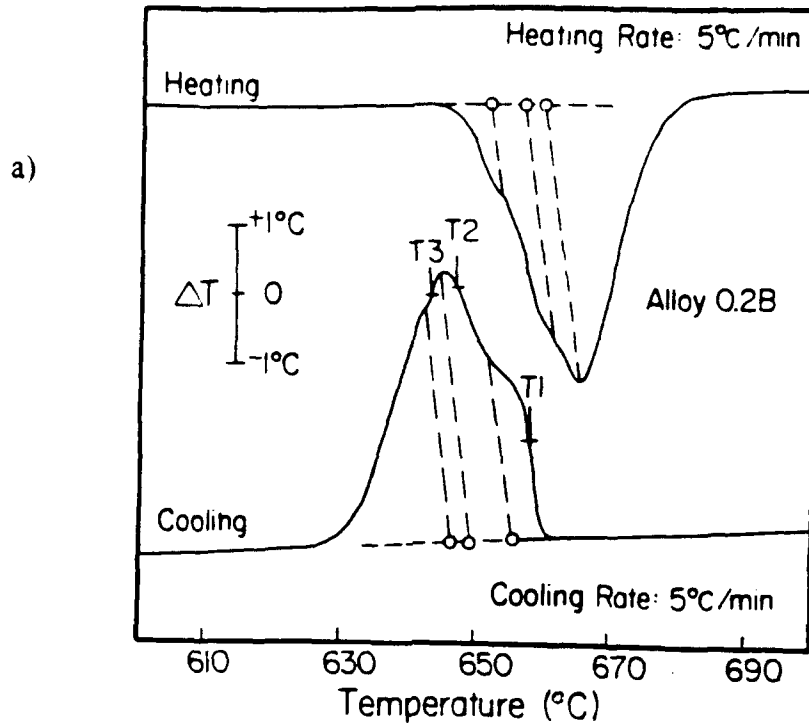


Figure 19

DTA thermograms obtained for Al-6wt.% Ti commercial alloys containing different amounts of Boron. The corresponding reaction temperatures are indicated as well as sets of quenching temperatures T1, T2, and T3: a) 0.2 %wt.B b) 1 %wt.B



Figure 20

Mixed backscattered and secondary electron image of Al-6 wt.% Ti-0.2 wt.% B alloy droplets quenched at T1 (Figure 19 b), revealing an active (A) and inactive (I) intermetallics. The sample was etched using 4% NaOH solution followed by 4% HF solution.



Figure 20

Mixed backscattered and secondary electron image of Al-6 wt.% Ti-0.2 wt.% B alloy droplets quenched at T1 (Figure 19 b), revealing an active (A) and inactive (I) intermetallics. The sample was etched using 4% NaOH solution followed by 4% HF solution.



Figure 21

Mixed backscattered and secondary electron image of Al-6 wt.% Ti-1 wt.% B alloy droplets quenched at T1 (Figure 19 b), revealing an active (A) and inactive (I) intermetallics. The sample was etched using 4% NaOH solution followed by 4% HF solution.

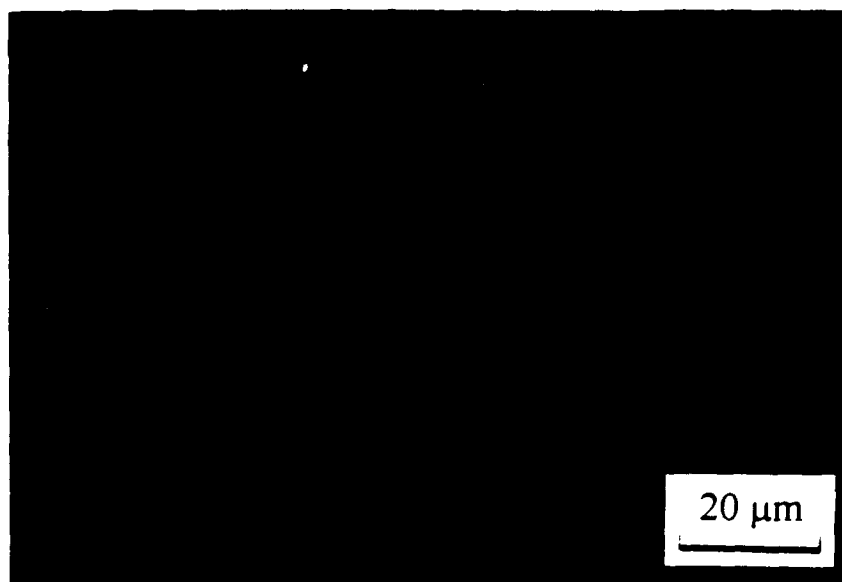


Figure 22

Mixed backscattered and secondary electron image photomicrograph of an unetched pure Al droplet containing a SiC particle emulsified at 800°C.

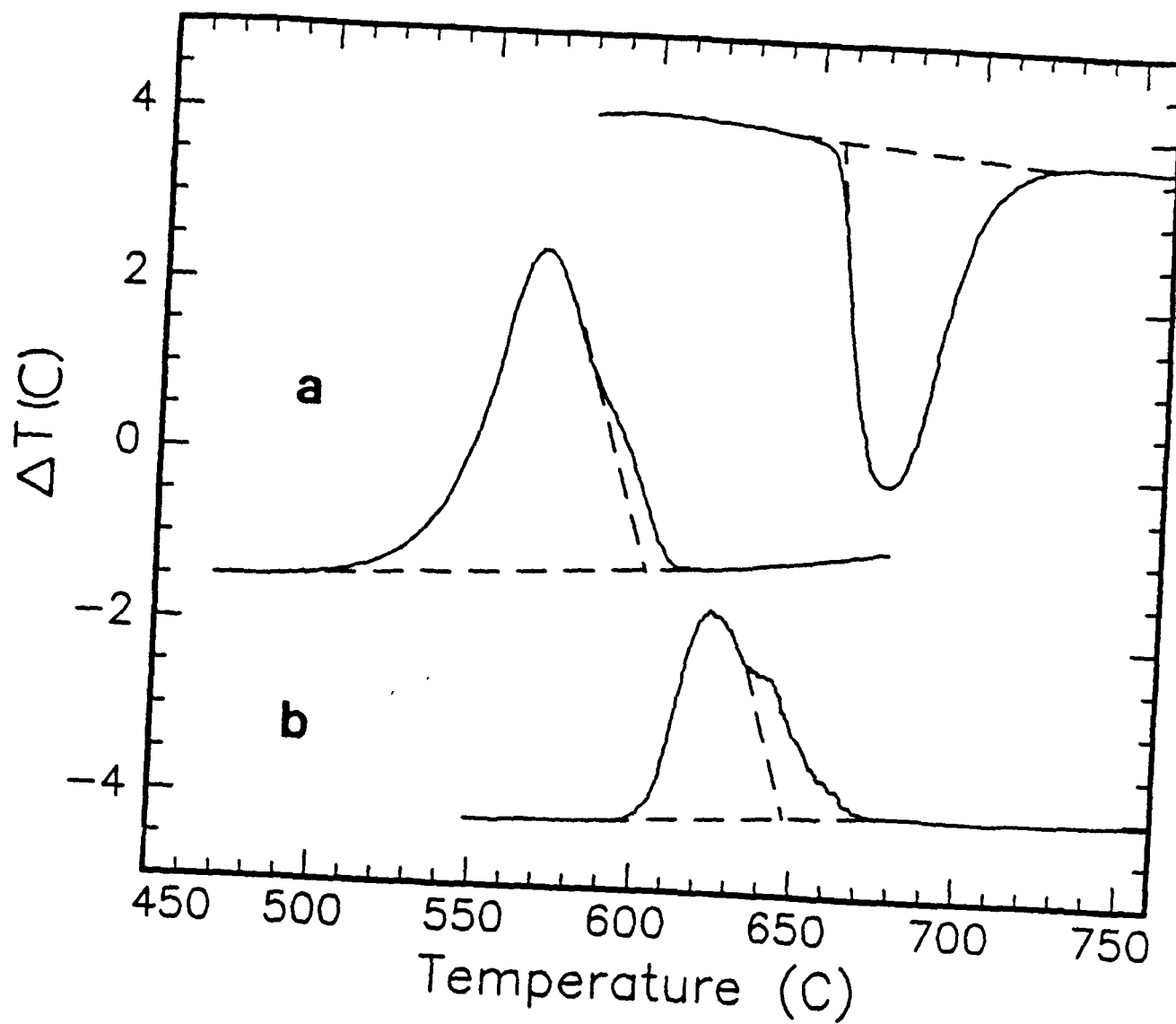


Figure 23

Differential Thermal Analysis traces generated by $\gamma\text{Al}_2\text{O}_3$ -Al composite droplet samples containing $1\text{ }\mu\text{m}$ $\gamma\text{Al}_2\text{O}_3$ particles at a heating rate of $5^\circ\text{C}/\text{min}$ and cooling rates of: a) $-30^\circ\text{C}/\text{min}$. b) $-3^\circ\text{C}/\text{min}$.

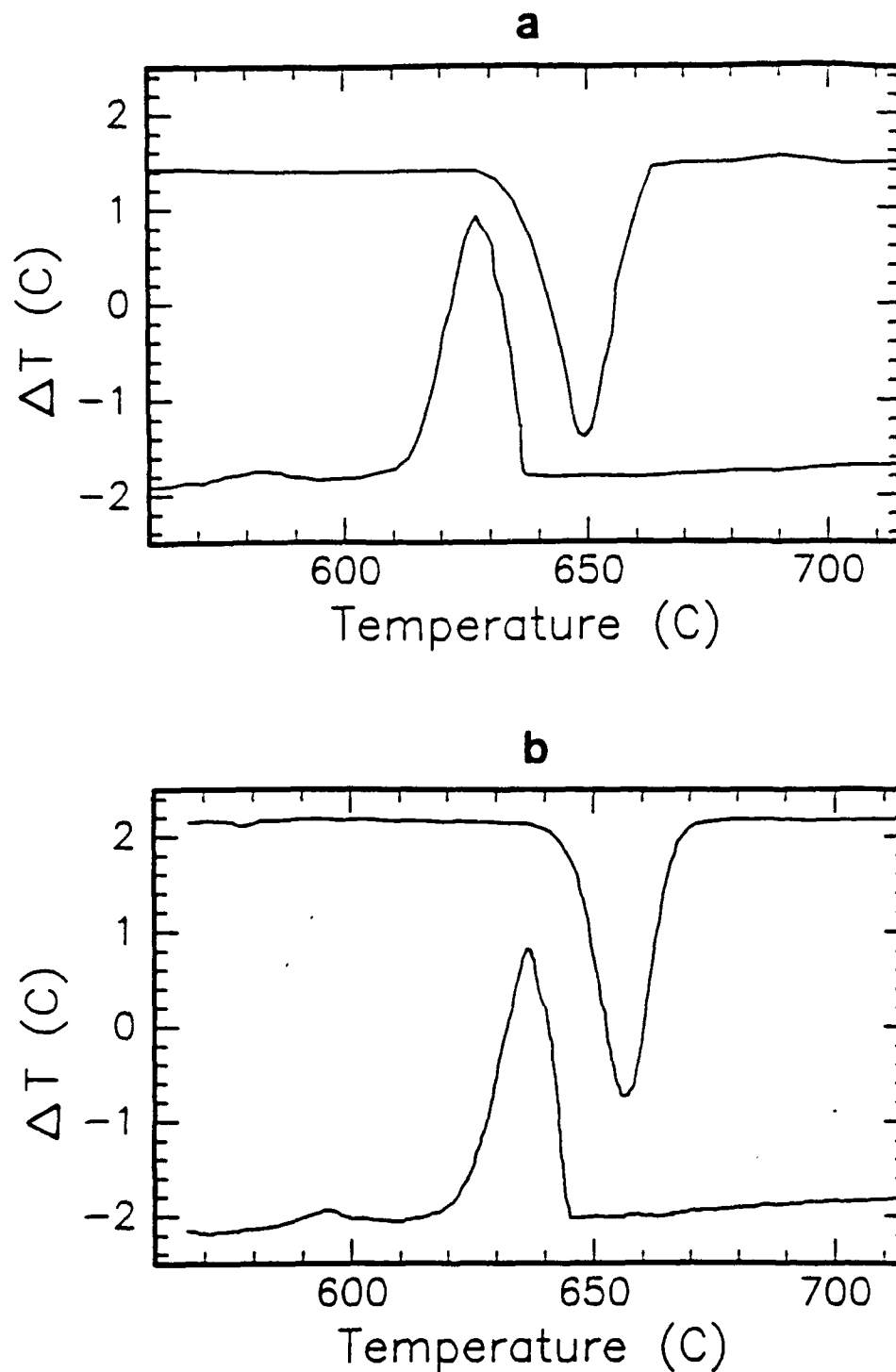


Figure 24

Differential Thermal Analysis traces generated by a SiC-Al composite droplet sample containing 10-40 μm SiC particles at heating and cooling rates of 5°C/min during: a) First cycle after emulsification. b) Second cycle after emulsification.

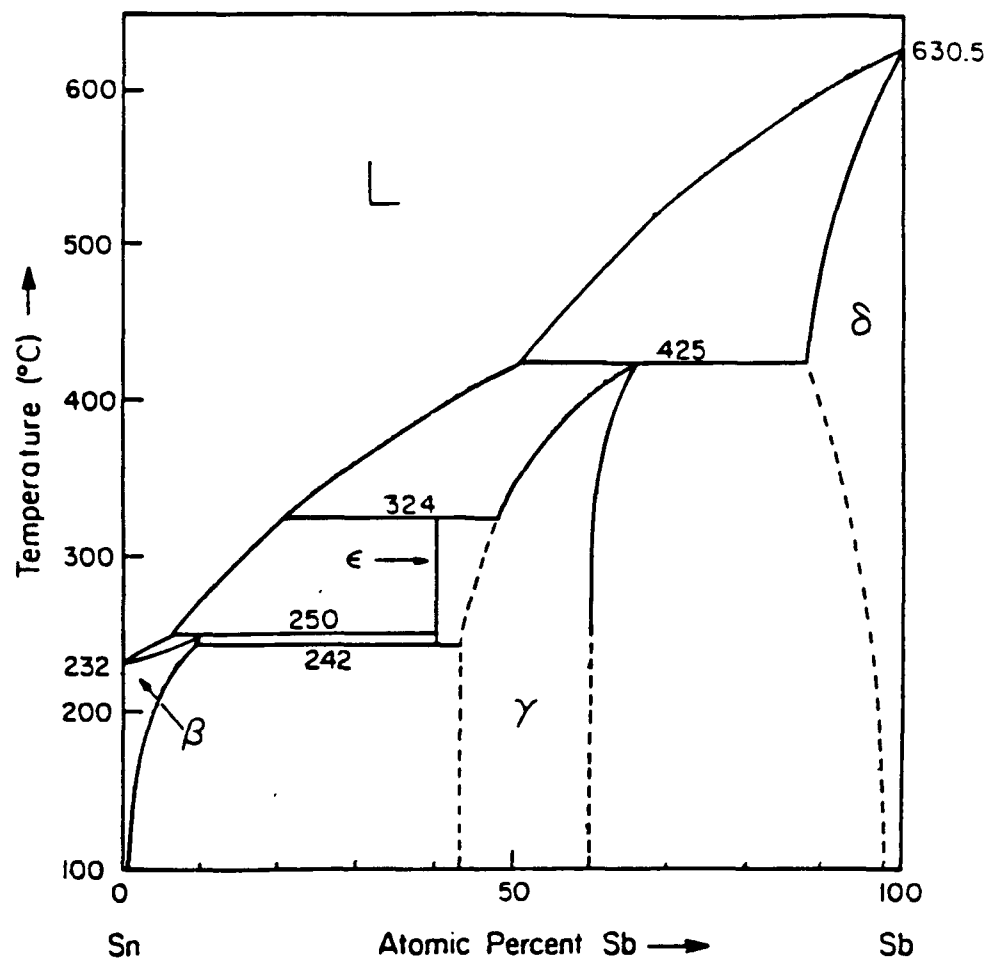


Figure 25

The Sn-Sb phase diagram of Predel and Schwermann. B. Predel and W. Schwermann, *J. Inst. Met.*, 99, 169 (1971).

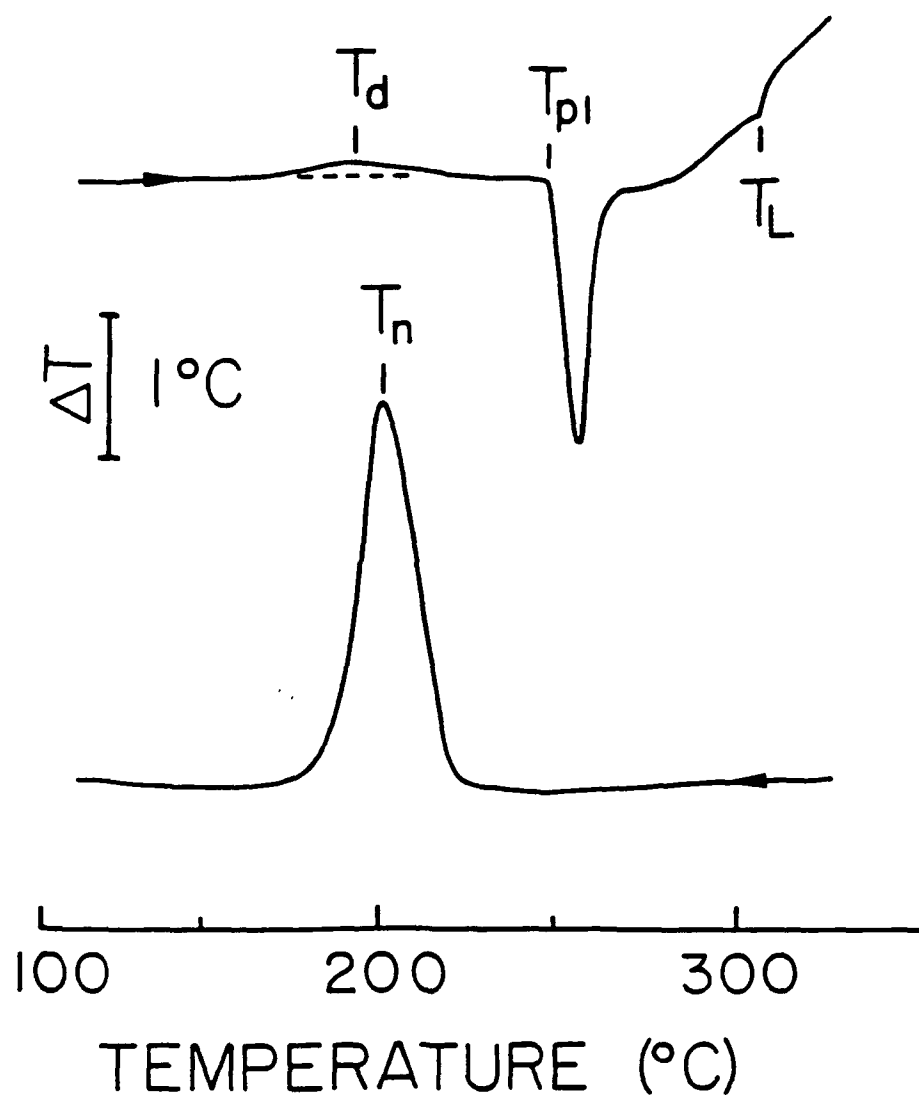


Figure 26

DTA thermogram of the emulsified Sn-16 wt.% Sb alloy. The sample was prepared under argon and treated with organometallic acids.

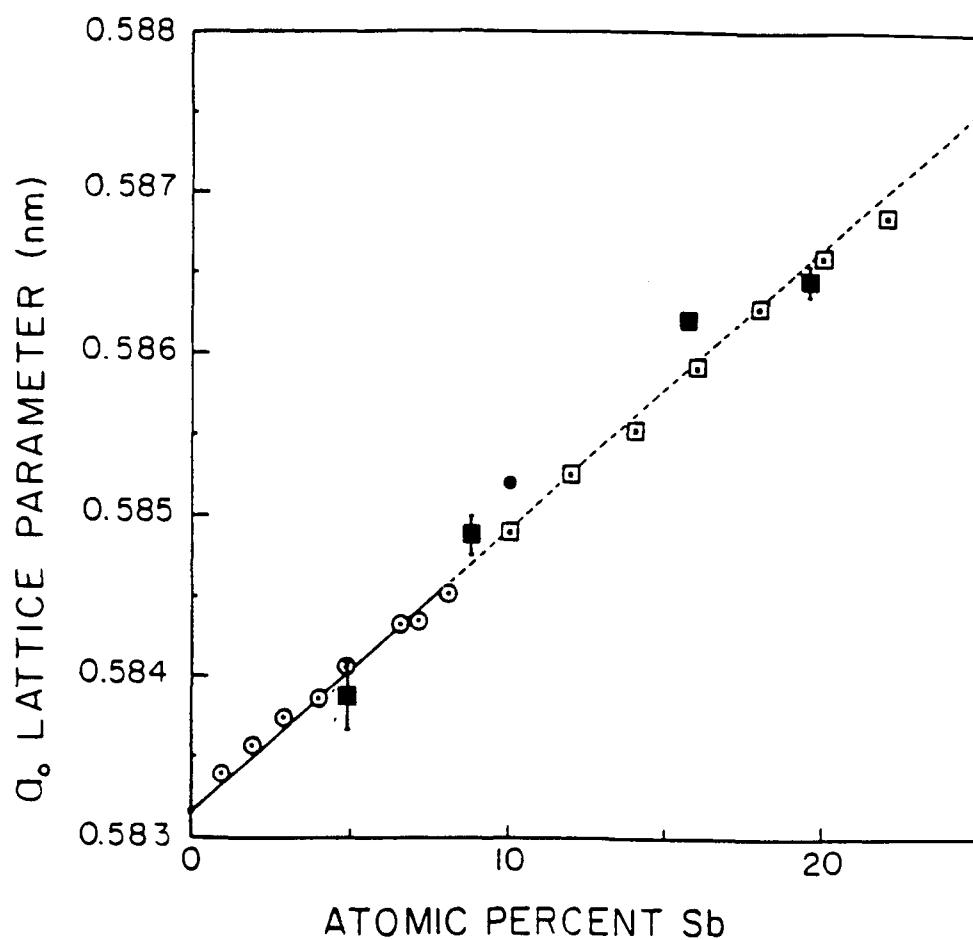


Figure 27

Compilation of measurements of the β lattice constant a_0 as a function of Sb content. Circles: Lee and Raynor (Ref: J. A. Lee and G. V. Raynor, *Proc. Phys. Soc.*, **B67**, 737 (1954); squares: Varich and Yakunin (Ref: N. I. Varich and A. A. Yakunin, *Izv. Akad. Nauk USSR. Met.*, **2**, 229 (1968); filled circle: Kaczorowski and Matyja (Ref: M. Kaczorowski and H. Matyja, *J. Mater. Sci.*, **14**, 2887 (1979); and filled square: present investigation.

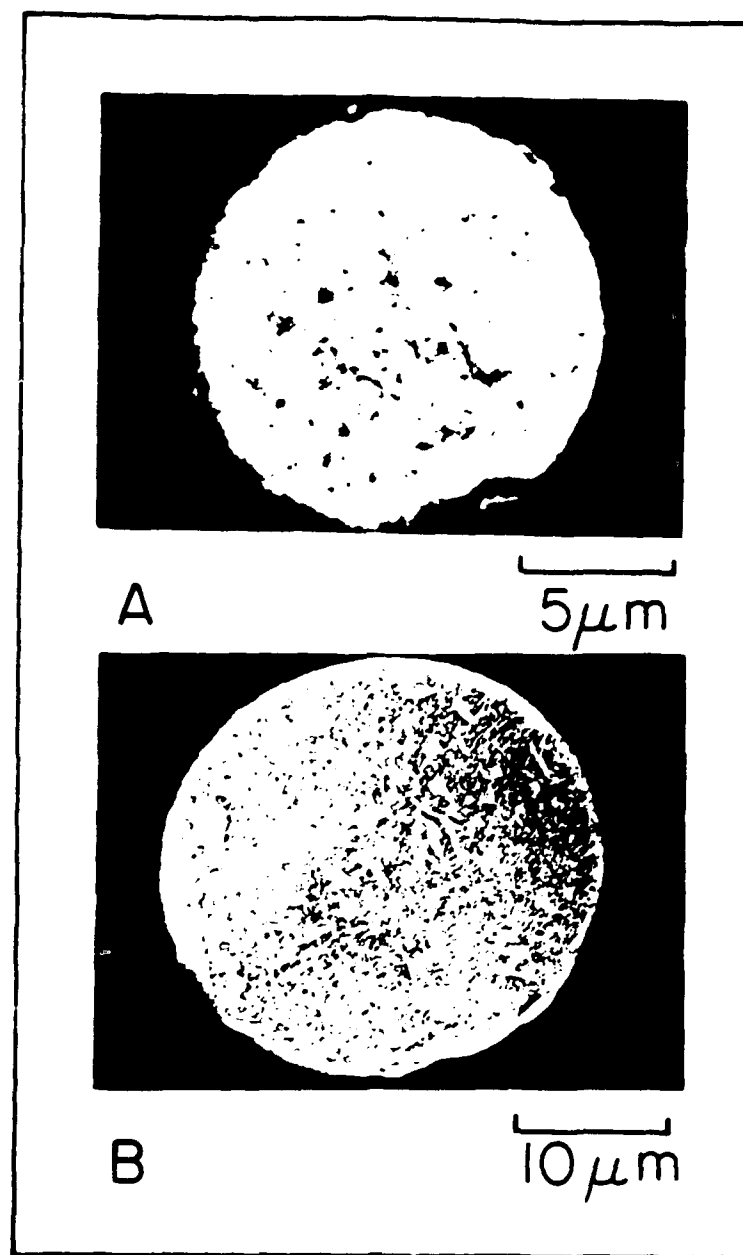


Figure 28

SEM micrographs of emulsified Sn-16 at.% Sb: argon cover with acid treatment. $\Delta T \cong 100^\circ\text{C}$. $T = 200^\circ\text{C s}^{-1}$. Micrograph A: as-solidified condition: powders consist of supersaturated β . Micrograph B: aged at room temperature: β contains a dispersion of SnSb precipitates.

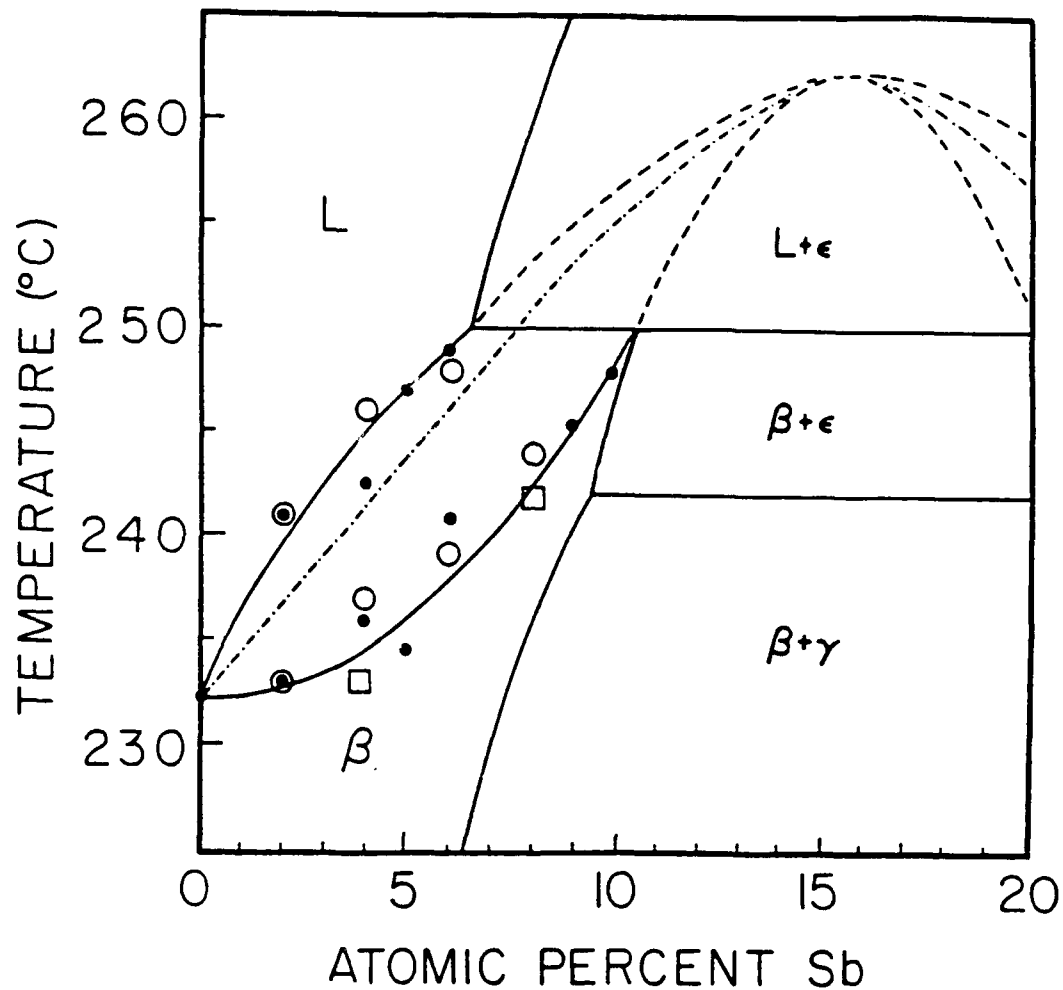


Figure 29

Tin-rich portion of the Sn-Sb phase diagram showing metastable extensions of the β liquidus and solidus as well as $T_0^{\beta+L}$ (dot-dashed line). A metastable melting point maximum is indicated in the vicinity of 15 at.% Sb. Open circles: Predel and Schwermann B. Predel and W. Schwermann, *J. Inst. Met.*, 99, 169 (1971); open squares: Iwasé *et al* (Ref: K. Iwasé, N. Aoki and A. Osawa, *Sci. Rep. Tôhoku Univ.*, 20, 353 (1931); and filled circles: present investigation.

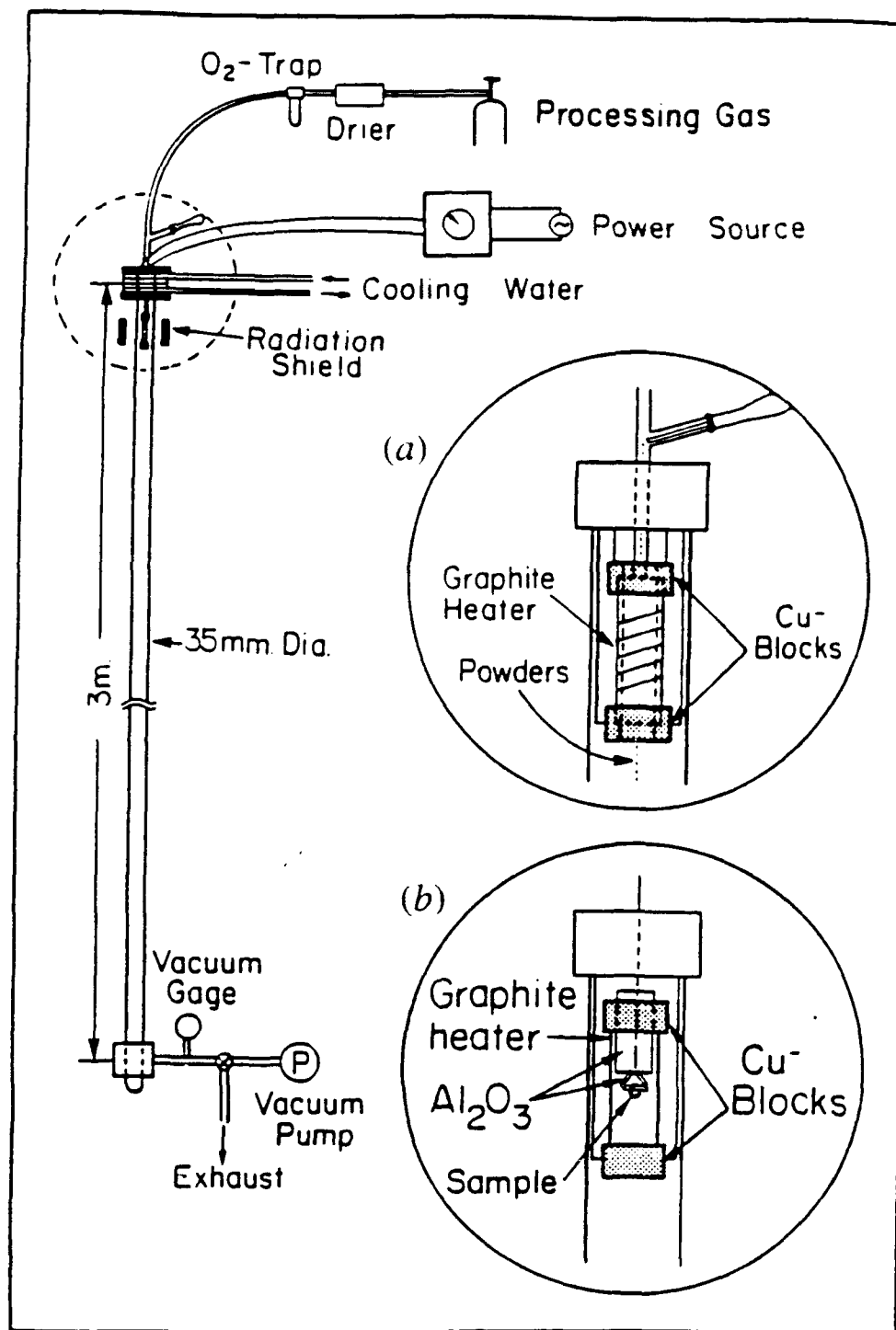


Figure 30

Schematic of the drop tube apparatus: (a) powder processing and (b) drop processing.

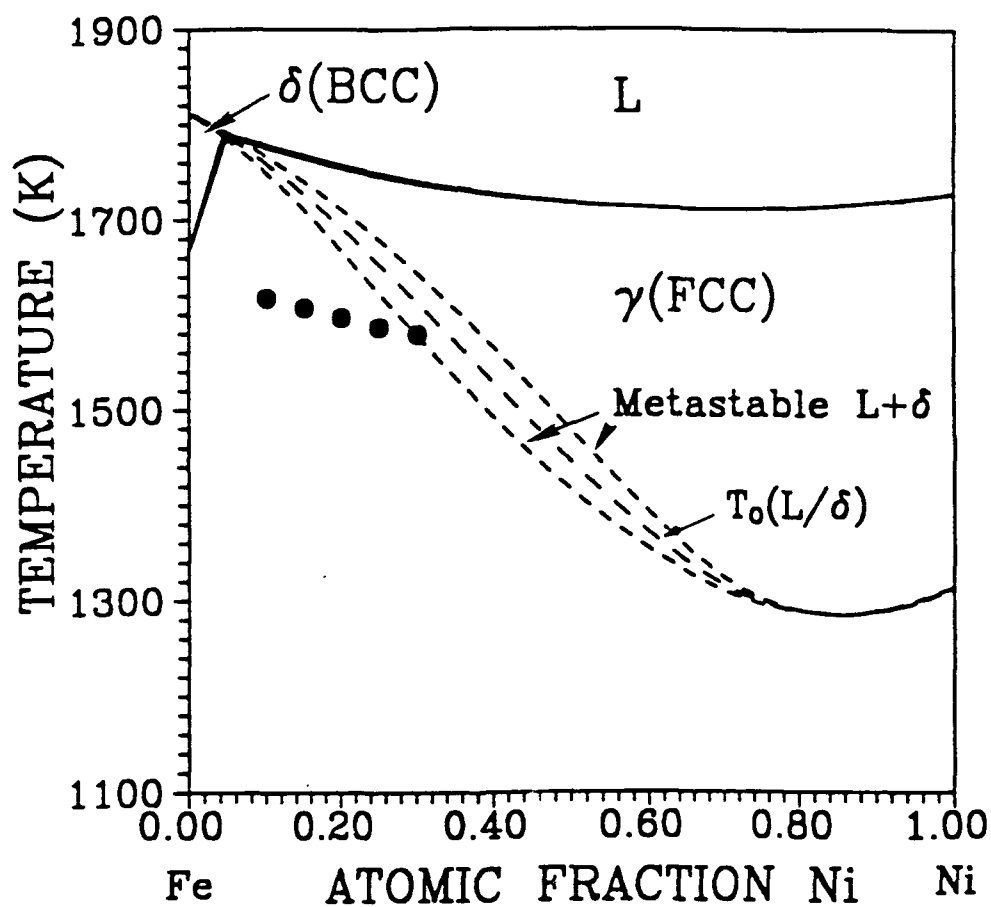


Figure 31

High-temperature Fe-Ni phase diagram with the undercooling levels of the large drops processed in He-2% H₂ labeled.

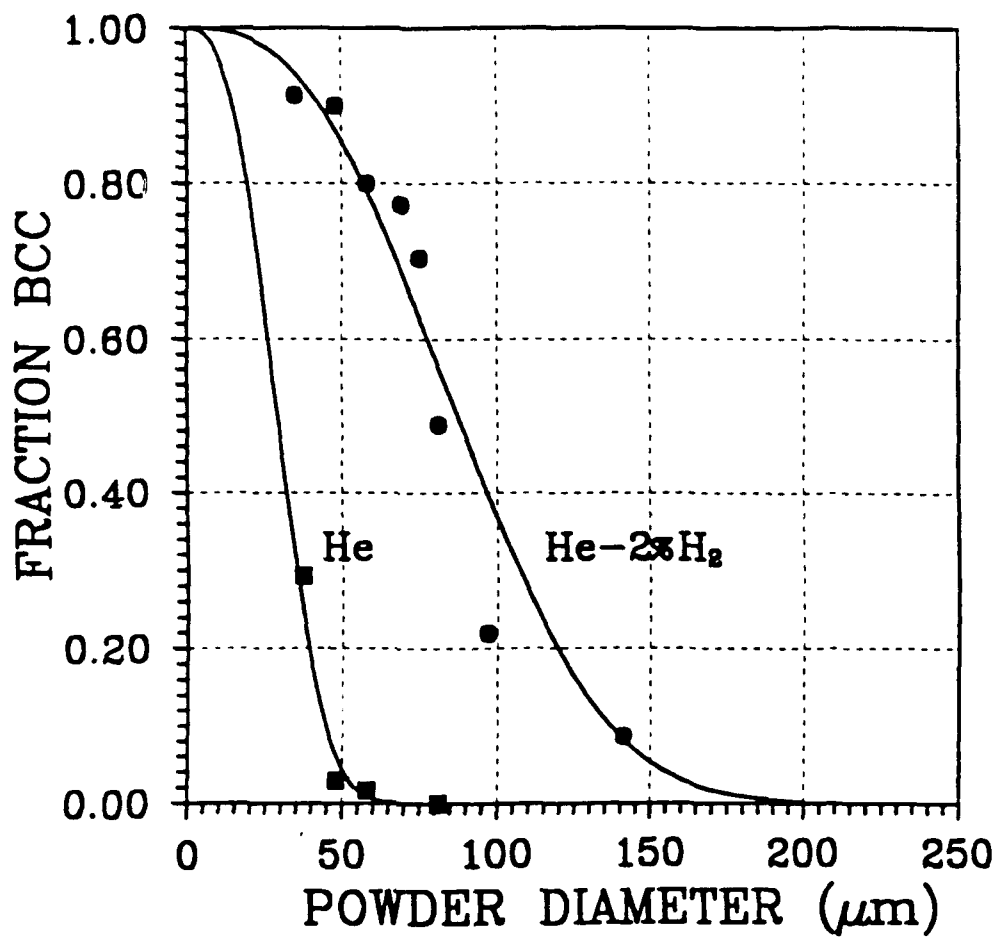


Figure 32

Comparative metastable bcc yields vs. average droplet diameter for Fe-15 wt.% Ni powder processed in He and He-2 % H₂ atmospheres.

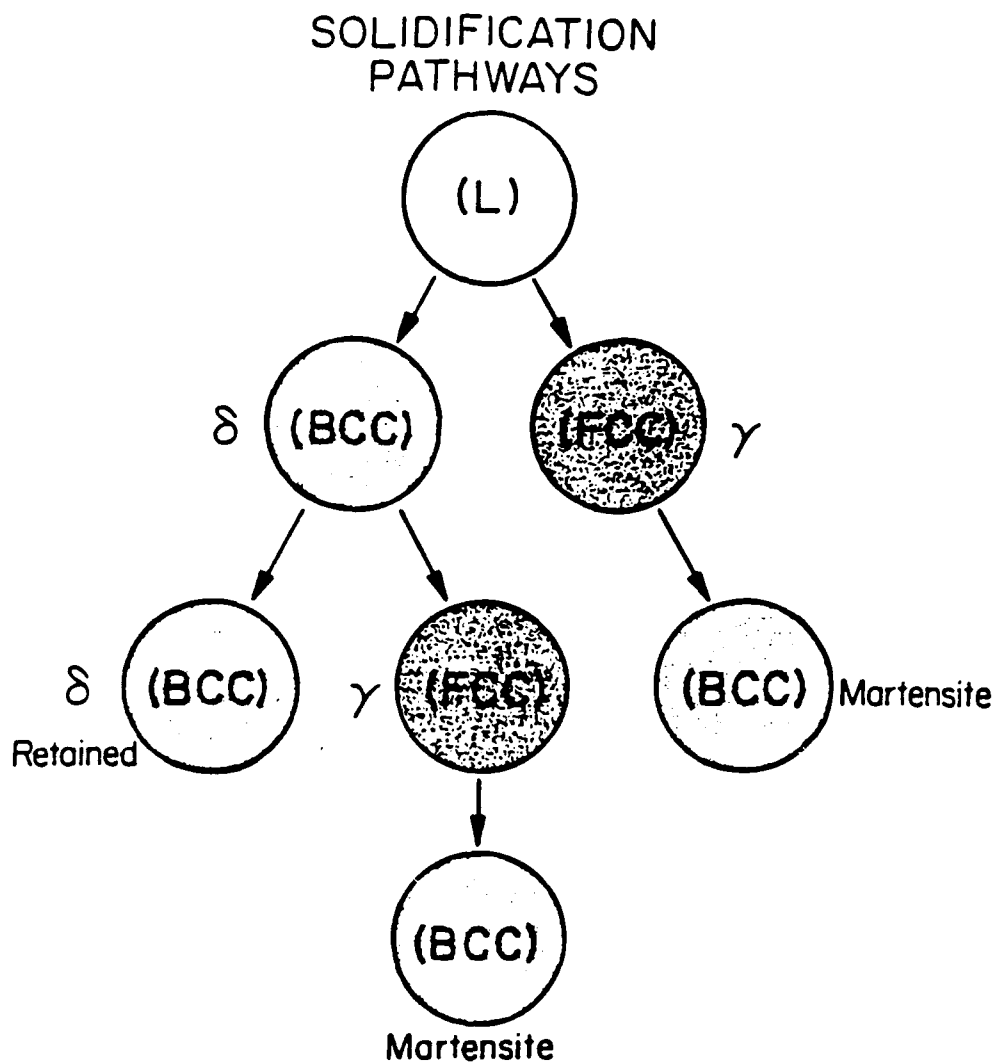


Figure 33

Schematic of two possible solidification pathways and different solid-state reactions for drop tube-processed samples.

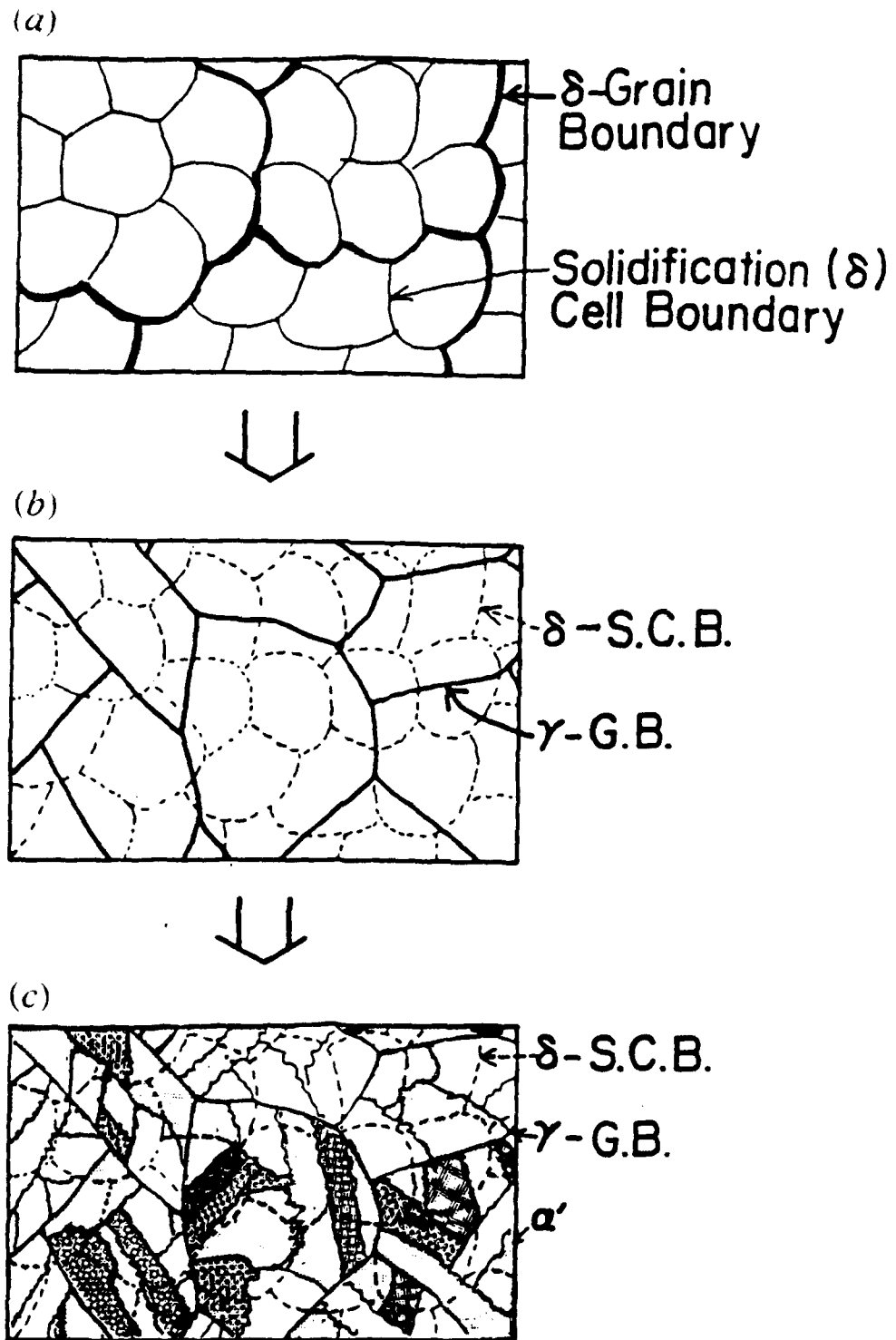


Figure 34

Schematic illustration of the microstructural evolution in large drops processed in the drop tube (S.C.B. = solidification cell boundary; G.B. = grain boundary; α' = martensite).

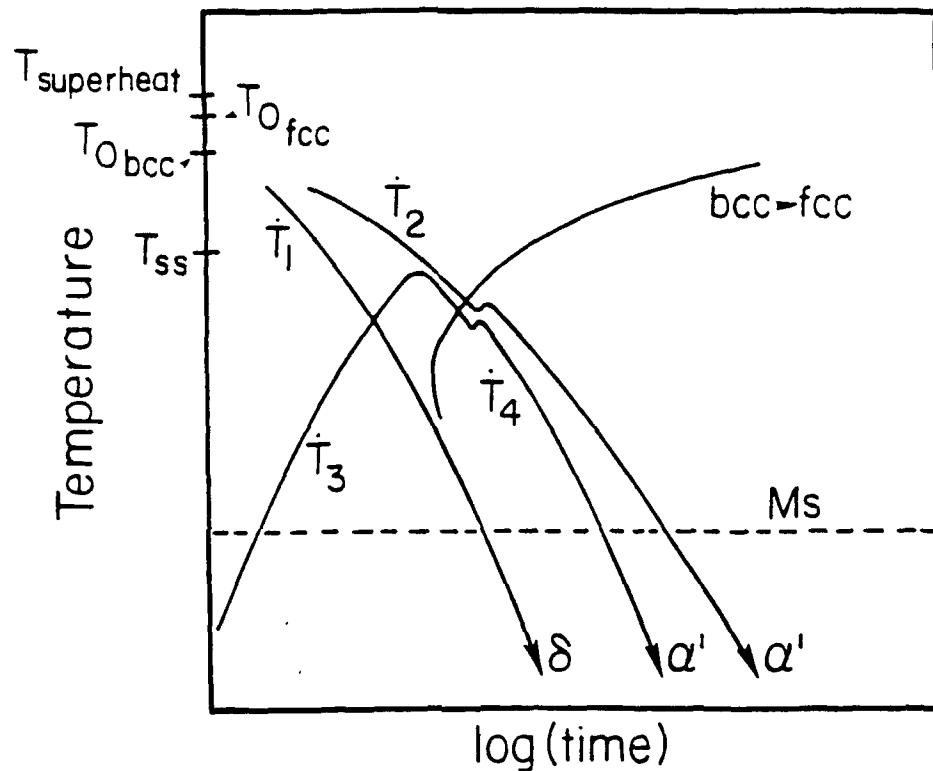


Figure 35

Schematic of solid-state powder processing pathways in Fe-15 wt.% Ni superimposed on a continuous cooling transition curve for bcc \rightarrow fcc: T_1 = cooling of solid powder ($d = 30$ to $44 \mu\text{m}$) processed from the melt; T_2 = cooling of solid powder ($d = 75$ to $100 \mu\text{m}$) processed from the melt; T_3 = heating of solid powder ($d = 30$ to $44 \mu\text{m}$) during reprocessing in the solid state; and T_4 = cooling of solid powder ($d = 30$ to $44 \mu\text{m}$) during reprocessing in the solid state.

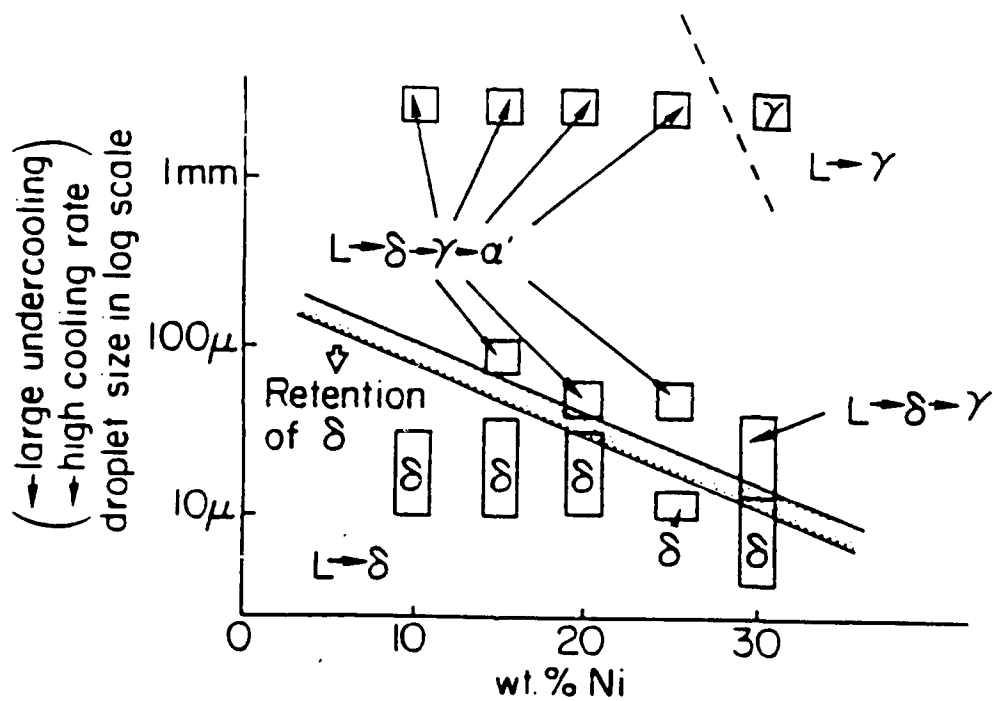


Figure 36

Summary of the structural evolution in the drop tube processing of Fe-Ni alloy processed in a He-2% H₂ environment.

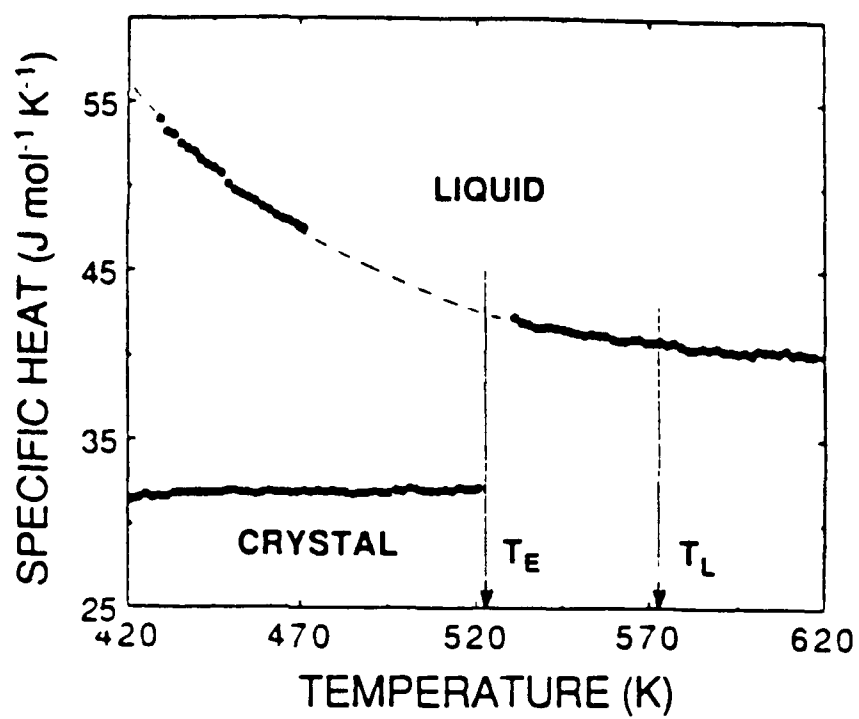


Figure 37

Heat capacity data measured for liquid and crystalline $\text{Au}_{53.2}\text{Pb}_{27.5}\text{Sb}_{19.3}$ alloys.

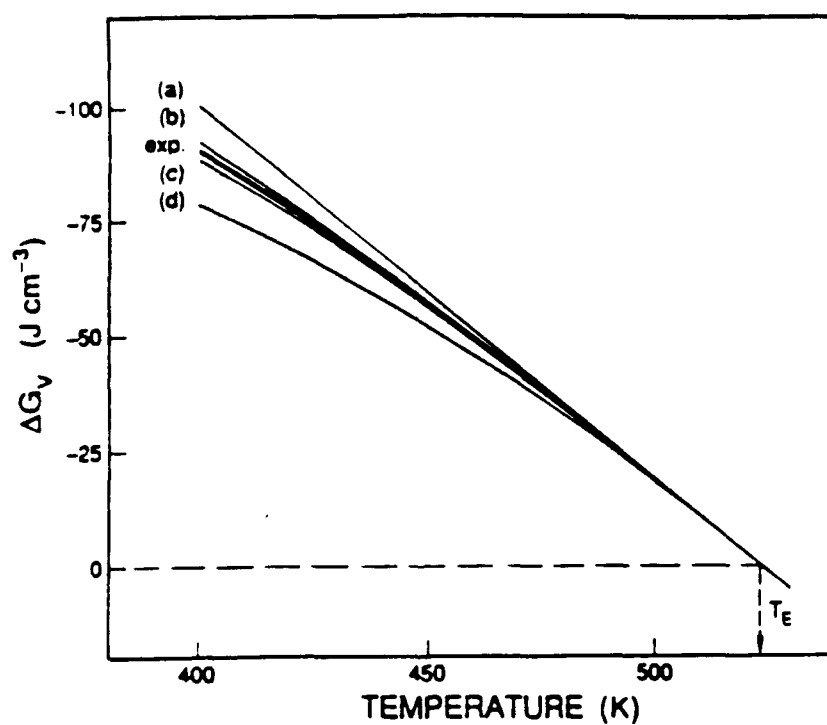


Figure 38

Free-energy difference between undercooled liquid and eutectic solid per unit volume based on different approximations including the experimental data.

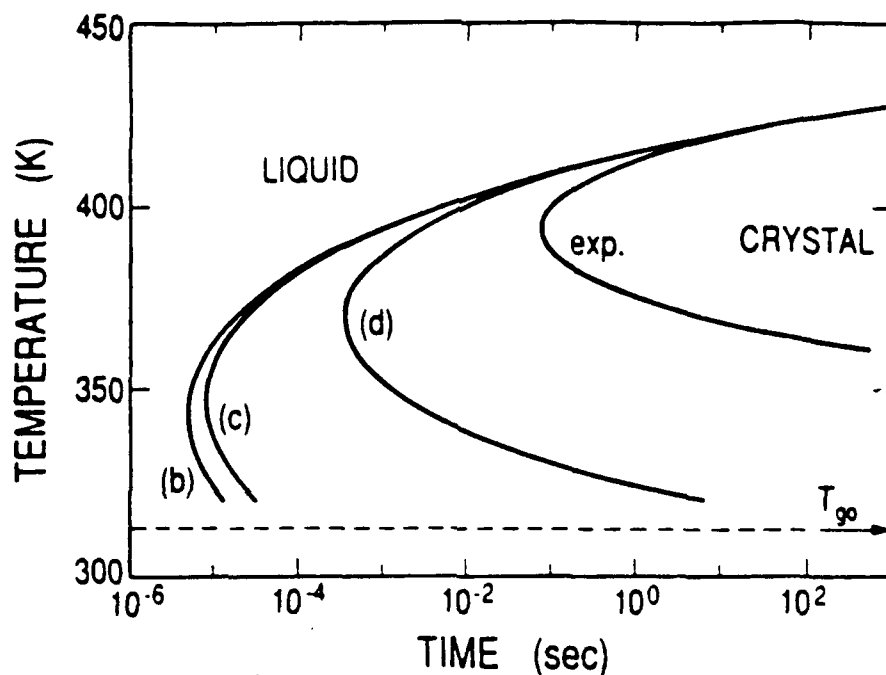


Figure 39

Calculated steady-state heterogeneous nucleation kinetics of glass-forming Au-Pb-Sb alloys including a correction for the temperature dependence of the viscosity of the prefactor terms for the different models for ΔG_V and the resulting ideal glass transition temperatures with the experimentally derived ideal glass transition temperature indicated as T_{g0} . The curves correspond to the extrapolation of experimental data (exp.), (b) to the approximation of ΔG_V and $T_{\Delta S=0}$ by Dubey and Ramachandrarao, *Acta Met.*, **32**, 91, (1984), (c) by Thompson and Spaepen, *Acta Met.*, **27**, 1855, (1979), and (d) by Hoffman, *J. Chem. Phys.*, **29**, 1192, (1958), respectively.

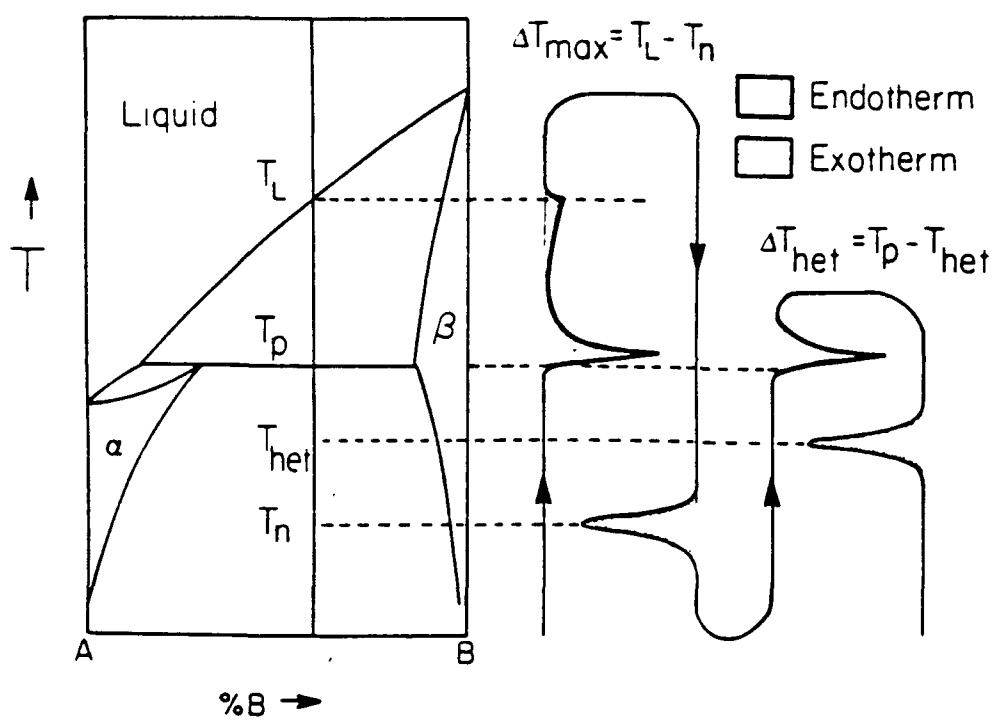


Figure 40

Illustration of the approach used to measure the catalytic potency of a primary substrate for nucleation of secondary phase.

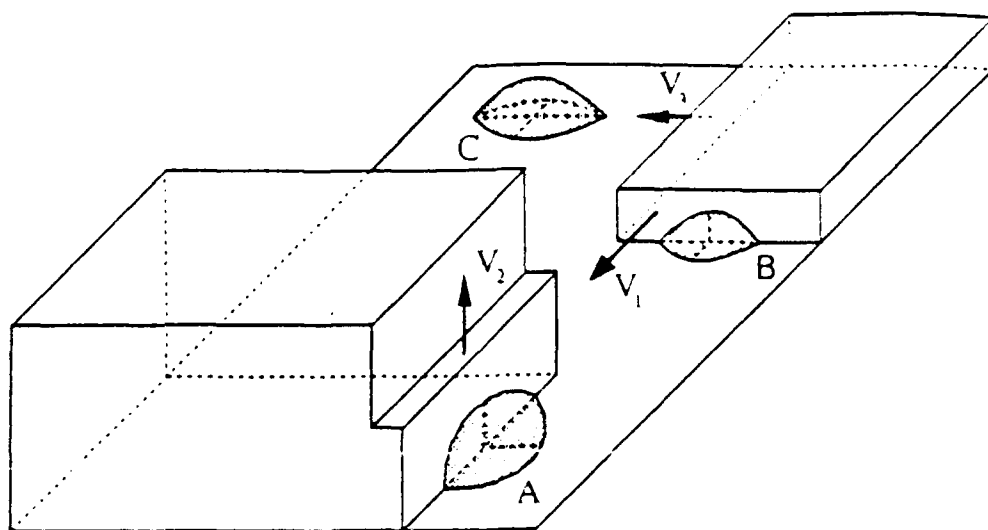


Figure 41

Geometry of heterogeneous nuclei with various substrate growth modes.

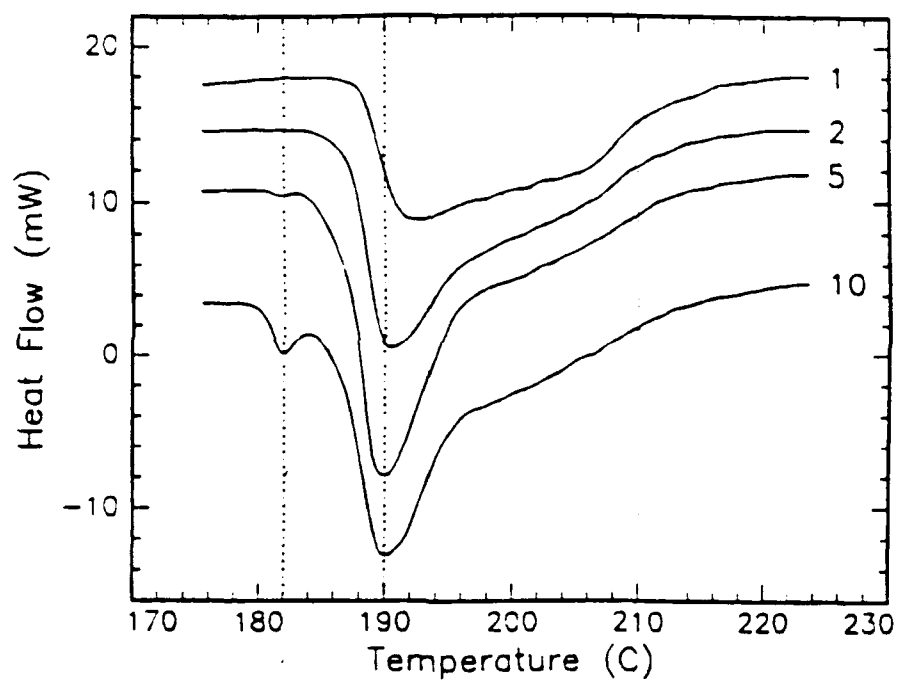


Figure 42

Exotherms observed during cooling phase of "het" cycles. The numbers along the right-hand side correspond to the cycle number. Note that the exotherm at 210°C disappears with increasing cycling, while the exotherm at 182°C increases.